Structural characterization of stressosome complexes by single-particle cryo-electron microscopy

Dissertation

zur Erlangung des Doktorgrades

der Naturwissenschaften

vorgelegt beim Fachbereich Biochemie, Chemie und Pharmazie

der Johann Wolfgang Goethe - Universität

in Frankfurt am Main

von

Susann Kaltwasser (geb. Münzner)

Frankfurt am Main 2015

Die Arbeit wurde in der Abteilung Strukturbiologie des Max-Planck-Institutes für Biophysik in Frankfurt am Main unter der Betreuung von Prof. Dr. Christine Ziegler durchgeführt und vom Fachbereich Biochemie, Chemie und Pharmazie der Johann Wolfgang Goethe-Universität als Dissertation angenommen.

Dekan: Prof. Dr. Michael Karas

1. Gutachter: Prof. Dr. Volker Dötsch

2. Gutachter: Prof. Dr. Christine Ziegler

Datum der Disputation:

CONTENTS

List of figures

List of tables

ABSTRACT

The stressosome is a Mega Dalton macromolecular complex involved in stress adaptation in bacteria. Stressosomes are considered as stress signaling hubs. They are able to perceive a variety of different stress stimuli and transduce them into one single cellular answer, which is the initialization of a transcriptional up-regulation of hundreds of different genes encoding for universal but also very specific stress response proteins.

The stressosome of *Bacillus subtilis* became a prime example for this intriguing stress-triggered transcriptional regulation when its architecture was determined by single-particle cryo-electron microscopy (cryo-EM) in 2008. In Gram-positive *Bacillus* species, the stressosome complex senses changes in salt concentration, ethanol content, blue-light, heat or acid stress contributing to the general stress response by activation of the alternative σ^B factor. σ^B is a transcriptional promoter that initiates the transcription of over 150 general stress genes, e.g. genes that encode osmolyte transporters to counteract osmotic and chill stress. The *B. subtilis* stressosome (stressosome_*Bc*) is composed of multiple copies of the three proteins: Rsb**R**, Rsb**S** and Rsb**T**. These three Rsb proteins (**R**egulator of **S**igma **B**) are found clustered in one operon forming the conserved **RST** module. RsbS and RsbR are scaffold proteins comprising a STAS domain, respectively. Because these domains are dominantly associated to **s**ulfate **t**ransporters and **a**nti-**s**igma antagonist they were named **STAS** domains, however, they were also identified in other sensor proteins. In the stressosome they form the internal ball-shaped core, while the N-terminal globin-fold sensor domain of RsbR, protruding to the outside, facilitates stress sensing. It is assumed that the stress signal is transduced to the stressosome core via the STAS domain resulting in conformational changes of the core. These changes affect the binding of the third protein, RsbT, a serin-threonine kinase. As a direct consequence of stress sensing the RsbT kinase is released from the complex to start an activation cascade involving the stepwise activation of RsbU, V, W, and X, which are all part of the same operon, and finally of σ^B. In *Bacillus* species, several RsbR orthologs were identified varying mainly in the sequence of the N-terminal

sensor domains. It is assumed that the stressosome_*Bc* assembles with a still unknown combination of RsbR orthologs allowing for the broad spectrum of stress stimuli that can be processed *in vivo*. The pathogenic bacteria *Listeria monocytogenes* is a close relative of *Bacillus*. Its potent stress response allows *Listeria* to survive the harsh environmental conditions during host infection and therefore the stress regulation machinery contributes heavily to the virulence of this pathogen. In *Listeria* the Rsb operon is conserved and highly homologous to the *Bacillus* one. In the frame of this thesis, the *in vitro* assembly of *Listeria innocua* stressosomes was shown for the first time by single-particle (SP) negative stain EM. Moreover, binding of *Listeria* RsbT to the assembled RsbR-RsbS complex was demonstrated biochemically.

Despite the conservation of the RST-module the entire Rsb operon is not conserved in the bacterial kingdom, suggesting that signal transduction and regulation of gene expression might occur by very different mechanisms in stressosomes of different species. We have focused here on a stressosome type from the Gram-negative pathogen *Vibrio vulnificus* that is quite distinct from the *Bacillus* ones with respect to (1) the missing conservation of the Rsb operon, (2) the role of RsbT, (3) the activation of a different transcriptional promoter, and (4) the absence of additional RsbR orthologs. Interestingly, there is only one RsbR protein encoded in the genome. This one contains a Haem-group in its N-terminal domain being oxygen sensitive. It is assumed that the *Vibrio* stressosome perceive only oxidative stress and that regulation occurs via a diguanylate cyclase with a GAF domain that synthesizes the second messenger c-di-GMP from GTP.

We have started a structure determination of the *Vibrio vulnificus* stressosome by SP cryo-EM to elucidate the differences in the molecular mechanism of stress sensing in divers stressosome types. A 3D map of the oxidized (activated) *Vibrio vulnificus* stressosome was determined to 7.6 Å resolution revealing an increased flexibility of both the core and the N-terminal sensor domains in comparison to the *Bacillus* stressosome suggesting that our structure has trapped for the first time an active state of a stressosome complex. A 3D map of the stressosome core to 7 Å resolution allowed fitting of a homology model of the *Vibrio* stressosome based on the *Bacillus*

stressosome as template. The conformational changes could be attributed to the entire core, which was confirmed by MD simulations.

ZUSAMMENFASSUNG

Mikroorganismen sind beständig sich ändernden Umweltbedingungen ausgesetzt. Daher müssen sie in der Lage sein auch sehr kurzfristig eine Stressantwort zu generieren. Anpassungsstrategien, um Änderungen wie beispielsweise des pH-Werts, der Temperatur, oder in der Nährstoffkonzentration entgegenzuwirken, finden unter anderen auf genregulierender Ebene statt. Hierbei werden zum einen generelle Stressproteine wie Chaperone zur Proteinstabilisierung oder Transporter zur Regulierung des osmotischen Haushalts und zum anderen Proteine, welche in Chemotaxis involviert sind, verstärkt exprimiert.

Adaptation an Kälte, UV Strahlung und osmotischen Stress wird in einigen Bakterien über das sogenannte Stressosom, einen zytoplasmatischen makromolekularen Komplex mittels eines eleganten Mechanismus reguliert. Trotz der enormen physiologischen Bedeutung von Stressosomen ist sehr wenig über deren Stress-Sensing Mechanismus bekannt.

Ausführliche zelluläre und strukturbiologische Daten existieren nur für das Stressosom von *Bacillus subtilis,* welches eine Aktivierung des Transkriptionsfaktors σ^B vermittelt. Basierend auf der in 2008 veröffentlichten Struktur des *Bacillus* Stressosoms setzt sich dieser Komplex aus drei verschieden Proteinen zusammen: RsbR (Rsb: **R**egulator von **S**ig**B**) und/oder dessen vier Paralogen, RsbS und RsbT, einer Serin- Threonin-Kinase. Alle drei kommen als Vielfachkopien im Komplex vor, wobei das Mengenverhältnis der Proteine bei 20 RsbR-Homodimeren zu 10 RsbS-Homodimeren und 20 RsbT Proteinen liegt.

Der Stressosomkern wird durch das Strukturprotein RsbS und das Sensorprotein RsbR gebildet. Beide Proteine besitzen eine C-terminale STAS (**S**ulfat **T**ransporter und **A**nti-**S**igma Faktor Antagonist) Domäne, welche in die Assemblierung des Komplexes involviert ist. STAS Domänen sind oft im Zusammenhang mit Sensordomänen zu finden, in bakteriellen Sensorproteinen ebenso wie in menschlichen Anionentransportern, und weisen eine konservierte Faltung bestehend aus vier α-Helices und vier β-Faltblatt Strukturen auf. Durch Konformationsänderungen oder veränderter Protein-Dynamik können durch

Sensordomänen empfangene Signale über die STAS Domänen weitervermittelt werden.

Die Globin-ähnlichen N-terminalen Domänen der RsbR Proteine ragen vom Kern nach außen und auf Grund ihrer exponierten Position wird davon ausgegangen, dass sie als Sensor diverse Umweltreize (Salze, Wärme, Ethanol, Licht) erfassen und an die C-terminale STAS Domäne weiterleiten. Mit Ausnahme vom RsbR-Paralog YtvA, ein Sensor für blaues Licht, sind keine Details über die Stress Stimuli bei *B. subtilis* bekannt. Im inaktiven Zustand inhibiert der Komplex die RsbT Kinase durch Bindung an RsbS. Unter Stress werden die STAS Domänen des Stressosoms an konservierten Aminosäureresten reversibel phosphoryliert, was zur Freigabe von RsbT führt. RsbT initiiert im Folgenden eine komplexe Signalkaskade, an deren Ende als Stressantwort die Aktivierung des σ^B Faktors steht, der wiederum die Expression von über 150 Stressgenen startet.

Die Gene der Stressosomkomponenten *rsbR*, *rsbS*, *rsbT* liegen als RST-Modul eines insgesamt acht Gene umspannenden Operons vor. Die konservierte Anordnung der Stressosomkomponenten als RST-Modul konnte auch in anderen bakteriellen Phyla (*Vibrio vulnificus*, *Listeria monocytogenes*, *Moorella thermoacetica* oder *Mycobacterium avium*) mittels Sequenzanalysen nachgewiesen werden.

In der vorliegenden Arbeit wurde der Stressosomkomplex aus *Listeria innocua* und *Vibrio vulnificus* untersucht. Da *Listeria monocytogenes* und sein nicht-pathogener naher Verwandter *Listeria innocua* beide ein RST-Modul im gleichen genetischen Kontext wie *B. subtilis* besitzen, wird angenommen, dass beide ein physiologisch relevantes Stressosom assemblieren können. Wie in *B. subtilis* liegen auch in *Listeria* vier Paraloge von RsbR vor, deren funktionelle Rolle im Stress-Sensing, bspw. unterschiedliche Stimuli zu detektieren, unbekannt ist. Es ist ebenfalls unbekannt in welcher Stöchiometrie die unterschiedlichen RsbR Homologe sich unter verschiedenen Stressbedingungen assemblieren. Dies ist problematisch, wenn es, wie in der vorliegenden Arbeit angestrebt, darum geht einen molekularen Regulationsmechanismus in Abhängigkeit des Stress-Typs aufzuklären. Interessanterweise existieren in *V. vulnificus* keine Orthologe von RsbR, d.h. Stress-Sensing wird ausschließlich über ein RsbR (*Vv*R) durchgeführt, welches unterschiedlich zu den *Bacillus*-Homologen eine zusätzliche Sensorglobindomäne

besitzt. Sensorglobine binden als Cofaktor Häm. Die reversible Oxidation von Fe-O_2 bewirkt eine Konformationsänderung, welche dann das Stressosom aktiviert. Auf Grund dieser oxidativen Aktivierung ist auch die Rolle des *Vibrio* RsbT Homologs, *Vv*T, nicht verstanden. Beispielsweise ist bis heute nicht geklärt, ob es überhaupt zu einer regulativen Bindung zwischen *Vv*S (*Vibrio* RsbS Homolog) und *Vv*T kommt. Die vom Stressosom aktivierten regulatorischen Proteine stehen, im Gegensatz zu *B. subtilis*, bei dem Humanpathogen *V. vulnificus* nicht im Zusammenhang mit der Aktivierung des generellen Stressfaktors σ^B, sondern sind u.a. für die Hochregulierung von GMP bindenden Proteinen verantwortlich. Diese synthetisieren cyclisches di-GMP aus GMP, einen sekundären Botenstoff in Bakterien der bei *Vibrio*, *Salmonella* und *Caulobacter* an der Modulation von Anpassungsreaktionen auf Umweltreize beteiligt ist. Zu den c-di-GMP regulierten Stressantworten gehören chemotaktische Bewegung, Biofilmbildung und Virulenz.

Es konnte im Rahmen dieser Arbeit gezeigt werden, dass sich die *Listeria innocua* Stressosomkomponenten, welche im RST Modul codiert sind, in *Escherichia coli* exprimieren lassen. Die heterolog synthetisierten und aufgereinigten RsbR, RsbS und RsbT (hier *Li*R, *Li*S und *Li*T) Proteine lagern sich *in vitro* zu einem Komplex zusammen, was mittels Größen-Ausschluss-Chromatographie und Elektronenmikroskopie gezeigt werden konnte. Erste elektronenmikroskopische Einzelpartikelanalysen mittels Negativkontrastierung zeigen zweifach und fünffach Symmetrien des Komplexes.

Im Hauptteil der Arbeit wurde die Struktur des durch Oxidation aktivierten Stressosomes von *V. vulnificus* mittels Einzelpartikelanalyse unter Kryo-Bedingungen untersucht. Die 3D Struktur wurde bis zu 7.6 Å gelöst, wobei die N-terminalen Domänen von *Vv*R eine niedrigere Auflösung (8-10 Å) als der Kern (um 6 Å) aufweisen. Im Kern sind Sekundärstrukturen wie α-Helix und β-Faltblatt erkennbar. Der Kern setzt sich aus 20 Dreieckflächen und 12 Fünfeckflächen zusammen. Diese Anordnung führt zu einer D2 Symmetrie des Komplexes. Die 40 N-terminalen *Vv*R Domänen treten als Dimere an 20 von insgesamt 30 Kanten auf.

Das *Vv*RS Stressosom zeigt den gleichen Grundaufbau wie das Stressosom von *B. subtilis*. Die N-terminalen Domänen des Sensorproteins *Vv*R sind im aktivierten

Zustand flexibler als die des *Bacillus* Stressosoms. Die erhöhte Flexibilität ist höchstwahrscheinlich dem aktivierten Zustand des Stressosomes geschuldet.

Zudem konnte im Rahmen der Arbeit erstmals gezeigt werden, dass der STAS-Domänenkern nicht wie zuvor beschrieben als starres Gerüst auftritt. Der Kern wurde mit einer Auflösung von 7 Å ermittelt. Weiterführende Untersuchungen wie 2D und 3D Klassifizierungen des Datensatzes zeigten verschiedene Zustände des Kerns, deren Konformationsänderungen am besten durch eine Dehn- und Kompressionsbewegung beschrieben werden können. Diese Flexibilität des STAS-Domänenkerns steht im Einklang mit Molekulardynamik-Simulationen.

Ein Homologiemodell des *Vv*RS Stressosoms basierend auf der Struktur von *B. subtilis* konnte in das 3D Volumen eingepasst werden. Innerhalb des STAS Domänenkerns lassen sich Kontaktflächen für Homodimere von *Vv*R und *Vv*S sowie für benachbarte Monomere beobachten. Die β-Faltblattstrukturen der STAS Domänen zweier Monomere bilden in den Homodimeren eine hydrophobe Kontaktfläche. Eingegrenzt sind die β-Faltblattstrukturen jeweils von einem α-helikalen Bündel. Stets sind zwei Helices (α1, α2) einer STAS Domäne in Kontakt mit einer Helix (α3) des benachbarten STAS Proteins. Interessanterweise zeigten Untersuchungen an Ionentransportern mit STAS Domänen für diese beiden Helices (α1, α2) Konformationsänderungen bei Stimulation. Durch diesen Kontakt könnte auch die Signalweiterleitung innerhalb des Stressosomenkerns erfolgen. Da STAS Domänen in die Signalübertragung in diversen Sensormodulen involviert sind, ist anzunehmen, dass sie im Stressosom während der Signalweitergabe Konformationsänderungen durchführen, welche die beobachteten Deformationen des Kerns bewirken könnte. Inwieweit die Flexibilität der N-terminalen Domänen und die des Kerns im Zusammenging mit der Bindung des Cofaktors Häm oder der fehlenden dritten Stressosomkomponente RsbT stehen, ist unklar. Zukünftig kann ein Vergleich mit dem reduzierten inaktiven Zustand des *V. vulnificus* Stressosoms mittels Kryo-EM entsprechende Ergebnisse liefern.

1. INTRODUCTION

1.1 Single-particle analysis a method for structure determination

The topic of this thesis is the molecular understanding of the activation mechanisms of the stressosome complex. As main method, cryo-EM single-particle (SP) analysis was chosen for several reasons, which will be summarized shortly in the next section before introducing the stressosome itself.

Structure-Function studies are absolutely necessary for the understanding of biologically relevant mechanisms on a molecular level. However, determination of an atomic structure is still challenging when it comes to macromolecular complexes and membrane proteins, which both represent intrinsically heterogeneous mixtures; in macromolecular complexes due to the assembly of several subunits, in membrane proteins due to their association with lipids and detergents. Crystallography was for a long time the only possibility to achieve atomic resolution requiring high amounts of stable protein. 3D crystals, however, represent a highly artificial non-physiological environment caused by the high concentrations, the de-hydrated conditions and crystal contacts. There is a high risk that conformational flexibility, which is often a characteristic of subunit assemblies in macromolecular complexes, is limited. Therefore, from the beginning, 3D crystallization was not considered an option for the stressosome complex.

On the other hand, single-particle cryo-electron microscopy became a powerful tool to investigate three-dimensional structures of high molecular weight complexes (Gabashvili et al., 2000; Ludtke et al., 2001; Ludtke et al. 2008; Zhang, et al. 2010; Mills et al., 2013) allowing the observation of proteins in their native states. What started as "Blobology" in the 1980s with e.g. structures of ribosomes (Rademacher et al., 1987; Wagenknecht et al. 1989, Frank et al. 1991) has developed to one of the most powerful techniques in structural biology over the last 30 years (Figure 1). Since Dubochet et al. reported in 1982 about the huge advantage of proteins embedded in vitreous ice to obtain higher resolution, especially complexes with high symmetry, large molecular mass and rigidity like viruses (Cheng et al., 2009; Wolf et al. 2010; Grigorieff and Harrison, 2011) and even a single ribosome

(Armache et al, 2010) could be solved, although not to atomic resolution. The breakthrough was achieved for the SP method when Zhang et al. determined the structure of the primed, infectious subvirion particle of aquareovirus at 3.3 Å in 2010. They presented the 3D map. But for smaller and non-symmetric molecules structure determination with single-particle analysis was still a challenging method that leads to low resolution maps around 10 Å at the best.

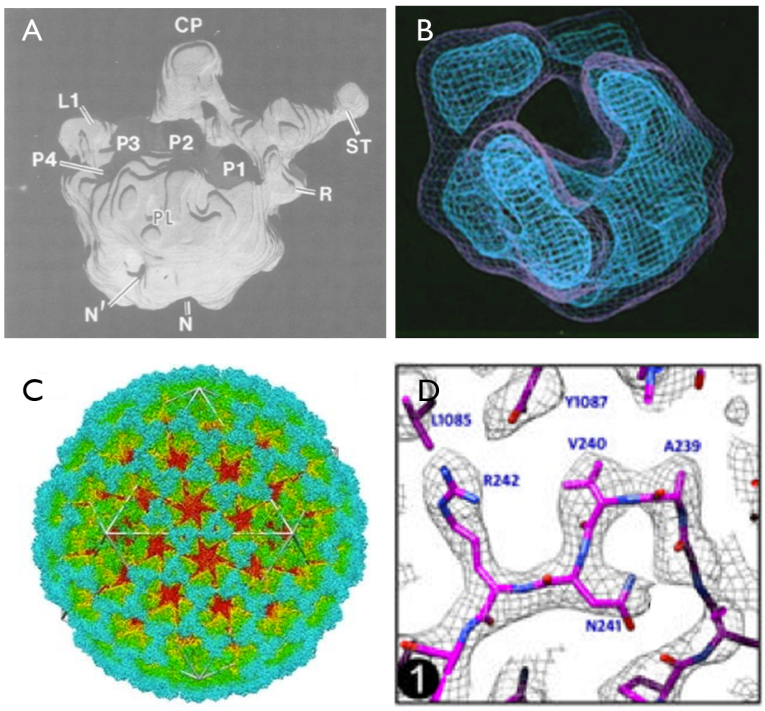

Figure 1 Single-particle EM reconstructions of different complexes.

A: Rademacher et al. 1987. Surface representation of the 50S subunit of the *E.coli* ribosome. CP central protuberance, BK back knob, N and N' notch and minor notch, L1 ridge containing ribosomal protein LI, P1-P4 pockets 1-4, PL plateau, R ridge, ST stalkcontaining ribosomal proteins L7 ands L12.

B: Frank et al. 1991. Computer-graphical representation of merged reconstruction in stereo view. Magenta: outer envelope of the particle; cyan: envelope of ribososmal RNA.

C,D: Zhang et al. 2010. **C,** density map of the aquareovirus ISPV at 3.3 Å. **D,** cryo-EM density (mesch) on boxed region showing representative side chains.

In the recent past important innovations emerged like the development of new electron detectors (Milazzo et al., 2011; Bammes et al., 2012), energy filters, phase

plates (Walter et al., 2012; Nagayama, 2014) in combination with new powerful processing algorithm (Scheres, 2012). Together they allowed to achieve near-atomic and atomic resolution for non-symmetric proteins and membrane proteins (Bai et al., 2013; Liao et al., 2013; Allegretti et al., 2014; Amunts et al., 2014). This method also enabled the trapping of a conformational flexibility unnoticed in previous X-ray structures of individual subunits (Ciccarelli et al. 2013). Many excellent recent reviews on near-atomic and atomic SP analysis can be recommended (Orlova and Saibil, 2011; Lau and Rubenstein, 2013; Bai et al., 2015; Cheng, 2015; Henderson, 2015).

Of all technical improvements, here, exemplarily the one arising from detector developments will be explained shortly.

In SP cryo-EM, images of unstained proteins or protein complexes (particles) embedded in a thin layer of amorphous ice are recorded in a transmission electron microscope at cryogenic temperatures. These images present many copies of the same particle in random orientations. By the use of statistical algorithms the orientation of each particle is determined and a 3D map is calculated. Finally refinements are conducted to improve the resolution. However, recording EM micrographs of ice embedded samples in good quality is a problematic subject and limiting factors like image blurring or quality of the recording medium make it difficult (Li et al., 2013). One major limiting factor is the notoriously low **S**ignal to **N**oise **R**atio (SNR) of the micrographs, i.e., the ratio of the amplitude of signal to the amplitude of the background noise. Any cryo-EM investigation of biological samples tolerates only low electron doses to avoid radiation damage, which would destroy the biologic sample immediately and uncontrollably resulting in the loss of high resolution information. Unfortunately, at low SNR the orientation determination of particles in ice is very difficult and may even inhibit the reconstruction process. The SNR and thereby the contrast at a given low dose will only improve by increasing the number of averaged images of identical particles. Consequently a large number of particles or a high symmetry were required to improve resolution. However, a major improvement of the low dose-SNR problematic came from developments in the recording media.

Until lately electron microscopy images were recorded on photographic film or with detectors based on the CCD (charged-coupled device) technique. CCD cameras used a scintillator to convert electrons into light at visible range lowering the DQE (Detective Quantum Efficiency) extremely. DQE is related to the amount of additional noise added by the detector. New direct detector device (DDD) cameras provide a way to collect data at lower doses even with increased SNR. These detectors are able to detect the electrons directly in a silicon layer without the need for a scintillator with an improved DQE. Ideally the DQE would be 1 but most detectors show a DQE of less than 1, e.g. in comparison photographic film shows an equal or even lower DQE as direct electron detectors (McMullan et al., 2009; 2014). Beam induced movement of the particles occurs permanently during the exposure and was described by Brilot et al. 2012. The very fast read out of the DDD cameras allow dose fractionating and recording a series of subframes that are summarized to one micrograph showing better SNR and contrast. The subframes of the image stacks can be aligned against each other and the limiting factor, the beam induced particle movement, can be corrected (Bai et al., 2013). In conclusion, the lower electron dose leads to images that are less influenced by radiation damage, and by summarizing subframes the contrast is preserved and high-resolution information is retained (Li et al., 2013).

Recently it could be shown that the first subframe of an image stack holds the most particle movement while the last frames are affected by radiation damage (Brilot et al., 2012; Campbell et al., 2012; Allegretti et al., 2014). By aligning only certain subframes of an image stack high-resolution information is preserved and images with higher SNR can be used for further 3D reconstructions.

For SP analysis a high sample quality with respect to protein purity, monodisperisty and particles in different orientations (Figure 21) are required to gain various particle-projections in different orientations. Nevertheless, a huge advantage of the method is that only a small amount of protein sample is necessary for data collection, a condition that cannot be realized in crystallography for instance. If the specimen is heterogeneous, additional classifications help investigating the data set further (Lyumkis et al., 2013). In the case of the fatty acid synthase of the *Mycobacterium tuberculosis* for instance, different functional states of the protein

could be identified via classification (Ciccarelli et al., 2013). Another resolution-limiting aspect is the flexibility of complexes. Proteins with high flexibility are found in different shapes so that the protein densities of particles in the same position cannot be averaged well resulting in a blurry map with low resolution. Nevertheless, most available techniques (fluorescence, NMR, crystallography) are limited for finding flexibility but SP analysis is the method that provides important functional information of flexible macromolecular assembly (Campbell et al., 2014).

The investigation of the functional flexibility and conformational changes which occur under activation of the stressosome complex required to take advantage of the aforementioned latest developments in cryo-EM data collection by DD as well as image processing. Especially latter had to be adapted to the specific problem of conformational flexibility in the stressosome and the detailed description of the method and its adaption is part of the results section.

1.2 The *B. subtilis* stressosome – a signal mediator in general environmental stress response

Bacteria are constantly exposed to changing environmental conditions with severe consequences on their ability to thrive and live. The detection and if possible immediate adaptation to stressful situations is most essential for their survival. One general response to environmental stress is the upregulation in transcription of genes encoding for stress response proteins, e.g., in the case of osmotic stress the enhanced expression of osmolyte transporters. In some bacterial species this transcriptional stress regulation involves a cytoplasmic mega Dalton complex, the so-called stressosome. In general, transcription depends crucially on the activation of σ factors enabling the RNA polymerase to recognize and bind to their promoter region. Transcription regulation upon stress is therefore directly linked to the controlled activation of the corresponding σ factor in order to become a subunit of the RNA polymerase. In a nutshell, the stressosome complex works as a signaling hub sensing various external stress stimuli including changes in salt concentration, temperature, pH, ethanol concentration, UV radiation or oxygen (Voelker et al., 1996; Hecker et al., 2007) and generating a single stress response, which is the activation of a transcription σ factor.

Genes encoding for the three stressosome subunits RsbR, RsbS and RsbT are found in the genome of several Gram-positive and Gram-negative bacteria, although they are not entirely conserved throughout the prokaryotic kingdom. If present, they are dominantly clustered in a conserved operon together with a set of varying regulatory interaction partner proteins (Pané-Farré et al., 2005). Despite many genetic and biochemical studies the molecular signaling mechanism, e.g., how the stress signal is perceived and transduced into a conformational response in the stressosome remains unknown.

The first and still the best-characterized stressosome complex is the one from the Gram-positive bacterium *Bacillus subtilis* (Dufour et al., 1996; Chen et al., 2003).

In *B. subtilis* the activation of the secondary sigma factor σ^B is regulated by environmental and internal metabolic stress (Hecker and Voelker, 1998). Binding of the activated σ^B initiates the General Stress Response (GSR) resulting in an up-regulation of the transcription of around 150 general stress genes within the large σ^B regulon. In 1996 the Rsb (Regulator of σ_B) proteins encoded by the Rsb operon were identified as key players in the activation of σ^B (Dufour et al. 1996). Later, genetic and biochemical studies indicated the presence of a stressosome complex composed of these Rsb proteins (Chen et al., 2003; Kim et al., 2004; Delumeau et al., 2006; Reeves et al., 2007). The capability of RsbR and RsbS to self-assemble *in vitro* to a 1.5 MDa stressosome complex was observed initially by negative stain EM in 2003 (Chen et al.). In 2008 first insights into the architecture of the *Bacillus* stressosome was provided by single-particle cryo-EM (Marles-Wright et al., 2008). Due to the high homology of stressosome proteins from different species it is assumed that stressosomes in general share this overall architecture (Pané-Farré et al., 2005).

RsbR, S and T are present within the complex in multiple copies (Figure 2A). RsbS is a single STAS domain protein (Sulphate Transporter and AntiSigma factor antagonist) and the antagonist of the kinase RsbT. STAS domains have a very conserved overall fold (Figure 2B) and are found in bacteria, archaea and in eukaryotes, e.g., in the human anion transporter SLC26 (Aravind and Koonin, 2000, Sharma et al. 2014). RsbR is a co-antagonist of RsbT. It is the largest protein in the stressosome with around 30 kDa (Chen et al., 2003). In RsbR, a N-terminal sensor and C-terminal STAS domain are connected via a linker helix (Marles-Wright et al., 2008). RsbS and the STAS domains of RsbR (Figure 2A, blue) constitute the main scaffold, the so-called central core of the complex and together they sequester RsbT (Figure 2A, purple).

Thereby, the STAS domains of RsbR and RsbS appear as homodimers and assemble into a pseudo-icosahedral rigid scaffold. Chen et al. described in 2003 the dimerization of RsbR monomers *in vitro* and discovered that even RsbR proteins alone are capable to form large complexes. Mutagenesis studies showed that in the absence of all RsbR paralogs no regulation by the stressosome is apparent resulting

in an active σ^B factor and continuous transcription of the σ^B operon (Akbar et al. 2001).

In *Bacillus*, five different paralogs (RsbRA-D and YtvA) are known, which differ in their N-terminal domains (Figure 2, yellow), but share the C-terminal STAS domain (blue) with a sequence identity of 45 – 50 % (Murray et al. 2005). The N-terminal domains of RsbR paralogs are considered to play an important role as sensor in signal detection. Interestingly, only RsbRA is present in the Rsb operon, while the others are scattered over the whole genome. RsbRA is assumed to be the most general Rsb protein with respect to stress sensing (Eymann et al., 2011). The N-terminal domains of RsbR face away from the central core (Figure 2A, yellow).

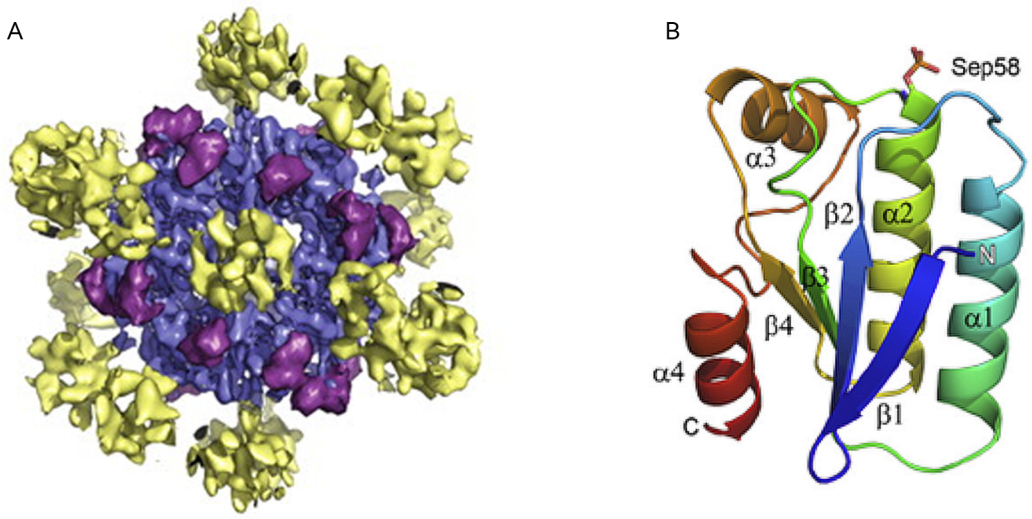

Figure 2 Stressosome of *B. subtilis*

A: Stressosome of *B. subtilis* (adapted from Marles-Wright et al., 2008), **B:** STAS domain protein (adapted from Quin et al., 2012).

A The stressosome is composed of three proteins RsbR, RsbS and RsbT. The blue core consists of the C-terminal STAS domain of RsbR and the single STAS protein RsbS. The N-terminal domains of RsbR are pictured in yellow and face away from the core. In between the N-RsbR domains the kinase RsbT is sequestered, shown in purple, located above the RsbS proteins.

B A typical STAS protein, the RsbS homolog from *Moorellla thermoacetica* (*Mt*S). The helices are rainbow colored. The overall arrangement of STAS domains shows four α-helices that enclose the four β-sheet assembly. C marks the C-terminal and N the N-terminal end. The STAS domains of the stressosome proteins possess phosphorylation sites here the Ser-58 at helix α2is displayed.

The ratio of RsbR:RsbS:RsbT in the *Bacillus* stressosome was shown to be 40:20:20 (Pané-Farré et al., 2005; Marles-Wright et al., 2008), although it is not known to date which one of the RsbR paralogues are present in the stressosome *in vivo*. It is assumed that the stressosome comprises a variation of the different RsbR types, but their stoichiometry might be regulated by the specific environmental conditions. Several studies of the stressosome are conducted with a stressosome composed of only RsbRA, RsbS and RsbT (Eymann et al., 2011; Gaidenko and Price, 2014) and these data confirm that a minimal stressosome is sufficient for environmental stress signaling (Kim et al., 2004 (a)). Subsequently, structural studies were performed with this minimal stressosome complex.

The first 3D map of the *Bacillus* stressosome revealed that RsbS and the RsbRA STAS domains form a quasi-icosahedral core with 30 2-fold axes. The outward pointing N-RsbR are located on 20 of the 2-fold axes according to a symmetric pattern that results in a D2 point-group symmetry, hence, the RsbR proteins are not randomly arranged within the complex.

1.2.1 Functional biology of the stressosome

The reaction pathway of the stress transmission for environmental stress conditions and the activation by energy stress is depicted in Figure 3. Both pathways lead individually to the activation of the GSR (general stress response) in *B. subtilis*.

Under external stress conditions the phosphorylation of RsbR and RsbS is conducted by the kinase RsbT and results in the release of RsbT from the complex initiating a partner-switching cascade, basically controlled by phosphorylation, (Hecker at al., 2007, illustrated in Figure 3). The released positive regulator RsbT activates the environmental phosphatase RsbU (Delumeau et al., 2004). RsbU in turn dephosphorylates RsbV-P, which also comprises a STAS domain. This dephosphorylating step triggers the partner-switching of the anti-σ factor RsbW. The affinity of RsbW to non-phosphorylated RsbV is 8-fold higher than to σ_B factor (Delumeau et al., 2002). Thus RsbW is forced to switch partner and releases the σ_B

factor that in turn binds to the RNA polymerase. In the absence of stress, σ_B is held inactive due to the interaction with anti-σ RsbW. The anti-anti σ factor RsbV is rephosphorylated by the kinase RsbW and later on released from RsbW, which is then free to inactivate the σ_B factor again.

Intracellular energy stress is transmitted by the RsbP phosphatase via partner-switching from RsbQ. RsbP dephosphorylates RsbV-P as well as RsbU by environmental stress in order to initiate the GSR (Figure 3). To reset the stressosome components the feedback phosphatase RsbX dephosphorylates the phosphorylation site Ser-59 of RsbS-P and Thr-205 of RsbR-P (Chen et al., 2004), (Figure 7). Thus the RsbX kinase activity counteracts RsbT by dephosphorylating RsbS (Yang et al., 1996).

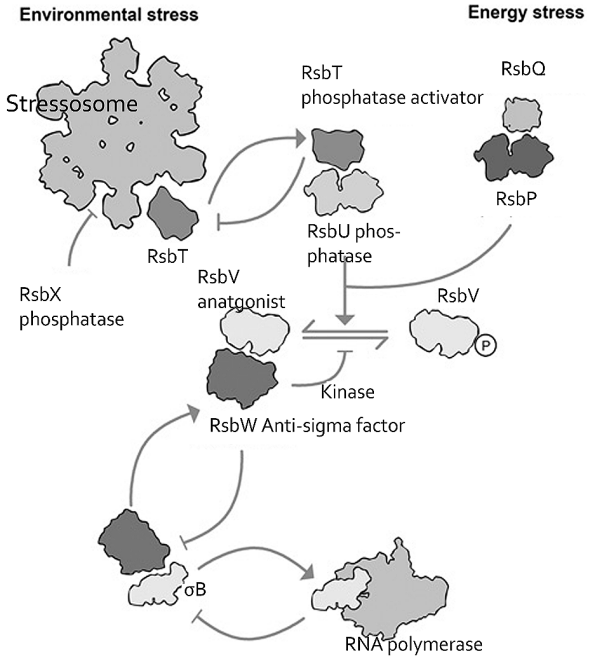

Figure 3 The release of σ^B occurs due to partner-switching cascade (adapted from Marles-Wright and Lewis, 2010.)

Two pathways lead to the activation of σ^B, environmental and energy stress. The stressosome mediates the first way and the RsbQ conveys the second.

1.2.2 Genetic organization of the Rsb proteins

All seven regulators shown in Figure 3 contributing to the control of σ^B-dependent activation are clustered together with the *sigB* gene in an eight-gene operon (Figure 4). These regulator genes and the *sigB* gene itself are controlled by the σ^B factor (Dufour et al. 1996). In the same operon the proteins of the stressosome complex are located upstream from the regulator part in a so-called RST module (Pané-Farré et al., 2005). *rsbR*, *rsbS* und *rsbT* together with *rsb*U form the so-called input module for the environmental stress pathway (Figure 3). They are under the control of a σ^A-dependent promoter. The σ^A factor is the housekeeping σ factor in *B. subtilis* that participates in the initiation of transcription of most of the housekeeping genes (Jarmer et al., 2001) and is independently activated from σ^B (Wise and Price, 1995).

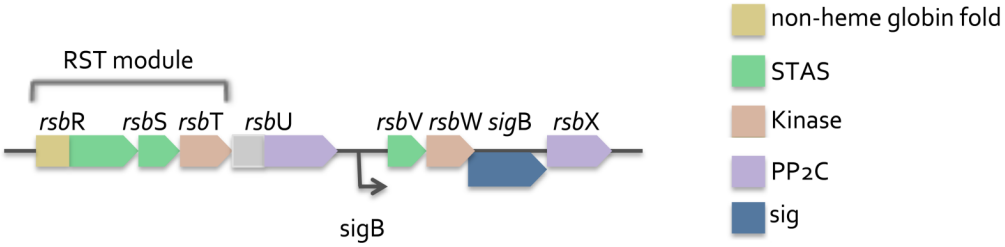

Figure 4 Operon structure of the 8 regulator genes of σ^B in *Bacillus* and *Listeria* (modified after Hecker et al., 2007).

The *rsb*RST genes are encoded in a conserved motif: the RST module that is located upstream. The four paralogs of RsbRA (RsbRB, RsbRC, RsbRD, and YtvA) are not encoded within the σ^B operon but spread around the *B. subtilis* chromosome. The genes of the σ^B regulators and members of the partner switching event are located downstream.

Right panel: Non-heme globin (structurally related to globins); STAS (Sulphate Transporter and AntiSigma factor antagonist); Kinase (enzyme that transfers phosphate groups); PP2C (serine/threonine phosphatase); sig (sigma gene); arrow: sigB-dependent promoter of the σ^B operon.

As aforementioned only *rsbRA* is located within this operon, the genes of the RsbR paralogs are spread over the whole genome. The phosphatases RsbP and RsbQ, responsible for transmission of internal energy stress (Figure 3) are not encoded

within the eight-gene operon but in close proximity to the regulator genes.

The RST module is a very conserved motif and can be found in a wide variety of bacteria e.g. in different *Bacillus* and *Listeria* species, *Vibrio vulnificus*, *Moorella thermoacetica* or *Mycobacterium avium* (Pané-Farré et al., 2005). This conserved RST module indicates that the stressosome proteins are adapted from several Bacteria species to compose a signal sensing complex that relays information to regulatory target components (Pané-Farré et al., 2005; Quin et al., 2012).

1.2.3 The stressosome proteins

1.2.3.1 Structure and function of STAS domains

STAS domains exhibit a conserved fold of 4 β-strands enclosed by 4 α-helices that form a characteristic alpha-helical handle-like structure (Kovacs et al., 1998; Aravind and Koonin, 2000; Sharma et al., 2011 (a), (b)). A common and important function of the STAS domain seems to be the participation in protein-protein interactions.

Nevertheless, the specific functions differ in single-STAS domain and multidomain STAS proteins. The transduction of light, oxygen, phosphates and GTP-binding proteins, as well as functions in sensing, metabolism or transport of nutrients such as sugar, amino acids, lipids, anions and vitamins are reported (Sharma et al., 2011 (a)).

STAS domain proteins are classified as following: I) bacterial anti-sigma factor antagonist of σ^F, II) bacterial anti-sigma factor antagonist of σ^B (stressosome proteins) and III) anion transporters like the Sulfate Permease SulP of bacteria, plants as well as the human SLC26 anion transport proteins.

In bacteria, STAS domains proteins are dominantly involved in stress response strategies. The signal cascade for activation of the alternative σ^B factor to counteract more frequently occurring stress was already discussed in detail in the previous chapter (Figure 3). Another example is the sporulation activation as response to extreme stress.

In fact the sporulation process is another intriguing stress adaptation mechanism based on a phosphorylation/de-phosphorylation events, which is however not regulated within the GSR mediated by σ^B. Sporulation is one of the most extreme examples for stress-survival strategy in bacteria and is controlled by the bacterial σ^F antagonist in *B. subtilis*. σ^F interacts with three regulators, the sporulation factors SpoIIAA, another STAS domain protein, SpoIIAB and SpoIIE. The phosphorylation of SpoIIAA by SpoIIAB leads to induction of the sporulation and SpoIIE is able to reset the system by dephosphorylating SpoIIAA. Although the activation process is very different, there are homologies between the kinase RsbT and SpoIIAB, which share 28 % sequence identity. In the aforementioned 3D map of the *Bacillus*

stressosome SpoIIAB was used as template for generating a homology model *Bs*RsbT.

Other examples for the involvement of STAS domains in stress strategies are the perception of blue light by the RsbR paralog YtvA and the SulP transporter in cyanobacteria. The SulP transporter comprising STAS domain is involved in inorganic carbon uptake being part of nutrition stress response. In addition interactions of the STAS domains with other transporters or cytoskeletal scaffolds are reported (Sharma et al., 2011 (a)). Molecular dynamics simulations, carried out by Sharma et al. in 2014, revealed essential conformational changes of mammalian STAS domains that occur during signal influence.

1.2.3.2 The sensory N-terminal non-heme globin domain

The N-terminal domains of the RsbR parlogs (RsbRA, RsbRB, RsbRC, RsbRD and YtvA) share a globin fold with a sequence identity ranging between 17-22 %. Therefore, it is assumed that different RsbR paralogs sense different stimuli, although physical triggers for the activation of the stressosome in *B. subtilis* are unknown to date. One exception is YtvA, which is the blue-light sensor protein of *B. subtilis* (Gaidenko et al., 2006; Avila-Pérez et al., 2006). In addition, paralogs RsbRA-D can replace each other functionally (Steen et al., 2012).

Despite the similar fold there is nearly no sequence similarity between N-terminal RsbR-type globin and heme-binding-globins. For instance, the *B. subtilis* N-RsbRA shares a sequence identity of only 13.5 % with HemAT (Figure 5B). HemAT is a monomeric globin-coupled sensor that binds heme for oxygen sensing and transmits a signal to regulatory proteins that control the oxygen-dependent aerotaxis in *B. subtilis* (Zhang and Philips, 2003). HemAT is mentioned at this point because oxygen sensing plays a major role in the *Vibrio vulnificus* stressosome, which will be discussed later.

In 2005 Murray et al. solved the crystal structure of the N-terminal domain of RsbRA to 2 Å (Figure 5A). The structure reveals a dimerization of the N-terminal domain similar to what was observed for the STAS domain before (Chen et al., 2003).

Different to other heme-containing globins the corresponding α-helices in RsbRA are arranged closer together, filling the heme-binding site. A conserved histidine residue being responsible for the iron coordination in heme-binding globins is replaced by an alanine in N-RsbRA.

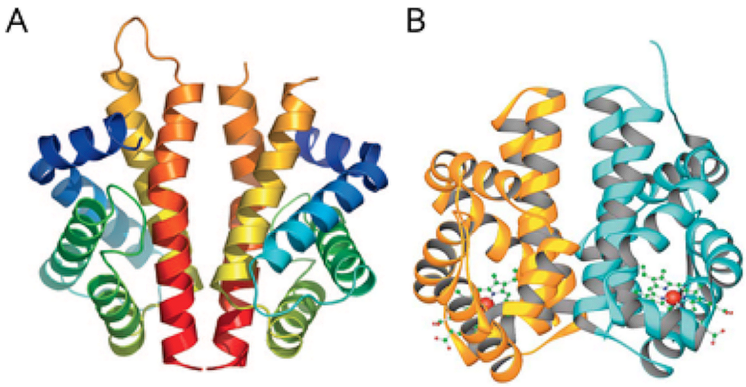

Figure 5 Dimer of the N-RsbR and dimer of the HemAT.

A: Structure of the N-RsbR dimer (Murrey et al., 2005 (PDB accession number: 2BNL)), **B:** structure of the HemAT dimer (Zhang and Philips, 2003 (PDB accession number: 1OR6)). N-RsbR is a non-heme globin sensor domain and HemAT an oxygen sensing globin coupled sensor, both are sensory proteins in *Bacillus subtilis*. N-RsbRA in A is illustrated in rainbow colors for every monomer; the N-terminus is blue and C-terminus red. Six helices are present in one monomer. In B the HemAT monomers are colored differently (yellow and blue) and each consists of eight α-helices. The cofactor heme is located, proximally.

The N-terminal and the C-terminal part of RsbR paralogs are connected by a conserved linker helix (Figure 6). These linker helices located between the sensor and effector STAS domains play a crucial role in signal transduction (Gaidenko et al., 2012). Conserved and non-conserved residues are located on opposite sides of the helix. Gaidenko et al. suggested, that the two sides of the helix interact with different partners *in vivo*, one side is a part of the RsbRA dimerization and the non-conserved side is involved in inter- and intramolecular contacts that regulate stressosome function. Mutations of the five conserved linker residues (Figure 6, magenta) increased activation of the transcription factor in unstressed *Bacillus* cells, while mutations at the five non-conserved positions (Figure 6, blue) decreased the

activity of σ^B in unstressed cells. Substitutions on residues responsible for dimerization show in unstressed cells a 30-fold increased stressosome output, transcription activity, but had no effect in salt or ethanol response.

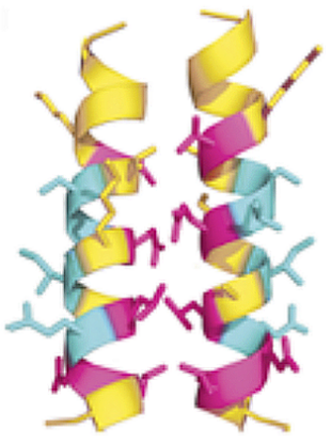

Figure 6 Model of the linker helix of RsbRA of *B. subtilis* adapted from Gaidenko et al., 2012
The linker is displayed as dimer since the N-terminal domains exhibit dimerization. Conserved and output increasing residues are shown in magenta. The non-conserved decreasing activity residues are displayed in blue. Substitutions of yellow residues show no effect.

One possible explanation for the crucial functional role of the linker helix in RsbR paralogs, conveying the stress signal might be found in an alteration of the dimerization properties, which in turn affect the core of the stressosome.
In order to determine the nature of stimuli sensed by RsbRA, substitutions of surface exposed residues in the N-terminal domain were performed (Gaidenko et al., 2011). Some of the N-RsbR substitutions indeed increased the activity of σ^B upon various stress types (except for ethanol stress), which could be monitored by an elevated transcription level. The activity of the σ^B factor was not affected by deleting one or several *rsb*R genes, only *rsbR* null mutants show a σ^B factor which is not able to receive. Concidering this as well as the former mentioned results of the genetic studies regarding the linker helix, Gaidenko et al. concluded that the liker helix could be a part of the sensory unit of RsbRA.

While the stimuli of RsbRA-D remain unidentified, the stimulus for YtvA is well-known (Avila-Pérez et al., 2006; Jurk et al., 2011). YtvA belongs to the LOV (**L**ight **O**xygen **V**oltage) family of blue light photoreceptors. LOV domains are conserved in sensory and regulatory proteins in bacteria, plants and fungi (Losi, 2007; Möglich et al., 2010; Herrou and Crosson, 2011). The LOV domain of YtvA binds a flavin cofactor, when exposed to light of a wavelength of 450 nm functioning as a photoreceptor *in vitro* and *in vivo* (Ávila-Pérez et al., 2006; Buttani et al. 2006). Again a major role is assigned to the linker helix between sensor and STAS effector. A conserved cysteine residue forms a covalent bond to the flavin that leads to modifications of the hydrogen bond network around the flavin chromophore generating a conformational change in which the linker helix undergoes a rotational movement that activates the C-terminal effector STAS domain (Möglich and Moffat, 2007; Herrou and Crosson, 2011).

1.2.3.3 Phosphorylation of RsbR and RsbS by the serine-threonine kinase RsbT

In the stressosome phosphorylation plays a crucial role in the signal transduction mechanism and initiated signaling cascade. Phosphorylation is a general regulatory mechanism that induces conformational changes in proteins by kinase activity. The kinase adds a phosphatase group to a substrate by binding ATP and as consequence the function of the target protein is modified.

The serine/threonine kinase RsbT phosphorylates the STAS domains of RsbS at a conserved serine residue under stress conditions (Figure 7) (Akbar et al. 2001; Kim et al., 2004 (b)). In RsbR, two conserved threonine residues (Thr-171 and Thr-205) were identified (Gaidenko et al. 1999, Pané-Farré et al., 2005). Interestingly, these two residues are not conserved in the paralog YtvA, hence YtvA is the only known RsbR paralog where no phosphorylation takes place (Akbar et al., 2001).

Although the RsbR phosphorylation state is important for the stressosome mechanism it is not clear to date, if RsbT phosphorylates RsbR. Previous findings (Eymann et al., 2011) demonstrated that RsbR Thr-171 is already phosphorylated in unstressed cells (Figure 7). Thr-205 is only phosphorylated under extreme stress

conditions but limits σ^B activation as a second feedback tool (Eymann et al., 2011). This brings RsbS into the focus of the signaling mechanism by phosphorylation.

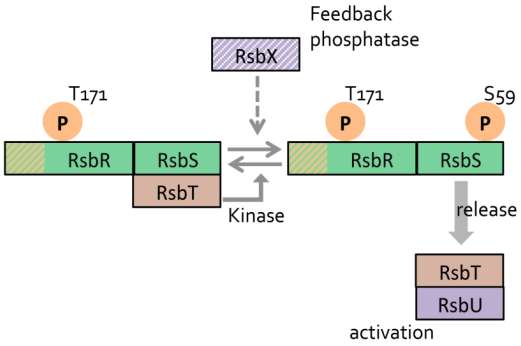

Figure 7 Phosphorylation of RsbS under moderate stress conditions (adapted from Gaidenko and Price, 2014)

The same color scheme as in Figure 4 was applied. Thr-171 is phosphorylated (yellow circle with P) under non-stress conditions and the RsbT kinase is bound to RsbS. Upon stress Ser-59 is phosphorylated, which goes along with the release of RsbT and assembles to an interaction complex with RsbU. RsbX is the feedback phosphatase that dephosphorylates Ser-59 to reset the system.

The stressosome contains 10 RsbS dimers (Marles-Wright et al., 2008). RsbS cannot form higher oligomers in absence of RsbR and no RsbS paralogs have been identified within the *B. subtilis* genome. The STAS domain of RsbS has only a single phosphorylation site (Ser-59), which is phosphorylated by the RsbT kinase (Kim et al., 2004 (a)) (Figure 7). Non-phosphorylated RsbS has a high affinity to RsbT (Kim et al., 2004 (a)) forming interaction aggregates in the absence of RsbR *in vitro*. Under non-stress conditions RsbS binds RsbT to the stressosome and RsbT is hold inactive (Chen at al., 2003; 2004). *In vitro* no interaction aggregates between RsbRA and RsbT are observed. RsbRA is assumed to promote the phosphorylation of RsbS most likely by an interaction with RsbT increasing kinase activity to phosphorylate RsbS during signaling. Response to very high stress levels was also obtained in strains where only two RsbR paralogs (RsbRA and RsbRC) and no RsbS was present, which demonstrated that under extreme conditions a phosphorylation of RsbR by

RsbT can initiate the signaling cascade (Gaidenko et al., 2011). These data are supported by recent studies about substitutions of Ser-59 that showed no response to minimal stress but a response of 60% WT activity under elevated stress conditions. Apparently different pathways exist in parallel for stressosome activation affecting stressosome sensing and signaling. The functional role of interactions between RsbS, R and T remains an open question und is topic of further studies in the stressosome field.

1.3 Diversity of stressosome sensing mechanisms

σ factor regulating *rsb* genes could also be identified in other bacteria (Firmicutis, Actinobacteria, Cyanobacteria, Proteobacteria, Deinococcus and Bacteriodetes) (de Been et al. 2011; Quin et al., 2012; Pettersson et al., 2013).

The upstream RST module is often but not always conserved in *rsb* containing bacterial species, while the downstream genes can encode very different proteins, although these proteins are all more or less involved in signal transduction and stress regulation (Pané-Farré et al., 2005).

Bacillus and *Listeria* belong to the same phylum of the Gram-postive Firmicutes and are close relatives. They share the regulatory downstream genes within the σ^B operon (Pané-Farré et al., 2005; Hecker et al., 2007). For *Listeria monocytogenes* and *B. subtilis* the physiological role of the stressosome was identified to a large extent, e.g., the activation of the sigB GSR to counteract environmental stress (Shin et al., 2010; Price 2010).

L. monocytogenes is an important food-borne pathogen that causes 2500 listeriosis cases per year affecting immuno-compromised persons. It is lethal in approximately 30 % of the infections (Disson and Lecuit, 2012). As the expression of virulence factors is controlled by the σ^B activation the stressosome is involved in pathogenicity (Raengpradub et al., 2008). The RsbR homolog of *L. monocytogenes* when expressed in *B. subtilis* participated at the formation of stressosome complexes that were able to activate σ^B by energy and nutritional stress (Martinez et al., 2010). Often investigations on the *Listeria* stressosome were conducted in the nonpathogenic *Listeria innocua*, which is the closest relative to *L. monocytogenes* among the *Listeria* species (Glaser et al., 2001). The activation of the RST module is assumed to be comparable within both organisms. In this thesis, too, *Listeria innocua* was used as a model system to investigate the *L. monocytogenes* stressosome.

Quin et al. classified the stressosome proteins from *Moorella thermoacetica* as well as the stressosome-regulated biochemical pathway in 2012. In the stressosome operon of *M. thermoacetica* no σ factor is present, the homologues of RsbR, S and T are called *Mt*R, *Mt*S and *Mt*T. Adjacent to *rsbs*, a two-component system is located

comprising a RsbX-like phosphatase. It was suggested that the RsbX-like phosphatase is responsible for resetting the system by dephosphorylation of the R and S components. Afterwards, a diguanylate cyclase follows including a GAF domain. GAF domains serve as receptors for GMP and synthesize c-di-GMP, a second messenger in many bacteria, that is involved in the regulation of adaptive responses like motility, biofilm formation or virulence in bacteria species as *Vibrio*, *Salmonella* or *Caulobacter*.

The structure of the *Mt*N-R protein was determined to 2 Å resolution by x-ray crystallography revealing an similar structure to the *B. subtilis* N-RsbR despite only 12 % sequence identity (Quin et al., 2012). The kinase *Mt*T was identified that acts towards *Mt*S and phosphorylates Ser-58. Negative stain EM revealed that the *Mt*R and *Mt*S self-assemble to the stressosome complex.

In the pathogen *Vibrio vulnificus* the arrangement of the RST gene cluster and the downstream open reading frames are similar to *Moorella*. There is no sigma-depending gene transcription for the downstream module, however a two-component system could be detected including a sensor kinase and a response regulator (Pané-Farré et al. 2005). Comparable to *M. thermoacetica* the downstream genes encode a diguanylate cyclase including a GAF domain that synthesizes c-di-GMP from GTP. In the marine pathogen *Vibrio cholerae* the level of c-di-GMP probably serves as an inductor for virulence (Tischler and Camilli, 2004), which suggest for *V. vulnificus* a RST module coupled virulence-factor control.

The RsbR and RsbS homologs of *V. vulnificus*, *Vv*R and *Vv*S, share the conserved phosphorylation sites in the STAS domains with the *B. subtilis* stressosome proteins (Figure 8). In contrast to *B. subtilis* only one RsbR homolog is present in the *V. vulnificus* genome (*Vv*R). Besides, sequence analysis of Pané-Farré et al. in 2005 identified for the N-terminus of *Vv*R a sensor globin domain that binds heme as a cofactor (Freitas et al. 2003). As many heme–based sensors *Vv*R use the ability of the co-factor to reversibly bind oxygen for the regulation of oxygen dependent conformational changes inside the protein. Unpublished data by the group of Jan Pané-Farré in Greifswald support the assumption of oxygen sensitivity of the *Vv*RS complex via the heme cofactor within the N-*Vv*R protein. An oxygen-dependent absorption spectrum reveals the transition from the reduced and oxidised

stressosome complexes when sodium dithionite was added to reduce Fe^{3+} to Fe^{2+}. The Soret peak shifted from 414 nm to 431 nm accompanied by a shift from red for the oxidized *Vv*RS to yellow for the reduced *Vv*RS indicating a complete redox reaction.

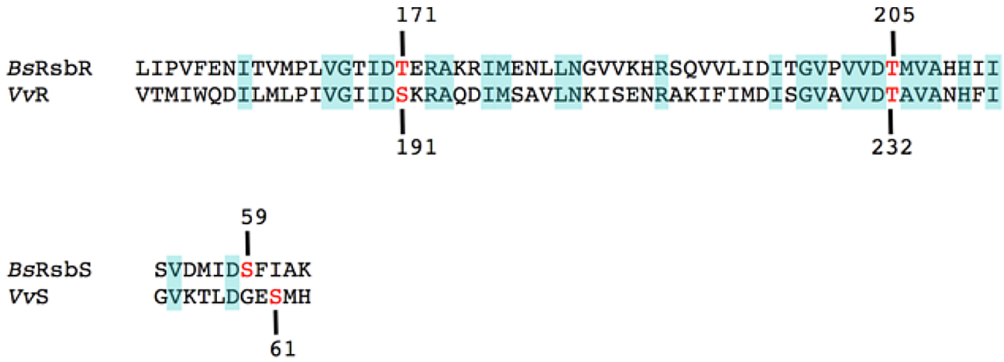

Figure 8 Sequence analysis of *B. subtilis* and *V. vulnificus* RsbR and RsbS homologs

The conserved phosphorylation sites are marked in red. The *Vv*R sequence exhibits two phosphorylation sites. The threonine 171 is replaced by a serine at position 191. The serine residue in *Vv*S is shifted about two positions. Identical sequences are marked in blue.

Oxygen stress can lead to changes in transcription or motility, e.g., the heme-containing oxygen sensor of *B. subtilis*, Hem-AT, is involved in aerotaxis. Similar to HemAT, N-*Vv*R comprises of the conserved histidine residue (Figure 9) that is essential for oxygen binding and coordination (Yoshida et al., 2012).

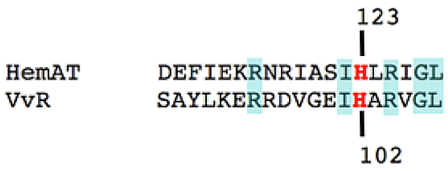

Figure 9 Sequence alignment of the sensor globin domains of HemAT and *Vv*R

The conserved proximal histidine residue at position 123 in HemAT (red) is also present in N-*Vv*R at position 102 (red). Identical sequences are marked in blue. Sequence identity of both N-terminal domains is 24 %.

In conclusion, it is assumed that the trigger for the *V. vulnificus* RST module is oxygen that is sensed by N-*Vv*R and further activates the stressosome dependent stress response. The presence of only one sensor protein (*Vv*R) in *Vibrio* and the known trigger for activation allow investigations of the activated and inactivated form of the RST module under controlled conditions.

Biofilm formation is a survival strategy of many microorganisms including *V. vulnificus* and its close relative *V. cholerae* to counteract harsh environmental conditions. The biofilm formation in *V. cholerae* is combined with toxin-generating mechanisms (cholera toxin and toxin-coregulated pilus), which represent important virulence factors causing cholera. For *V. vulnificus*, an opportunistic human pathogen, capsular polysaccharide (CPS) production and biofilm formation are thought to be crucial for disease progression. Since *V. vulnificus* is a facultative organism generally considered to be oxygen-tolerant the sensitivity to oxygen stress shown by Tamura et al. in 2012 was surprising. They discovered that hyperbaric oxygen (HBO) is an effective therapy for *V. vulnificus* infections. *V. vulnificus* is not able to repair strong oxygen DNA damage caused by reactive oxygen species (ROS). Phippen and Oliver reported in 2015 about reduced biofilm formation in the absence of oxygen and proposed that when oysters infected with *V. vulnificus* are eaten the change to anaerobic conditions would lead to planktonic lifestyle to move within host. When the oxygenated bloodstream is reached the genes for CPS are up-regulated and the encapsulated cell can bypass the immune system, causing fetal septicemia. Oxygen detection is fundamental for the organism to survive. For host infection the switch from sessile to planktonic lifestyle is an important factor in the virulence and by oxygen sensing the stressosome play an important role in this process. By blocking the oxygen detector of the pathogen, infections could be controlled.

Summary: In this work the structure-function relationship of stressosome complexes of two bacteria species of different phyla *Vibrio vulnificus* (Proteobacteria) and *Listeria innocua* (Firmicutes) were investigated. Both bacterial species comprise the conserved RST module that encodes the stressosome proteins within the genome but differ significantly in their signaling and regulation mechanism. In order to examine the stressosome assembly in *Listeria* species we investigated a close relative to the human pathogen *Listeria monocytogenes*. The proteins of the RsbRST paralogs of *L. innocua* were expressed, purified and complex formation was investigated. To gain insights to the environmental stress sensing mechanism in *Listeria* could provide basic information to control pathogens like *L. monocytogenes*, e.g., by inhibiting general stress response, which might affect the survival of this pathogen during host infection.

Further structural studies of the human pathogen *V. vulnificus* stressosome were performed.

Since the stressosome is a large macromolecular complex with high symmetry single-particle analysis is the perfect tool for structure determinations. Single components of the stressosome were already investigated by X-ray crystallography as the described *Mt*S and N-*Bs*RsbR but the stressosome was never structurally studied in an activated and inactivated form. The *Vibrio vulnificus* complex provides ideal conditions for the investigation of the active (oxidized) and inactive (reduced) form and for identifying conformational changes of the sensing domains or movements in core that take place in different states. We first focused on single-particle analysis with the oxidized *V. vulnificus* stressosome.

2. MATERIALS

Listed in the following are the utilized materials for *Listeria innocua* stressosome protein expression.

Table 1 Gens of *Listeria innocua* 6a (strain CLIP 11262)

gene	Properties		Reference
liR	837 bp, STAS domain protein	GenScript	Glaser et al., Science 2001
*li*S	357 bp, STAS domain protein	GenScript	Glaser et al., Science 2001
*li*T	411 bp, ATP binding protein	GenScript	Glaser et al., Science 2001

Table 2 Bacteria strains

Strain	Genotypes	Company
E.coli strain Bl21 (DE3)	F- ompT gal dcm lon hsdSB (rB-mB-) λ (DE3 [lacI lacUV5-T7 gene 1 ind1 sam7 nin5])	Invitrogen (Sambrook et al., 1989)
E.coli strain DH5α	F-Φ80lacZΔM15 Δ(lacZYA-argF) U169 recA1 endA1 hsdR17 (rk-,mk+) phoA supE44 λ- thi-1 gyrA96 relA1	Invitrogen (Killmann et al., 1996)
Listeria innocua	DSM No.: 20649, Type strain	(ex Seeliger and Schoofs 1979) Seeliger 1983

Table 3 Plasmids

Plasmid	Resistance	Properties
pET 11a	Amp	*rsbR* and *rsbS* cloned bicistorinic with additional ribosome binding site in between restriction sites *Nde*I and *Bam*HI
pGEX-6P-2	Amp	*rsbT* cloned in pGEX-6P-2 between *Bam*HI and *Not*I restriction sites

Table 4 Expression media

Medium	
Luria Bertani, LB-medium	10 g/l bacto trypton 5 g/l bacto yeast extract 10 g/l NaCl
Brain Heart Infusion Agar (Fluka)	
Brain Heart Broth (Fluka)	

Table 5 Purification buffers

Buffer	Composition
Lysis buffer	50 mM Tris-HCl, pH 8.3 10 mM EDTA 5 mM DTT (Dithiothreitol) 1 mM PMSF
Elution buffer I *Li*R:*Li*S (DEAE column)	50 mM Tris-HCl, pH 7.5 1 mM DTT 0 – 750 mM NaCl (depending on step)
Elution buffer II *Li*R:*Li*S (Superdex column)	200 mM NaCl 50 mM Tris-HCl, pH 8.5 1 mM DTT
BSA buffer	50 ml 1xTBS buffer 1.5 g BSA
Binding buffer *Li*T	PBS pH 7.4 140 mM NaCl 2.7 mM KCl 10 mM Na_2HPO_4 1.8 mM KH_2PO_4
Elution buffer *Li*T	50 mM Tris – HCl, pH 8.0 10 – 20 mM reduced Glutathione 1 mM DTT

Table 6 Buffer for 15 % SDS Gels

Buffer	Composition
5x sample buffer for SDS page	10 % w/v SDS (sodium dodecyl sulfate) 0.16 M DTT (250 mM) 30 % Glycerol (87 %) 0.25 M Tris-HCL, pH 6.8 (0.5 M) 0.4 % w/v bromphenol blue

Table 7 SDS gel

Components for 5 SDS gels	4 % stacking gel	15 % separation gel
0.5 M Tris-HCl; pH 8.6	1.3 ml	-
1.5 M Tris-HCl, pH 8.8	-	1.16 ml
Acryl amid (40%)	0.26 ml	11.25 ml
10 % SDS	200 µl	300 µl
H_2O_{dd}	17.8 %	10.83 ml
TEMED	25 µl	20 µl
10 % APS	100 µl	100 µl
Stain SDS gel		
Solution I: 50 % ethanol, 10 % acetic acid Solution II: 5 % ethanol, 7.5 % acetic acid Coomassie stock solution: 0.25 % Coomassie brilliant blue R250 in 95 % ethanol		

Table 8 Components for 1.2 % agarose gel

Solution	Composition
1 x TAE buffer (Tris acetat)	Tris-acetate pH8.0 40 mM Na_2EDTA 1 mM Acetic acid (100 %) 40 mM
EDTA (100 ml):	18.6 g EDTA with 10 M NaOH titrate to pH 8.0
Agarose gel (200 ml)	2.4 g agarose add 200 ml 1 x TAE 3 µl EtBr (Ethidium bromide)

3. METHODS

3.1 Protein production

3.1.1 General methods

The following paragraphs describe general methods that were applied in this work during the expression and purification of the *Li*RS proteins.

3.1.1.1 *Transformation*

The plasmid with the gene of interest was mixed with 100 µl freshly thawed *E. coli* BL21 competent cells and incubated on ice for 15 min. To open the membranes the cells were heat shocked for 45 sec at 42° C and afterwards placed on ice for 5 min. For cell division 100 µl of LB medium was filled into the transformation tray and after 1 h rotating at 250 rpm the cells were distributed on LB plates containing 50 µg/ml carbenicillin antibiotic and incubated at 37° C over night.

3.1.1.2 *Agarose gel electrophoresis*

To confirm the insertion of the gene a gel electrophoresis was implemented. The composition of the 1.2 % gel is displayed in Table 8. Before starting the agarose gel a restriction digestion was performed to separate the plasmid and the gene of interest. The restriction samples were mixed with 6 x DNA sample buffer before loading into the pockets of the gel. After 1 h at 100 V the DNA within the gel could be viewed under UV light due to the gel containing Ethidium bromide.

3.1.1.3 *SDS-polyacrylamide gel electrophoresis (SDS-PAGE)*

To produce a SDS gel the components for the separation gel (Table 7) were first loaded into the gel chambers and then topped up with the stacking gel solution. Pocket holders were placed into the chambers until the gels were polymerized.

For performing a SDS-PAGE the gel pockets were loaded with 15-30 µl sample in a ratio of 3:1 sample and sample buffer (Table 6), furthermore one pocket was filled with 5 µl marker (Prestained Protein Ladder, Fermentas). The electrophoresis was performed with the Mini Gel System from Biorad, the first 30 min at 80 kV until the proteins entered the separation gel and then continuing at 120 kV until the proteins were distributed.

After conduction of the electrophoresis the SDS gels were stained (Table 7) for the visualization of the single protein bands. The gel was placed in 50 ml solution I and heated in a microwave for ~30 sec. After five minutes at room temperature solution I was replaced with 50 ml of solution II and 200 µl Coomassie blue and again heated for ~30 sec. The bands appeared after a few minutes at room temperature.

3.1.1.4 *Western blot*

To confirm the expression of *Li*R and *Li*T specific antibodies were applied to certain SDS gels as described in the following procedure. Two layers of blot paper (Whatman), saturated with transfer buffer, were placed in the blot device Trans-Blot (Biorad Muenchen) (Table 9). The PVDF (polyvinylidene difluoride) membrane activated with 100 % methanol was positioned on the blot paper and the SDS gel was placed on top. Everything was covered with two more layers of blotting paper and the electrophoresis was performed for 35 min at 15 V.

To block unspecific binding of the antibody, the PVDF membrane was placed in TBS buffer with 3 % BSA (200 mM Tris-Cl pH 7.5; 1.5 mM NaCl). After 2 h of shaking the membrane was washed three times with TBS buffer and the primary specific antibody was applied (diluted 1:1000 in TBS buffer) and incubated for 1 h at room temperature. After washing three times in TBS buffer, the membrane was placed in

the solution of the second antibody (anti-mouse IgG, Sigma-Aldrich; 1:1000 diluted in TBS buffer) for 1 h at room temperature.

To visualize the specific binding, SIGMA*FAST*™ BCIP®/NBT tablets were dissolved in TBS buffer and the membrane was shortly incubated until the individual bands appeared.

Table 9 Western blot

Buffer	Composition
Transfer buffer	100 mM Tris-ac pH 8.3 0.2 % SDS 10 % methanol
TBS buffer	200 mM Tris-HCl ph 7.5 1.5 mM NaCl

3.1.2 Expression of stressosome proteins from *Listeria innocua*

3.1.2.1 *Cloning and expression of Li*R *and Li*S

The wild-type genes encoding for the *Listeria innocua* CAC96120.1 (*Li*R) and CAC96121.1 (*Li*S) (Table 1) proteins were cloned in a pET-11a vector (Novagen, 69436-3), using the *Nde*I and *Bam*HI restriction sites. Additionally, a ribosome-binding site was inserted in between (construct by GenScript). 5 µl of the plasmid pET-11a containing *Li*R and *Li*S were transformed in *Escherichia coli* DH5α cells and transferred onto plates with LB to receive single colonies. To gain an appropriate plasmid yield for the further work single colonies were picked for replication approaches in 20 ml LB medium. The subsequent plasmid preparation was performed using a QIAprep Spin Miniprep Kit (Qiagen). The DNA yield of plasmid was approximately 100 ng/µl.

Expression tests were performed in two different *E. coli* strains and revealed a successful expression of *Li*R and *Li*S in both DH5α and BL21. The BL21 strain was selected for this project. The transformation was performed as described before (3.1.1.1) and the proteins *Li*R, *Li*S were expressed in the following way: Overnight cultures were prepared whereby single colonies were picked from plates and added to 10 ml LB medium. These cultures were placed at 250 rpm and 37° C and on the next day every pre-culture was transmitted into 1 l of fresh LB. The proteins *Li*R and *Li*S were co-expressed in the presence of 1 mM carbenicillin in 1 l medium at 37° C with 120 rpm until an absorbance of 0.6 at 600 nm. Then the over-expression was induced adding IPTG to a final concentration of 1 mM. After 3 h the cells were harvested by centrifugation for 20 min at 4500 rpm and the cell pellet was resuspended in 30-50 ml lysis buffer (Table 5), placed two times into the cell disrupter at 1.4 mPa and subsequently centrifuged for 1 h at 45000 rpm. The supernatant containing the proteins of interest was gradually concentrated further with a 10 kDa (Amicon Ultra) filter.

3.1.2.2 *Purification of Li*R *and Li*S *proteins*

To extract the soluble proteins the filtered supernatant was mixed with the positively charged resin DEAE (Diethylaminoethyl cellulose) for ion exchange chromatography. The ratio of DEAE:cell-lysate was approximatly 1:1. The 50 ml Falcon tube containing the supernatant with DEAE was incubated rotating over night at 4° C to ensure the complete mixture of both components and for a sufficient protein binding to increase the yield. After 24 h the mixture was loaded on an empty plastic column and the proteins were eluted at room temperature by use of a step gradient with ice-cold buffers. The concentration of NaCl was increased stepwise by 50 mM in the elution buffer (0, 50, 100, 150, - , 750 mM NaCl). The eluted fractions were loaded onto a 15 % SDS gel and the fraction containing the highest yield of *Li*R and *Li*S proteins (fraction with 350 mM NaCl) was desalted (Zeba Spin Desalting Columns) and concentrated with a 10 kDa filter. The second purification step with anion exchange media DEAE was performed with the desalted fraction having eluted with 350 mM NaCl. The second purification was conducted in the same way performing a step gradient of NaCl. After the second purification the fraction containing a high yield of *Li*RS and only a little amount of contaminating proteins was determined by performing a SDS-PAGE. The corresponding fraction was selected and concentrated by ultracentrifugation using a 10 kDa MWCO filter. The concentrated sample was subsequently applied to a Superdex G200 column with a bed volume of 24 ml to perform size exclusion chromatography (SEC) using an Aekta Explorer System (Pharmacle Biotech). Fractions eluting with a retention volume of 8 ml were pooled, proteins were visualized with SDS-PAGE and determined to be *Li*R and *Li*S. After concentrating the corresponding fraction with a 10 kDa filter at 4200 rpm, it was loaded onto a Superdex G75 column connected to the Aekta system performing another SEC. The proteins were eluted at 4° C with a retention volume of 0.5 ml. For electron microscopy studies 3 µl of the sample were placed onto a carbon-coated grid immediately after the elution. Several grids were prepared and negatively stained (3.3.1.1). To confirm that the fractions contained only *Li*RS complexes the sample was loaded onto a SDS-PAGE and additionally a

western blot was conducted for immuno detection of *Li*R via specific antibody binding to ensure the expression of the target proteins.

3.1.2.3 *Cloning, expression of Li*T

The *Listeria innocua* protein CAC96122.1 (further *Li*T), the homolog to the *Bs*RsbT was cloned from the transfer vector pUC57 (pUC57/*Li*T delivered from GenScrpit) into the pGEX-6P-2 vector (GE Healthcare), using *Bam*HI and *Not*I restriction sites to produce a construct with a GST-tagged fusion protein. GST (Glutathione *S*-Transferase) is a 26 kDa highly soluble protein and attached to the N-terminus of the recombinant protein.

Table 10 Restriction setup

Insert	Vector
I. Restriction	
30 µl pUC57/*Li*T (6.6 µg)	22 µl pGEX-6P-2 (3.3 µg)
6 µl buffer B (SuRE/Cut, 10x)	6 µl buffer B (SuRE/Cut, 10x)
3 µl *Bam*HI (Fermentas)	3 µl *Bam*HI (Fermentas)
1 µl BSA (BioLabs)	1 µl BSA (BioLabs)
10 µl H_2O_{dd}	12 µl H_2O_{dd}
II. Restriction	
30 µl pUC57/*Li*T (6.6 µg)	22 µl pGEX-6P-2 (3.3 µg)
6 µl buffer B (SuRE/Cut, 10x)	6 µl buffer B (SuRE/Cut, 10x)
3 µl *Not*I (Fermentas)	3 µl *Not*I (Fermentas)
1 µl BSA (BioLabs)	1 µl BSA (BioLabs)
10 µl H_2O_{dd}	12 µl H_2O_{dd}

The cleavages were performed separately. The first restriction was executed using *Bam*HI and the second one using *Not*I (Table 10), both for 2h at 37° C. Between the restriction steps a purification with PCR Purification Kit (Qiagen) was performed. After the cleavage the insert was separated from the vector by an agarose gel electrophoresis and afterwards the *rsbT* gene was extracted applying a QIAquick Gel Extraction Kit (Qiagen).

For the ligation 20 µl *Li*T gene and 5 µl linearized vector pGEX-6P-2 were incubated in 3 µl ligase buffer with 3 µl T4 ligase for 2 h at 37° C. The ligated plasmid was transformed in BL21 cells and after detecting single colonies on LB plates, 20 ml cultures were prepared in LB medium with 0.5 % carbenicillin as selection for the insertion of the plasmid with *li*T.

Table 11 Test restriction

pGEX-6P-2/*Li*T (restriction sites BamHI)
20 µl purified plasmid (pGEX-6P-2/*Li*T)
5 µl Puffer B (SuRE/Cut, 10x)
1 µl BSA (BioLabs)
2 µl *Bam*HI enzyme (BioLabs)
2 µl *Not*I enzyme (Fermentas)
19 µl H_2O_{dd}

For the purification of the plasmid with the gene of interest from the cells a QIAprep Spin Miniprep Kit was applied and the eluate was loaded on a 1.2 % agarose gel to verify the size of the vector. The yield of plasmid was determined via absorption measurement with NanoDrop™ device (Thermo Scientific).

For the protein expression BL21 cells were used and after transforming the plasmid into competent cells single colonies from LB plates were grown over night at 37° C.

The expression was performed similar to the *Li*R and *Li*S proteins. Single colonies were transferred into 10 ml LB with a concentration of 1 mM carbenicillin and rotated over night with 250 rpm at 37° C. For the expression every pre-culture was decanted in 1 l LB medium with 1 mM carbenicillin and the cells were grown at 120 rpm and 37° C until 0.6 absorbance at 600 nm. By adding ITPG with a final concentration of 0.1 mM the induction was started and after 3 h the cells were harvested by centrifugation for 25 min at 4500 rpm. The cells were resuspended in lysis buffer transferred into the cell disrupter at 1.4 mPa and afterwards centrifuged for 1 h at 45000 rpm for separation of the cell components from the soluble fraction.

3.1.2.4 *Purification of Li*T

Prior to the purification, the supernatant containing *Li*T was filtered. 1 ml of the filtered sample was loaded onto a 1 ml GSTrap 4B affinity column (GE Healthcare) linked to the Aekta system of GST tagged proteins. If required, up to 4 or 5 GSTrap columns could be connected in series to increase the yield of *Li*T. After washing the columns with 10 column volumes of binding buffer the elution buffer was applied to elute the GST-*Li*T proteins in 0.5 ml fractions. The fractions containing the GST tagged *Li*T were pooled, analyzed by SDS-PAGE and concentrated with a 10 kDa Amicon Ultra filter. For the cleavage of GST from the recombinant protein, 1 unit PreScission™ Protease per 100 µl *Li*T protein (GE Haelthcare) was added and incubated over night at 4° C. The size exclusion chromatography was performed the next day by loading the sample on the Aekta coupled Superdex G75 column. Fractions containing only *Li*T were unified and to verify the purity the pooled fractions were visualized with a 15 % SDS gel.

3.1.2.5 *Forming stressosome complexes*

The three *L. innocua* proteins (*Li*RS, *Li*T) were mixed after purification for 2 h at 4° C and further purified by size exclusion chromatography utilizing a Sephacryl S-500

HR (GE Healthcare) column with a bed volume of 60 ml. To confirm that the RST proteins are able to self-assemble, a SDS-PAGE was performed by loading the fractions eluted after 60 ml which corresponds to a molecular size of around 2 MDa in the elution profile. Negative stained samples were prepared for electron microscopy as described in 3.3.1.1.

3.1.2.6 *In vivo detection of LiR*

To obtain a glycerol stock of the *Listeria innocua* bacteria strain (Table 2) the liquefied cells were plated on BHI agar. Over night cultures at 30° C were prepared by transferring several single colonies from the previously produced LB plates into 50 ml Brain Heart Broth media. Subsequently the pre-cultures were added to 2 l Brain Heart Broth and cells were grown at 100 rpm and 37° C. After 24 h they were harvested by centrifugation at 4200 rpm for 30 min and resuspended in 100 mM Tris buffer with 10 % glycerol and frozen in liquid nitrogen at -80° C.

3.2 Expression and purification of *Vibrio vulnificus* stressosome proteins

The *Vibrio vulnificus* stressosomes were kindly provided by Wenke Reiss from the group of Jan Pané-Farré, University of Greifswald in collaboration with the group of Rick Lewis, Newcastle University.

3.3 Electron microscopy

3.3.1 EM - *Listeria innocua*

3.3.1.1 *Sample preparation for negative stain*

For the first screening negative stained *Li*RS complexes were prepared by loading 3 µl purified protein sample onto a glow-discharged carbon-coated grid (400 mesh, SPI Supplies / Structure Probe, Inc). After incubation for 30 sec, they were stained with 1 % uranyl acetate or 5 % ammonium molybdate solution.

3.3.1.2 *Structural investigations of Li*RS *complexes by single particle EM*

A small set of micrographs from the negative stained *Li*RS proteins was collected on a Philips CM120 electron microscope at 120 kV with a 2k x 2k CCD camera for preliminary analysis using a magnification of 45,000x at a defocus range of 2.5 – 3.5 µm. 6100 particles were picked with the EMAN program Boxer (Ludtke et al., 1999) and further processed with IMAGIC (van Heel, 1981). To improve the image quality the single projections were pre-processed: first, by band-pass filtering followed by centering and masking to define the area of interest (IMAGIC handbook, Image Science Software GmbH, Berlin, Version May 2006). Afterwards statistical analysis of the image set (MSA classification) was done to sort the images into groups with common orientations.

3.3.2 EM - *Vibrio vulnificus*

3.3.2.1 *Sample preparation for cryo-EM*

To prepare vitrified samples of the oxidized *Vv*RS stressosomes, 3 µl aliquots with a concentration of 0.3 mg/ml were applied onto glow-discharged Quantifoil holey carbon grids (Quantifoil Micro Tools, Jena, Germany). The grids were blotted for 2-2.5 sec at 10° C and 70 % humidity, were immediately plunge-frozen in liquid ethane using an FEI Vitrobot and afterwards transferred into liquid nitrogen.

3.3.2.2 *Data collection for single particle analysis*

Two data sets which differ in the recording approach were collected from the oxidized *V. vulnificus* stressosome. The first set (Set 1) was collected on film and the second (Set 2) with a direct electron detector, Falcon II camera.

Data collection for the Set 1 was implemented on the FEI Tecnai Polara electron microscope operating at 200 kV with a magnification of 59,000x recording on Kodak SO-163 film. The dose was 10-15 $e^-/Å^2$ and the defocus range between 2.5-3 µm. The obtained negatives were developed for 12 min in full-strength D-19 developer and fixed for 8 min in Kodak Rapid Fix, afterwards scanned with a Zeiss Photoscan scanner (Intergraph) with a pixel size of 7 µm, resulting in a pixel size of the sample of 1.14 Å.

For Set 2 the data was also collected with a FEI Tecnai Polara but the operating voltage was set to 300 kV and a back-thinned FEI Falcon II detector was used. The camera system was configured to collect 18 subframes/sec with an exposure time of 1.5 sec resulting in 24 subframes per micrograph. The electron dose was 3 $e^-/Å^2$ per subframe and the defocus range for the recorded data set was between 1.7 – 5.5 µm. The magnification was set to 59000x and the pixel size of the sample was 1.77 Å.

3.3.2.3 *Image processing of cryo-data*

The image size is camera-dependent, hence different amounts of particles were boxed for each set manually. On micrographs from the Falcon II camera 20 up to 60 single complexes were obtained and in contrast about 100 complexes from digitalized film. Set 1 finally contained 31300 particles from 292 micrographs and Set 2 amounted to 66200 particles of the *Vv*RS complex from 1600 micrographs.

The new direct detectors provide innovative applications for modifying the quality of the cryo-EM micrographs (for comparison chapter 1.1). For Set 2, consisting of stacks of images, motion correction was performed by subframe alignment of one stack (Li et al., 2013) (the software for motion correction is available on http://www.nature.com/nmeth/journal/v10/n6/full/nmeth.2472.html#supplementary-information). Furthermore the first subframe containing the most drift was removed from the stack. The remaining subframes were summed to a new drift-corrected image that was used for the 3D map reconstruction.

Of every image the contrast transfer function (CTF) was determined by CTFFIND3 (Mindell and Grigorieff, 2003) either using the program EMAN2 for Set 1 or with CTFFIND3 within the RELION workflow concerning Set 2. For the second data set CTF was subsequently rechecked in EMAN2 to verify the correction for certain images. Micrographs with perfect fitted oscillations of the CTF and without any drift or astigmatism were selected for further reconstruction processes. The reconstructions were performed with EMAN2, Set1, (Tang et al., 2007) and RELION, Set 2, (Scheres, 2012). The reconstruction process is described in detail in the result part.

4. RESULTS

4.1 *L. innocua* stressosome proteins

4.1.1 Protein purification of *Li*R and *Li*S

*Li*R and *Li*S could be separated from the cell lysate by two subsequent cation chromatography (DEAE) runs and size exclusion chromatography in order to minimize the amount of contaminations (Figure 10). It was essential to perform the washing by a step gradient starting with 50 -200 mM NaCl. *Li*R and *Li*S were eluted at around 350 mM NaCl.

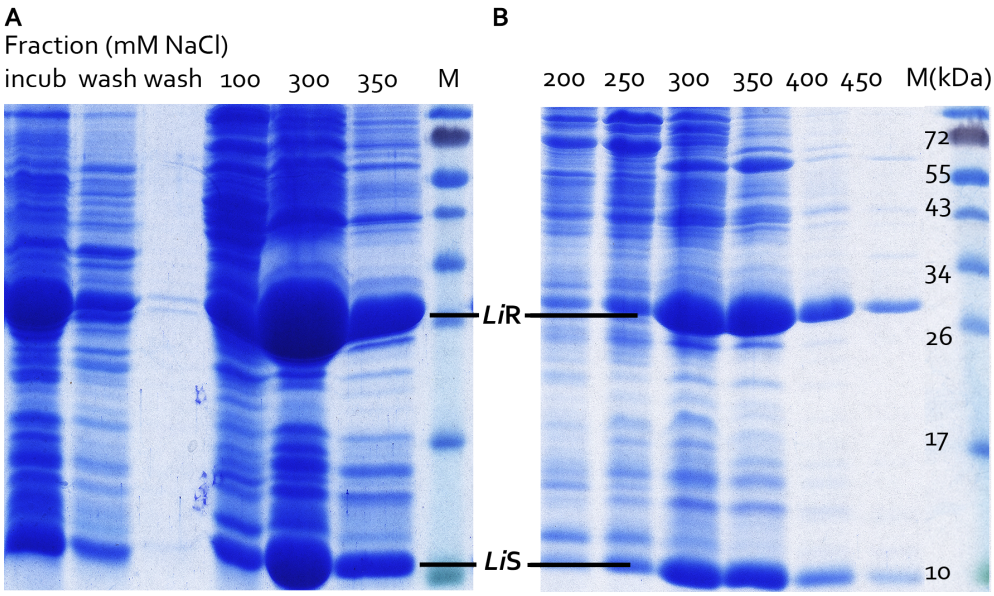

Figure 10 DEAE purification of *Li*R and *Li*S

A: First ion exchange chromatography. Incub: over night incubation of cell lysate with DEAE, wash: wash steps before elution. Fraction 350 mM NaCl was selected for further DEAE purification, represented in **B**.

B: Second ion exchange chromatography. *Li*R and *Li*S migrate at levels of lower molecular weights. Fraction eluted at 350 mM NaCl contains less contamination compared to the previous purification.

*Li*R and *Li*S appeared around 30 kDa and 11 kDa (Figure 10A, lane 300 mM NaCl) which was validated after the second DEAE purification by sequencing of the protein bands (Zentrum für Molekulare Medizin, Zentrale Bioanalytik, Robert-Koch-Str. 21, 50931 Köln). The results confirmed the expression of *Li*R and *Li*S, clearly observable on the SDS gel (Figure 10) and revealed a molecular weight for *Li*R of approximately 32 kDa and for *Li*S of approximately 13 kDa, respectively.

After desalting, size exclusion chromatography was conducted using the Superdex G200. It was assumed that the *Li*RS stressosome proteins self-assemble to complexes as the *Bs*RsbRS proteins. Therefore a size exclusion column with a higher separation range for molecular weights between 10000 and 600000 Da was chosen to separate the *Li*RS complex from the soluble part (Figure 11 A). Some contaminations were still observable but both protein bands appeared dominantly on the SDS-gel (Figure 11A, lane 7-9).

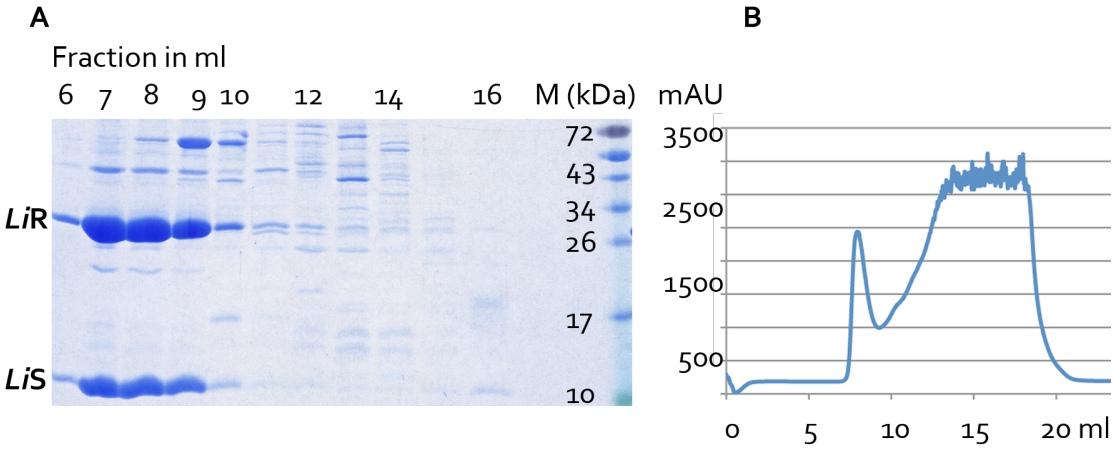

Figure 11 Purification of *Li*R and *Li*S with Superdex G200

A: The lanes 7-9 ml contain *Li*R and *Li*S, some small contaminations are detectable.

B: *Li*RS complexes were eluted in the void volume.

Due to the remaining residual contaminations an additional size exclusion chromatography was performed with a Superdex 75 (Figure 13). Afterwards only

two bands were visible on the SDS gel representing the high purity of the sample with a ratio of approximately 2:1 for *Li*R:*Li*S.

In addition, a thin band appeared above the monomeric *Li*R band (Figure 13A, lane 10). A polyclonal anti-*LiR* antibody (GenScript) verified the upper band as *Li*R dimers, shown in the western blot in Figure 13.

MYKDFANFIRTNKKDLLNNWMNEMEKQSDPLINDIAKEPMYEETSIEFVDLIVSNITENGSKFNEKLDDFAEKVV
HLGWPIHFVTTGLRVFGLLVYTAMRDEDLFLKREEKPEDDAYYRFETWLSSMYNKVVTAYADTEKTVSIQKSAL
QELSAPLLPIFEKISVMPLIGTIDTERAKLIIENLLIGVVKNRSEVVLIDITGVPVVDTMVAHHIIQASEAVRLVGCQA
MLVGIRPEIAQTIVNLGIELDQIITTNTMKKGMERALALTNREIVEKEG

Figure 12 Protein sequence of *Li*R

The N-terminal sequence for anti-*Li*R is marked in red.

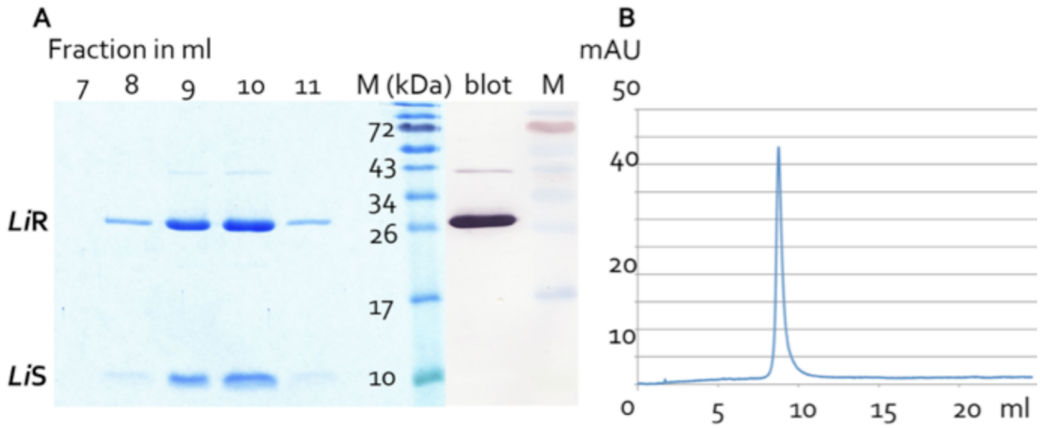

Figure 13 Purification of *Li*R and *Li*S with Superdex G75

A: SDS gel shows two protein bands belonging to *Li*S at 10 kDa and *Li*R at around 30 kDa. A higher third band appears at 43 kDa, visible in lane 9 and 10 ml. Western blot (blot) identified this band as *Li*R dimer.

B: The elution profile of Superdex G75 confirms the formation of the *Li*RS complex. A single peak appeared in the void volume.

4.1.2 Cloning of *LiT*

The fragments obtained after the restriction of pUC57/*li*T were separated by agarose gel electrophoresis as shown in Figure 14A. After ligation of the expression vector pGEX-6P-2 with the insert *liT* a transformation was conducted and all tested colonies contained a 400 bp insert (Figure 14B). Sequence analysis (SRD, Scientific Research and Development GmbH, Bad Homburg) of the purified insert resulted in identical sequences for the insert and *li*T.

After purification of *li*T from the agarose gel the concentration of *Li*T in 50 µl HH_{add} was measured with NanoDrop yielding around 100 ng/µl.

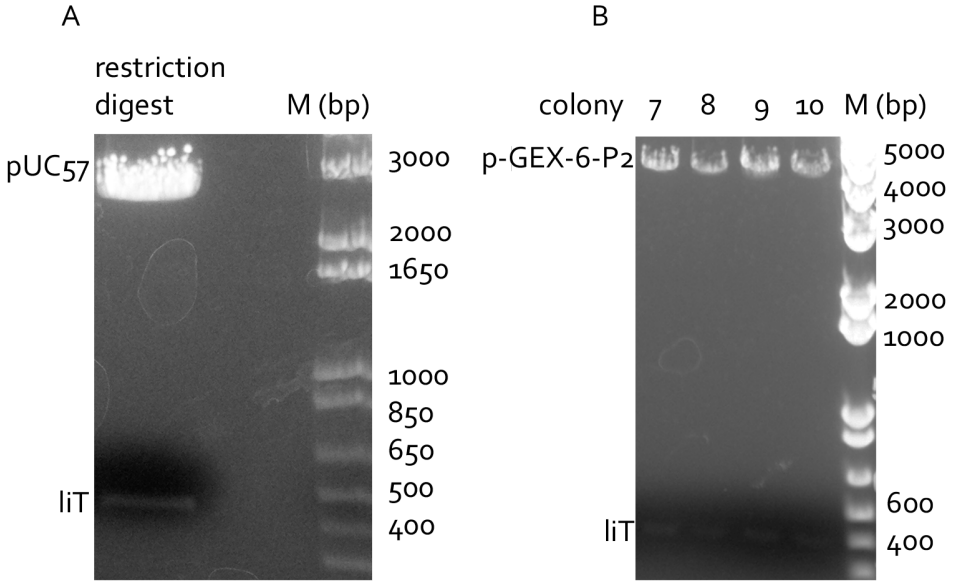

Figure 14 Cloning of *liR*

A: After digestion of pUC57/*li*T two gene bands appeared at different molecular-weight sizes. The band at 400 bp represents *li*T hile that at 2800 bp represents the transfer vector pUC57. The insert of A was ligated into the expression vector pGEX-6P-2.

B: Analytical restriction of the final plasmid pGEX-6P-2/*li*T, all digested plasmids inserted *li*T.

4.1.3 Protein purification of *Li*T

The purification of the GST-tagged protein *Li*T (15 kDa) out of the cell lysate is shown on the SDS gel in Figure 15.

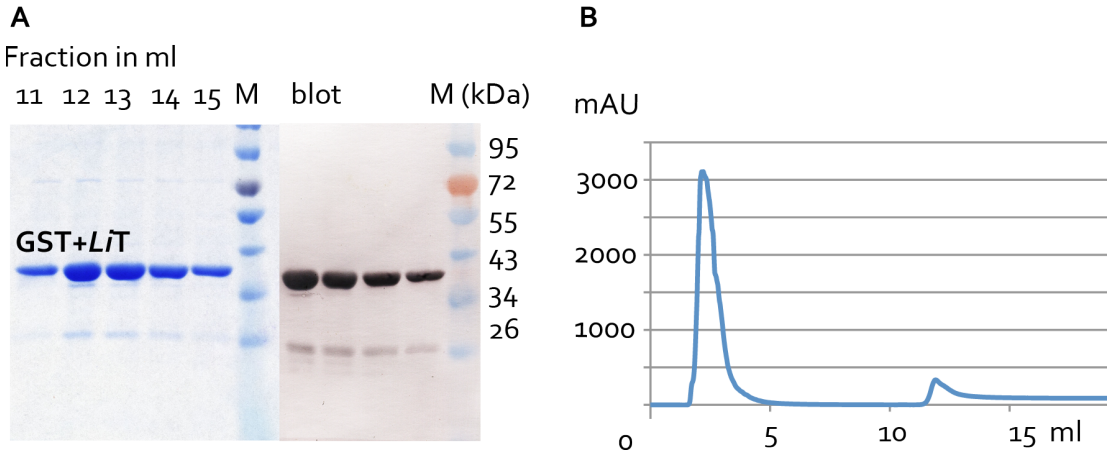

Figure 15 GST fusion protein purification

A: SDS gel of the elution fractions of the GSTrap affinity column (left) and western blot containing the GST-tagged fusion protein (right).

B: The first peak of the elution profile contains the cell lysate (2-4 ml). After washing steps (5-10 ml) the GST-tagged fusion protein was detected at 11-15 ml and visualized at a SDS gel (**A**) at a molecular weight of around 40 kDa.

Both proteins were linked in a complex and appeared as a single band at a molecular weight of around 40 kDa, visible on the SDS gel s well as the western blot (Figure 15A). The smaller band at 26 kDa in the gel and the blot is referable to the unbound GST protein. The cleavage of the GST protein from the *Li*T protein is visualized in Figure 16 A. Sequence analysis of the purified protein performed by ZMMK confirmed (sequence identity of 90 %) the identity of the *Listeria innocua* protein CAC96122.1 (*Li*T). The expression and purification of *Li*T could therefore be established.

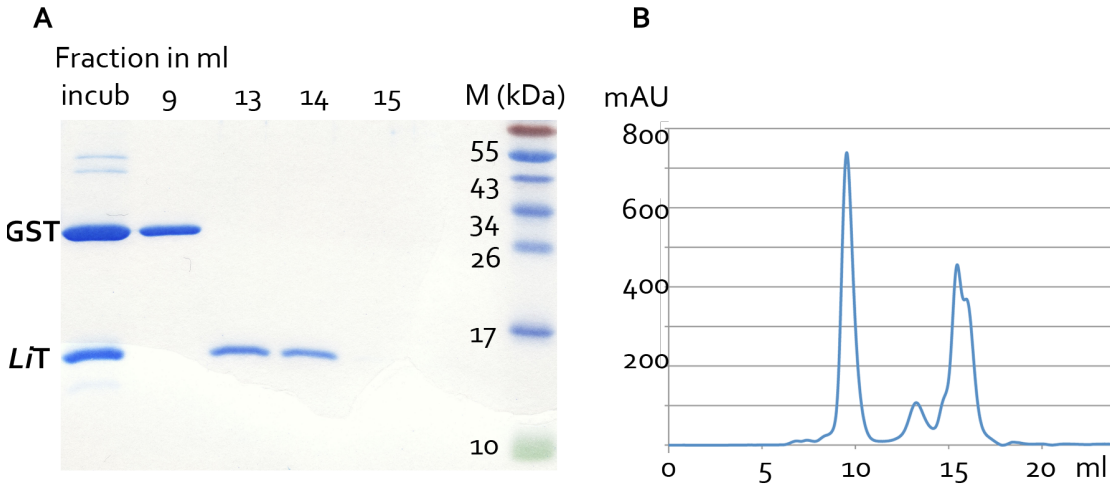

Figure 16 Size exclusion chromatography of the cleavage of GST and *Li*T

A: SDS gel of the cleavage. Incub shows the approach before and lane 9 – 15 ml after the size exclusion chromatography. GST and *Li*T were separated. Lane 9 ml contains GST and lanes 13-14 *Li*T. No contaminations are present in the *Li*T containing fractions.

B: Size exclusion chromatography profile. First peak contains GST and the second *Li*T. The peak at 16 ml contains DTT (Dithiothreitol), a component of the elution buffer.

4.1.4 Stressosome complex assembly of *Li*RsbRS and *Li*RsbT

After the successful expression of all three stressosome proteins of *Listeria innocua* *Li*R, S and T were mixed and incubated to confirm that the proteins self-assemble to the RST complex. After size exclusion chromatography the pooled fractions between 65 – 80 ml, corresponding to a molecular size of around 1.8 MDa, were concentrated and loaded onto a SDS gel (Figure 17) showing the self-assembly to *Li*RST stressosomes.

In comparison to *Li*R, *Li*S and *Li*T appear less concentrated on the SDS gel, which could be explained by the low molecular weight and quantity within the stressosome. The yield of *Li*T is half as much as that of *Li*S, despite the similar molecular weight and the equal predicted amount of both proteins. The binding efficiency of *Li*T could lower the yield of *Li*RST stressosomes. The wide peak extending over 15 ml within the elution profile (Figure 17) is an indication for incomplete *Li*RST assembly or monomeric *Li*R assemblys.

Fractions eluted at about 80-100 ml contained no proteins or any contaminations, observed within SDS-PAGE.

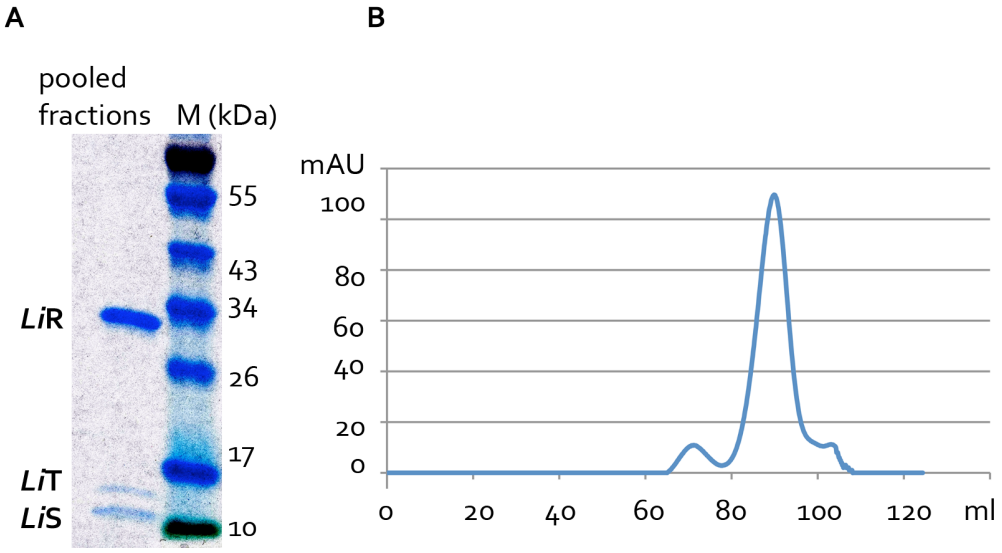

Figure 17 Stressosome formation

A: SDS gel representing all pooled fractions between 65 and 80 ml of the size exclusion chromatography. Three protein bands are visible in one lane representing *Li*R, *Li*S and *Li*T

B: Profile of the size exclusion chromatography.

4.1.5 Electron microscopy of *Listeria innocua* RS and RST complexes

Purified *Listeria innocua* RS and RST complexes (chapter 3.1.2) were further investigated by negative-stain EM in Figure 18. These images provide the first evidence that the *Listeria innocua* genome encodes for RST proteins that self-assemble to stressosome complexes.

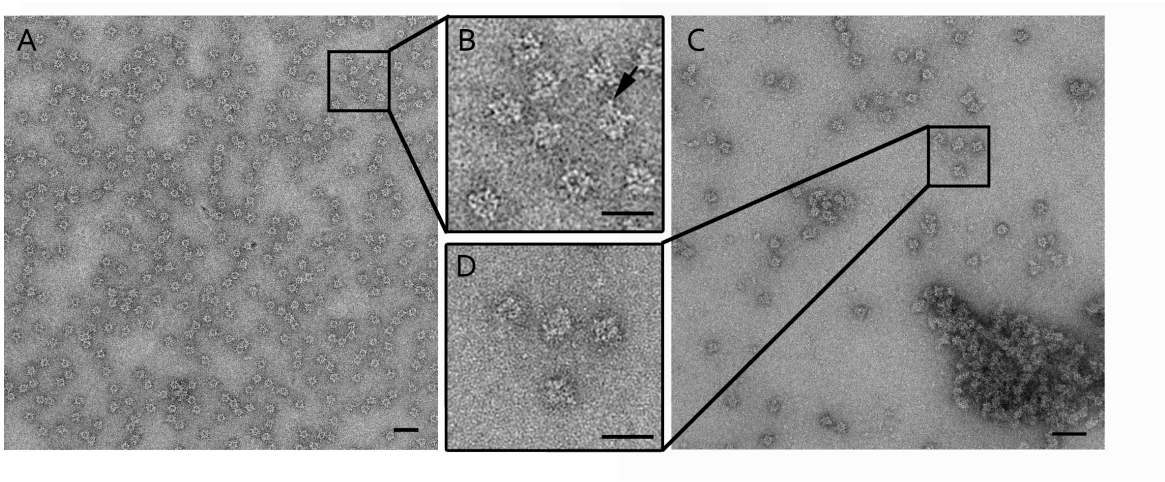

Figure 18 Negative stained micrographs of *Li*RS and *Li*RST stressosomes

A: Micrograph of *Li*RS complexes after purification. Stressosomes appear white. The enlarged cutout of **A** on the right (**B**) shows the N-terminal domains of *Li*R as several smaller dots around the circular core (**arrow**)

C: Micrograph of the *Li*RST negative stained stressosome. Single complexes and some aggregates are present. *Li*RST complexes are shown magnified in **D** with visible N-*Li*R as white dots around the core. Scale bar in **A** and **C** is 50 nm. Samples stained with 1 % uranyl acetate. The applied magnification to collect images was 45,000x. Scale bar in B and D is 300 Å.

The negative stained stressosmes in Figure 18 show a measurable diameter of 20 nm, moreover the N-terminal domains of *Li*R appear as small white points located around the core (Figure 18B, D). The core shows a darker centre, which implies a hollow sphere.

Preliminary structural investigations were performed of negative stained *Li*RS complexes (Figure 19) by single-particle analysis. 6100 particles were boxed from 20

images and the set was imported to IMAGIC for further processing (3.3.1.2). The class sums of the *Li*RS stressosome (Figure 19B, C) represent the round complex and a darker spot in the centre that reveals a hollow STAS domain core. In some classes the N-*Li*R domains are detectable (Figure 19B polygon) within the resolution range expected for a negative stained particle. Further class sums were constructed including the core of the complex only. The fuzzy outer part containing the N-terminal domains, for comparison Figure 19B, was masked out for the class averages of the *Vv*RS core. Specific symmetries of the core class sums are noticeable (Figure 19C arrow).

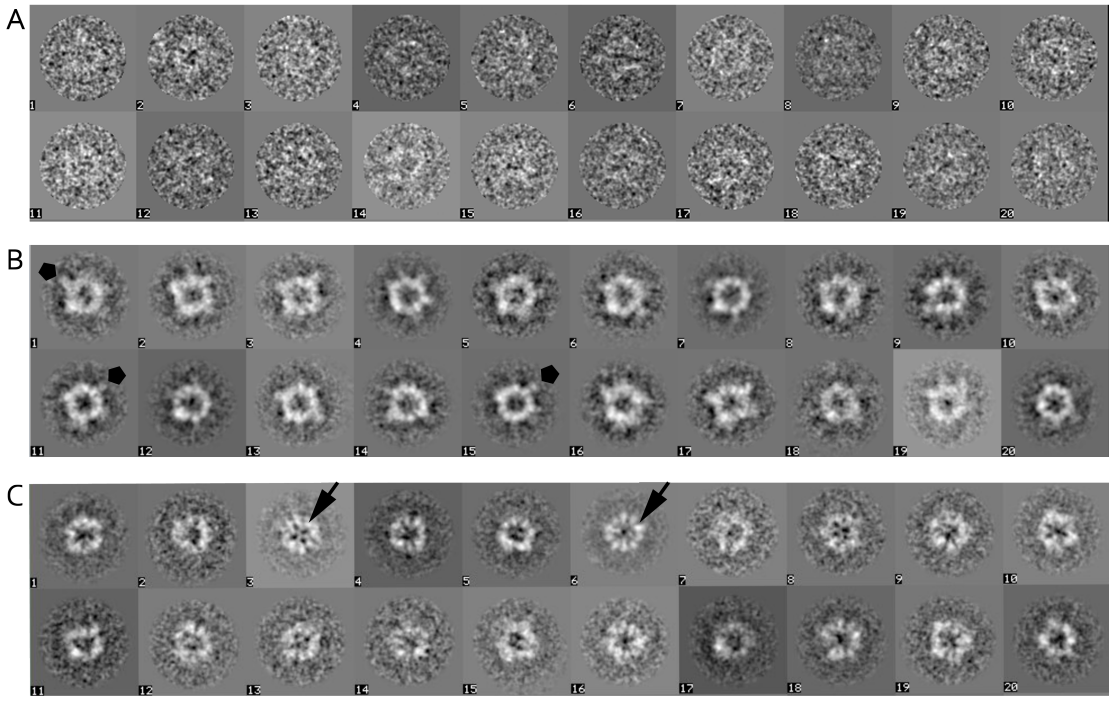

Figure 19 Structural analysis of *Li*RS complex

(**A**) Particles, (**B**) Class sums *Li*RS, (**C**) Class sums *Li*RS-core

A Subset of the original boxed particles, band-pass filtered, centered and masked.

B Class sums of *Li*RS complexes of 6100 particles show round hollow spheres with a fuzzy outer part and at some points the N-terminal domains of *Li*R stick out from the core as brighter domes (polygon).

C: 2-fold and 5-fold symmetry becomes apparent in some classes.

4.2 Single particle analysis of *Vibrio vulnificus* RS complexes

The samples of the *Vv*RS stressosomes were first verified by negative stain (Figure 20) and then prepared for cryo-EM (Figure 21). On the micrograph the sample shows the same overall shape as the *Li*RS stressosome

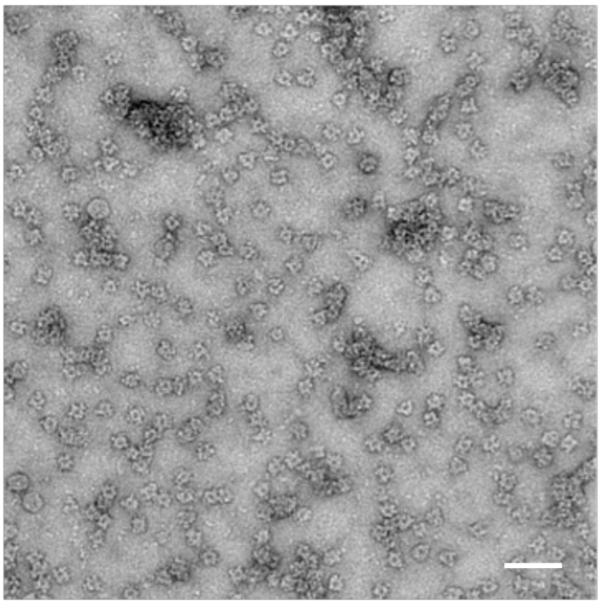

Figure 20 *V. vulnificus RS* stressosome

Negative stained complexes are observable in white. The particles are very concentrated. For the preparation of the cryo samples the sample was diluted in order to avoid particle contact. The complexes appear as round dots with a black middle due to the hollow core while the N-terminal domains of *Vv*R protrude from the center. Stain: uranyl acetae, scale bar 300 Å.

4.2.1 Data processing of Set 1

For the preliminary evaluation of the *Vv*RS cryo-data 14 scanned negatives with 1900 particles were processed. More particles per image could be boxed on film (around 100 single particles) compared to the digital micrographs from the Falcon II (around 60 single particles) (Figure 21A, C). Data class sums were created and are represented in Figure 22.

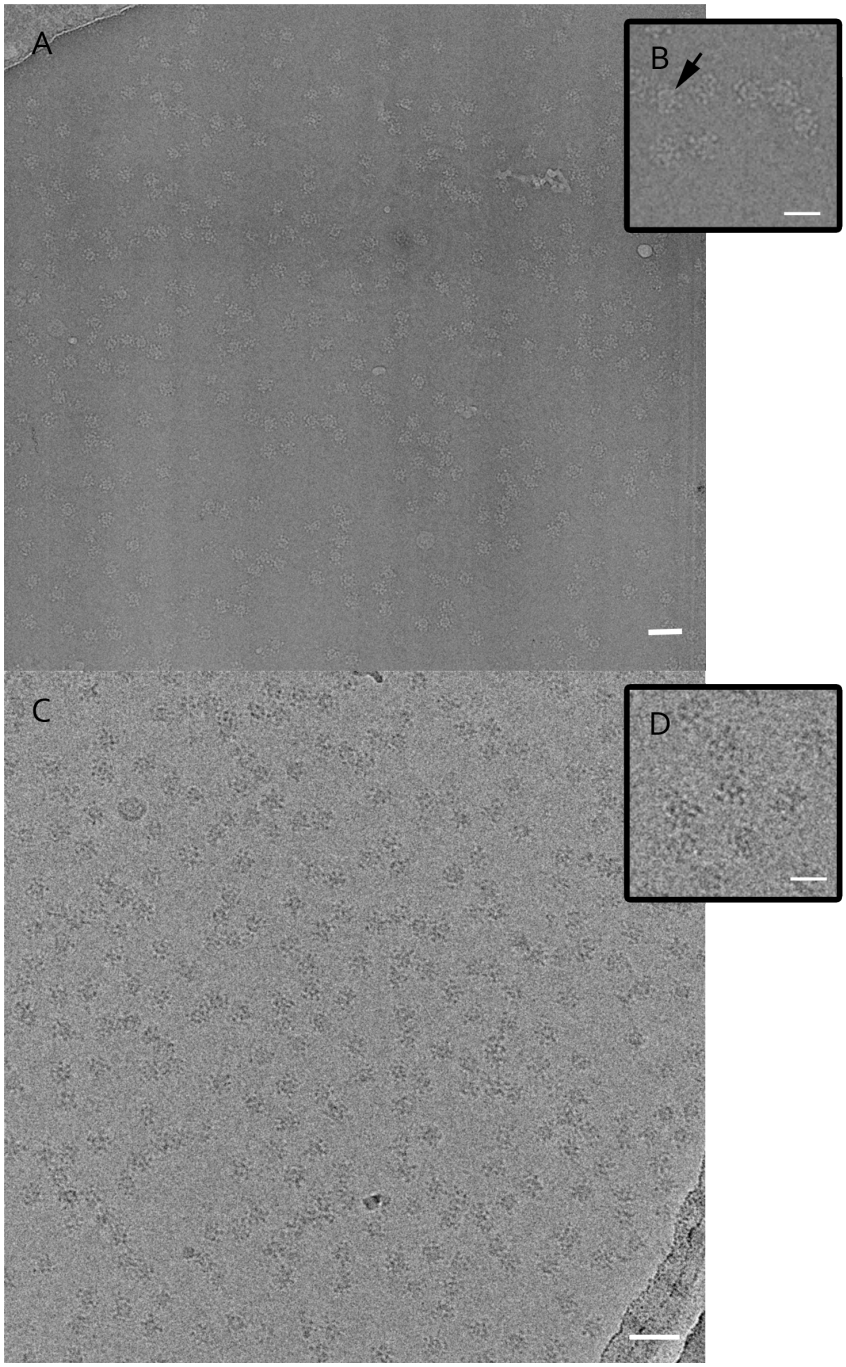

Figure 21 Cryo-micrographs of the *Vibrio vulnificus* RS stressosome

A: Scan of a negative. **C:** Micrograph collected with the Falcon II. Complexes are visible in both images with the round core. Cutouts in **B** and **D** show enlarged stressosomes with the N terminal domains of *Vv*R as small round densities (arrow). **C** and **D** reversed contrast, proteins appear black. Scale bar in **A**, **C** 50 nm, **B**, **D**. 300 Å.

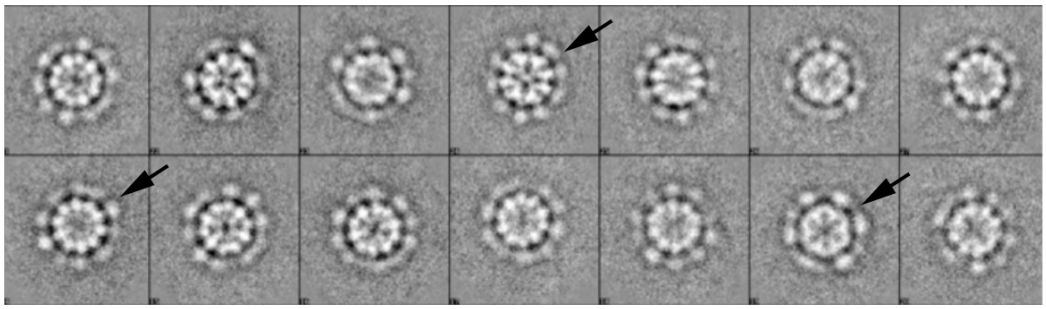

Figure 22 Selection of various class sums

The classes show the core and N-terminal domains of *Vv*R. Different symmetries are perceptible within the inner part (arrows).

The class sums obtained with EMAN2 (Figure 22) show that the N-terminal domains of *Vv*R were not uniformly distributed around the inner part of the stressosome. The core appears denser than the N-terminal domains which are represented in the image as small white dots. Within the core two-, three- and five-fold symmetries could be distinguished (Figure 22 arrows). This class sums are comparable to the class sums of the *Bacillus* stressosome (Maerles-Wright et al., 2008, supporting online material). These promising preliminary results prompted further analysis and more data were collected, first to 14.600 particles for the generation of a reconstruction.

4.2.1.1 *Generating the initial model*

The first cryo-data indicated that the overall structure of the *Vibrio vulnificus* and the *Bacillus subtilis* stressosome is quite similar exhibiting the same D2 point group symmetry with one *Vv*S and two *Vv*R surrounding each 3-fold axis. For the first reconstructions an initial 3D model is necessary, which was obtained with class-averages (Figure 22) in EMAN2 and according to the outer shape of the core icosahedral symmetry was applied. The arrangement of the proteins within the core and the locations of the N-terminal domains were not considered at that point.

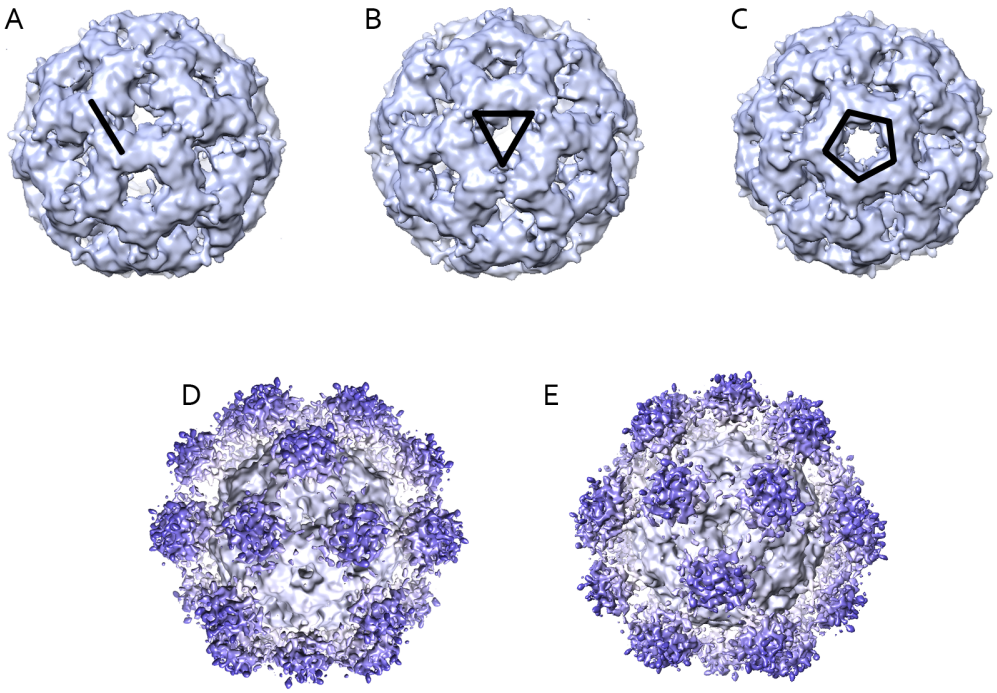

Figure 23 Initial model constructed by applying icosahedral symmetry

A-**C:** Initial model from different views presenting 2-fold (**A**), 3-fold (**B**) and 5-fold (**C**) symmetry which are illustrated via stroke, triangle and pentagon.

D and **E:** 3D Map with all 30 N-terminal domains is pictured in 2 different orientations. On every 2-fold a N-terminal domain is located. Orientation in **A** is the same as in **D** and orientation **B** and **E** correspond as well. Using the data set of 14.600 particles in EMAN2 an initial model could be obtained.

The obtained initial models were very similar, virus-like shaped and without any appendages (Figure 23A-C). Due to the complex D2 symmetry of the stressosome it was necessary to reconstruct the core first accordingly, afterwards continuing to reconstruct the N-terminal domains. One of the five-fold models was chosen as the reference map to start the reconstruction process and to generate a symmetrical correct core as starting point applying icosahedral symmetry. The resulting map consists of an icosahedral core at 12.5 Å with 30 2-fold axes and 5- and 3-fold symmetry (Figure 23D, E) with 30 N-*Vv*R dimers located on each 2-fold axis because of the applied icosahedral symmetry.

For the following reconstruction D2 symmetry was superimposed using a reference map based on the icosahedral initial model. According to the *B. subtilis Bs*RsbRS model 10 additional N-terminal domains were removed using USCF Chimera (Pettersen et al., 2004).

4.2.1.2 *The difficulty of single-particle analysis of the stressosome*

The 3D map of Set 1 (31.300 particles recorded on film) exhibits a resolution of 20 Å with N-terminal domains of varying densities. The challenge during the reconstruction process was the high symmetry leading to misalignments. N-terminals domains of *Vv*R are not equally distributed around the core. Two N-terminal domains are located at each 3-fold axis, respectively (detailed symmetry description in 4.2.1.4). Overlapping densities increased significantly in the projections (Figure 24B and C) whereas N-terminal domains with weaker densities could not be aligned by the program and were averaged out in the second refinement iteration (Figure 24B and C). The class sum in Figure 24A shows *Vv*R N-terminal domains of varying densities. The core reveals a much denser structure compared to the flexible N-terminal domains.

Consequently it was necessary to find the right conditions for the reconstruction which exclude misalignments and result in a 3D map, which includes the D2 symmetry axis.

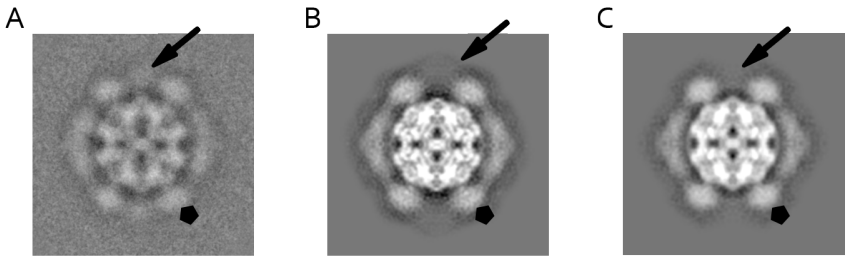

Figure 24 Densities in class sums, projection of round 1 and projection of round 2

A: A particle class and the corresponding projection classes after **B:** the first and **C:** second reconstruction round. The arrows indicate a weak density of a backward located N-terminal domain that is not visible after the second refinement iteration (**C**). The N-terminal domains which are located in front and overlap are detectable as bright spots (polygon).

4.2.1.3 *Reconstruction of VvRS stressosome with data collected on film*

The eigenimages and class sums of the single projections in Figure 25 illustrate a combination of different symmetries within the *Vv*RS stressosome. Eigenimages indicate the main symmetry elements of the data and hence, are useful to determine the symmetry of a protein (van Heel, 1989). The images of the *Vv*RS complex in Figure 25A show 2- ,3- and 5-fold symmetries. In image 3 and 5 of the eigenimages the irregular ordering of the N-terminal domains is noticeable and additionally the projections show the irregular pattern of the distribution of the *Vv*R N-terminal domains around the core as well. The correspondence of the class averages with the re-projections from the reconstructed map confirms that the final map displayed in Figure 25 is correct.

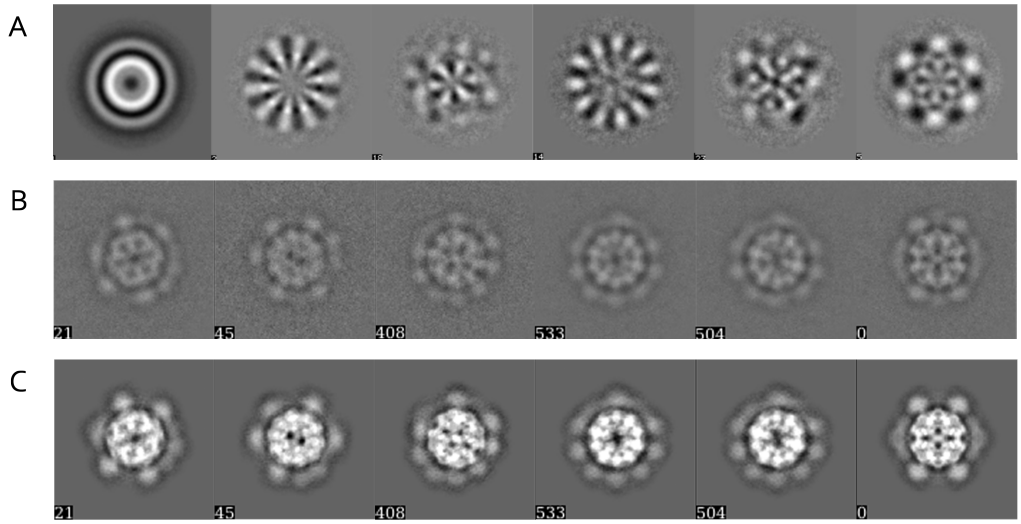

Figure 25 Image analysis of the *Vv*RS stressosomes

A: Subset of some eigenimages show different symmetries within the complex. **B:** class averages and **C:** corresponding re-projections of the 3D map. Various symmetries are within the classes and re-projections detectable 3-fold, 2-fold, 5-fold and mirror symmetry (from left to right).

The reconstruction reveals a 3D structure at a resolution of 19.5 Å (Figure 26). The stressosome comprises 20 *Vv*R N-terminal dimers that point away from the core. We were able to adjust the reconstruction settings in a way, that all N-terminal

domains nearly have the same density. The connecting helixes between the C- and N-terminal domains of *Vv*R-dimers could be obtained at some positions but were not resolved for every dimer at this resolution.

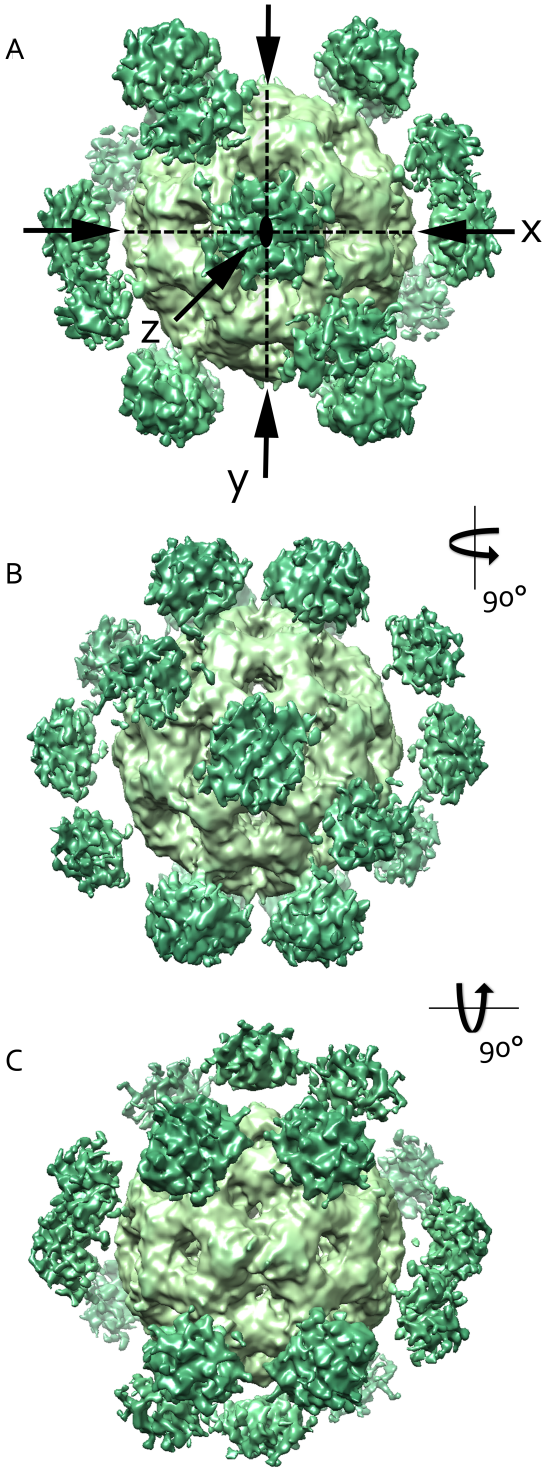

Figure 26 Single particle reconstruction of *Vv*RS stressosome.

The final map with a resolution of 19.5 Å is presented at the three different D2 symmetry axes (**A**-**C**). The *Vv*R N-terminal domains are illustrated in a darker shade of green than the *Vv*RS core.

A: 3D map positioned at the axis that was used for the reconstruction in EMAN2. Some N-*Vv*R dimers appear denser. The 2-fold axes x and y are indicated with arrows and broken lines, the third axis z as a dot in the middle due to the frontal view. All three axes are perpendicular to each other and meet in one center rotation point within the core.

B: Map is turned by 90° and visible from the y-axis.

C: Map is turned again by 90° and visible from the z-axis. One *Vv*S dimer is located in every 3-fold of the core resulting in two N-*Vv*R free bands around the core with five *Vv*S dimers in every band. The down view represents a *Vv*S dimer.

A major challenge for the reconstruction program was that the N-terminal domains exhibited weaker densities compared to the compact core (Figure 24, Figure 25) leading to misalignments. This resulted in the map in weak and strong N-*Vv*R densities, in missing or half sized N-terminal domains. Secondary structures could not be obtained at this resolution. The detailed arrangement of the subunits is summarized and pictured in the following chapter.

4.2.1.4 *Symmetry and subunit arrangement of the stressosome*

The stressosome has a D2 point-group symmetry with a pseudo-icosahedral STAS domain core. The three symmetry axes are perpendicular to each other running through a centre rotation point (Figure 26). In Figure 27 the arrangement of the stressosome proteins *Vv*R and *Vv*S is illustrated as a plane 2D map. Typical for an icosahedron is the presence of 30 2-fold edges that are observable for the stressosome core. Only on 20 edges *Vv*R dimers are located (black oval) leading to the D2 symmetry whereas *Vv*S dimers (red oval) are positioned on the other 10 edges.

The core shows 5-fold and 3-fold symmetry axes, pictured as a pentagon (5-fold) and triangle (3-fold). These are arranged alternating in an s-shaped manner resulting in two s-bands that form the core (grey and blue: first s-band, green and purple: second s-band). Within the bands two of the 3-folds are lying together as dimers front-faced and in every band five 3-fold dimers are observable. Every triangle dimer connection of the 3-fold possess 2 *Vv*S proteins and results in the *Vv*S dimer (red oval). This arrangement leads to the N-*Vv*R free bands (Figure 27B). In parts of the upper map some grey shaded planes are marked in between the shapes. They indicate the connection edges that are closed in the 3D map but open in the plane.

In 8 of the 12 5-folds present three *Vv*R proteins are positioned together with two *Vv*S and the 4 of the pentagons hold 4 *Vv*R proteins, visible in the top and middle of the diagrams. The *Vv*R dimers are generated by *Vv*R monomers from two adjacent pentagons only (Figure 27B black oval). In this diagram 10 of the 20 *Vv*R dimers are indicated (black oval). In the middle of the map two differently colored pentagons are located tip on tip perpendicular to each other (Figure 27A grey arrow) and this point of view is comparable to the orientation of the map in Figure 26B. The triangle-dimers located below and above the tip on tip pentagons are represented in view Figure 26C.

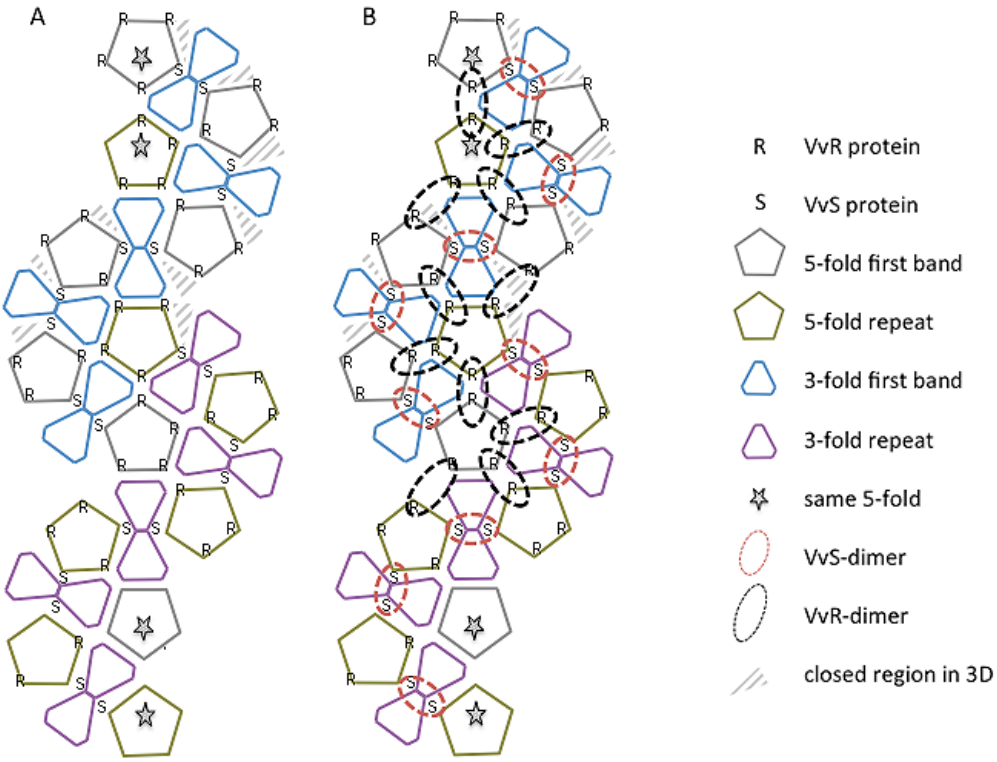

Figure 27 Symmetry of the stressosome and arrangement of the subunits represented in a 2D map

A: Symmetry arrangement of the stressosome. All *Vv*R and *Vv*S proteins are pictured within the 2D map. Labels of the symbols are explained in the legend on the right. The 4 pentagons with the arrows mark the 2 repeated five-folds lying on the back, the pentagon dimers are pictured twice here in the 2D map for better representation.

B: Additionally the *Vv*S dimers (in red oval) and the *Vv*R dimers (black ovals) are marked.

4.2.2 Data processing of Set 2

The image processing for the data set collected with the Falcon II direct electron detector (Set 2) was conducted as described in chapter 3.3.2.3. The first class sums (Figure 28) show 2-, 3- and 5-fold symmetry elements comparable to the class sums of Set 1 (Figure 22) and the N-*Vv*R proteins are detectable as white spots around the core. Within the black ring surrounding the bright core some connecting helices between the C- and N-terminal domains of *Vv*R are detectable (Figure 25, Figure 28 arrow). Due to the front position or overlay of several N-*Vv*R in one complex some N-terminal domains appear brighter compared to all present N-*Vv*R (Figure 28, frame 1).

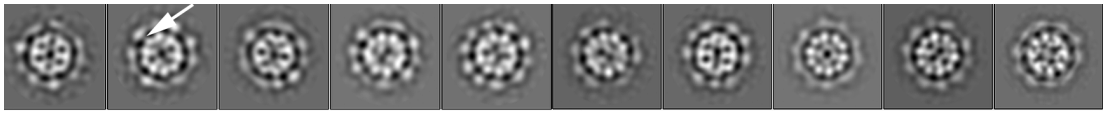

Figure 28 Selection of class sums Set2

White arrow indicates a visible linker helices between C- and N-terminal *Vv*R. In the first frame the brighter N-terminal domains are noticeable.

4.2.2.1 *Reconstruction process*

CTF correction was performed within the RELION workflow. The Thon rings and CTF amplitudes from a typical electron micrograph collected with the Falcon II are presented in Figure 29.

The 3D map received from Set 1 was chosen as initial reference, rescaled to the new pixel size of 1.77 Å and used to refine the first part of Set 2. Comparably to Set 1 the first reconstruction was done with imposed icosahedral symmetry to achieve an optimal resolution for the core. The arrangement of the N-*Vv*R was not considered t first. A similar map to Figure 23 was obtained with 30 N-terminal domains of *Vv*R on the icosahedral 2-folds. Afterwards the N-terminal domains were reduced manually in Chimera as described before and the reconstruction process was repeated applying D2 symmetry.

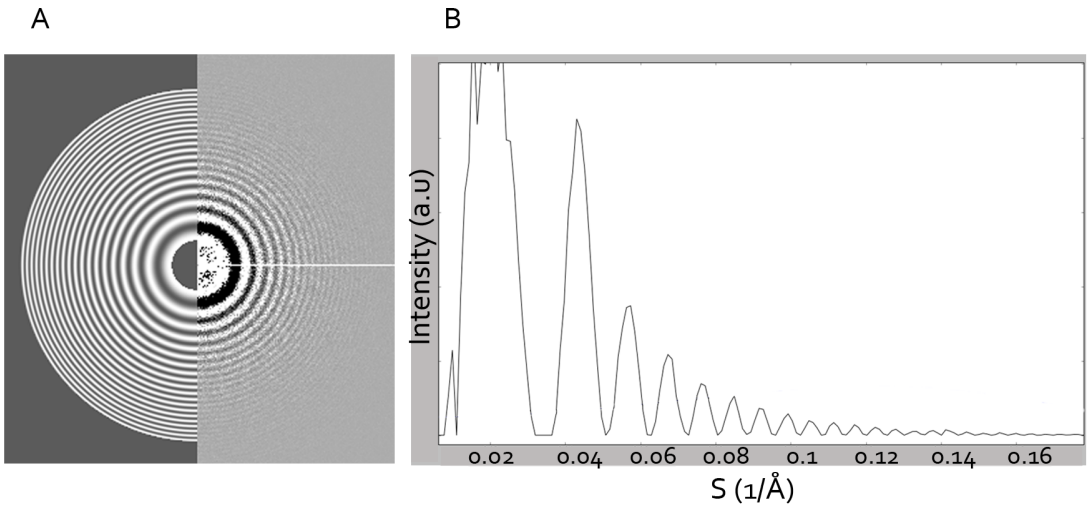

Figure 29 CTF correction

A: Thon rings **B** CTF. CTF correction of a frame composed of 23 subframes after drift correction and removal of the first subframe.

During the reconstruction process the previously reconstructed map was implemented as reference for the next refinement. Subsequent refinements were carried out, first with icosahedral symmetry and then finally applying D2.

In the resulting maps unequal density distribution between the N-terminal domains could be observed during all refinement steps. As the N-*Vv*R domains are identical and always formed as dimers in the stressosome we assumed that these differences were caused by misalignment due to the flexibility of the N-terminal domains. For efficient refinement of the N-terminal domains the density of the reference map was multiplied with the density of a sphere of the same size but comprising different density zones. The inner part representing the core had a density of 1 while the outer part, comparable with the area of the N-terminal domains, had a density of 1.5 (map constructed with IMAGIC). This approach resulted in a reference map with higher density in the outer part, whereas the density in the core remained unchanged. Furthermore the N-terminal domains could be refined respectively (Figure 26). During optimization of the refinement the data set could be extended to a final amount of 66.200 particles.

4.2.2.2 *3D map of the VvRS stressosome*

After several refinement cycles the final map of the oxidized *Vv*RS stressosome was resolved to 7.6 Å (Figure 31A, Figure 30) showing secondary structures like α-helices and β-sheets in the core (Figure 31C).

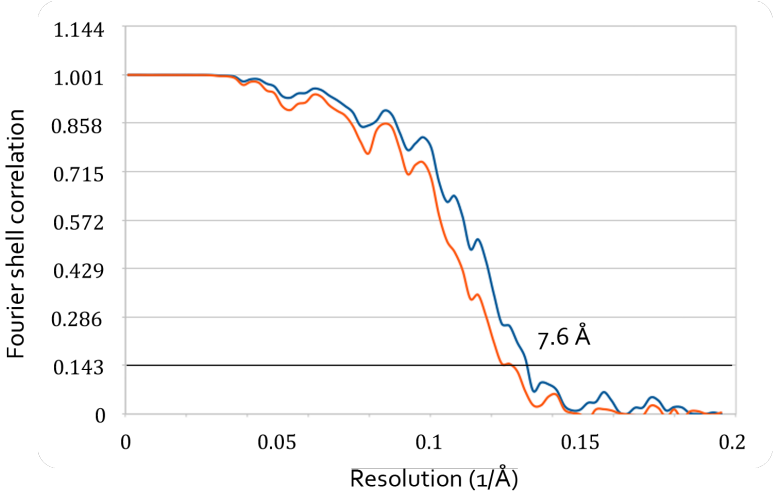

Figure 30 Fourier Shell Correlation (FSC) curve.

FSC curve is calculated from two independent data sets after soft masking (blue) and reveals a resolution of 7.6 Å for the whole stressosome. The unmasked map (red) shows a lower resolution than the soft-masked map, which indicates the real resolution of the 3D map.

The diameter of the complex is about 280 nm in total and each N-terminal dimer of *Vv*R (Figure 31B) extends for about 50 nm from the 180 nm STAS domain core. The overall arrangement is similar to that of the map obtained from Set 1 (Figure 26). Analysis of the resolution distribution with the program ResMap (ResMap, Kucukelbir et al., 2014) of the unfiltered map revealed that the core has a significantly higher resolution, between 5.5 Å and 6.5 Å, than the N-terminal domains with 8-10 Å (Figure 31D, E). The mean resolution estimated by ResMap is 7.48 Å. The reconstructed map shows the movement of the N-terminal domains by slightly differently shaped and blurred densities (Figure 31B). Based on this result the core seem to be a ridged structure whereas the N-terminal domains show a high flexibility.

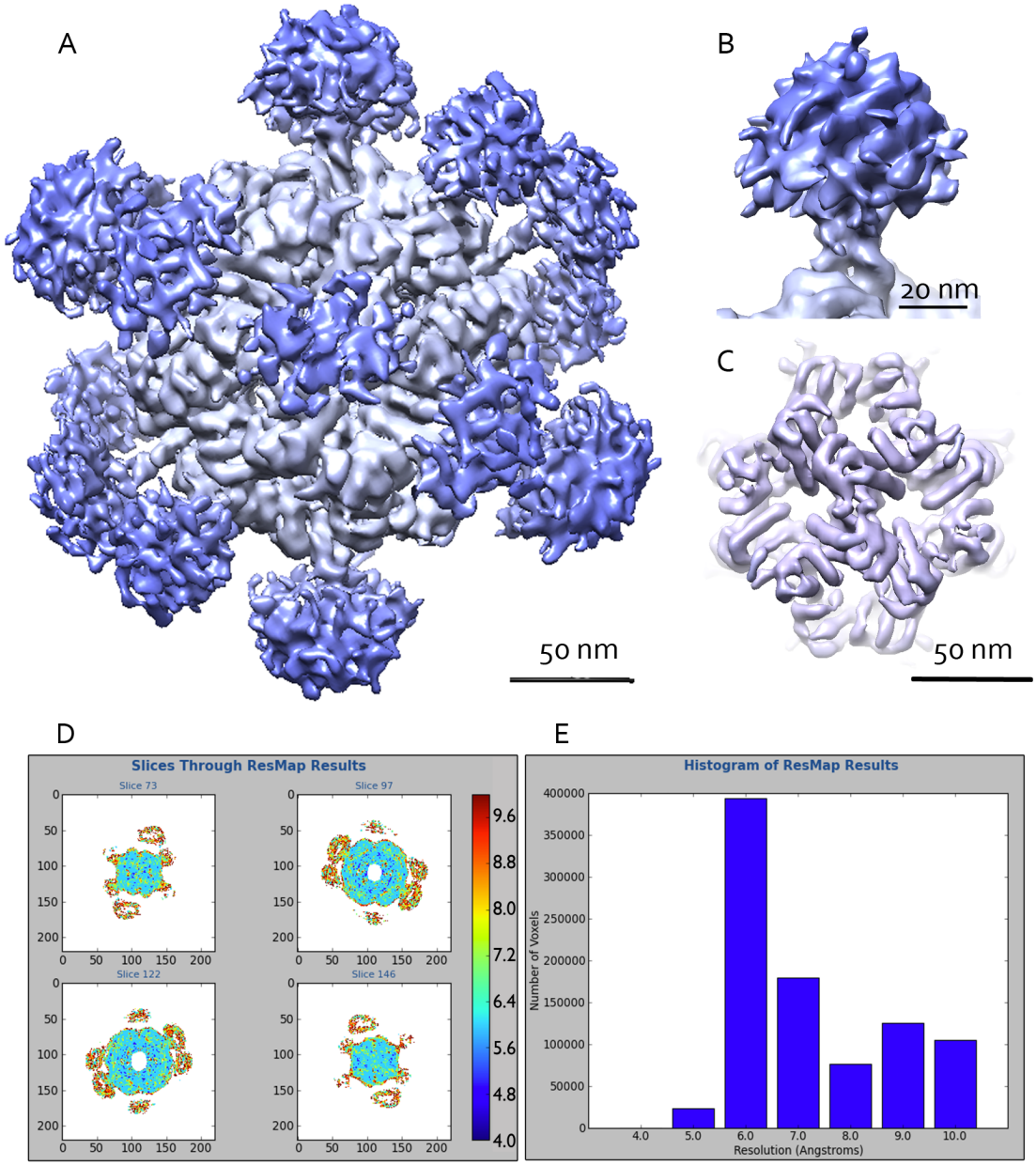

Figure 31 3D map of oxidized *Vv*RS complex at 7.6 Å

A: 3D map. The *Vv*RS STAS domain core in bright blue shows helical substructures. 20 N-terminal *Vv*R dimers form turrets are marked in darker blue. **B:** N-terminal dimer is connected to the C-*Vv*R domains of the core via linker helices. **C:** Detailed view of the core with helical substructures. A 2-fold axis is presented. **D:** The local resolution distribution computed by ResMap. The insets present slices through the map showing a significantly higher resolution for the core in a range of 5.5 – 7 Å than for the N-terminal domains that are colored orange-red, indicating a range of 8 – 10 Å. **E:** The bars visualize the quantity of each resolution class. The resolution mostly represented is 6 Å.

For reconstructions concerning Set 2 the gold-standard procedure in RELION was implemented (Scheres and Chen et al., 2012). After the refinement the map was post-processed based on the publication of Chen et al. from 2013 to establish the final resolution of the map (Figure 30).

The refinement using the particle-based approach for subframe alignment within RELION (Scheres, 2012) did not improve the resolution further which was probably caused by the low SNR at the N-terminal domains.

4.2.2.3 *Validation of the achieved VvRS 3D map*

Validation of the 3D map was conducted constantly, e.g., by monitoring the Euler angle distribution. The Euler angles for the *Vv*RS reconstruction (Figure 32) show a uniform distribution concerning the particle orientation. By means of the determination of the Euler angles from a 3D map the coverage of the particle orientation belonging to a 3D map can be visualised indicating no preferred orientation in ice on the grid for the stressosome, consequently no misalignment during the refinement procedure was caused.

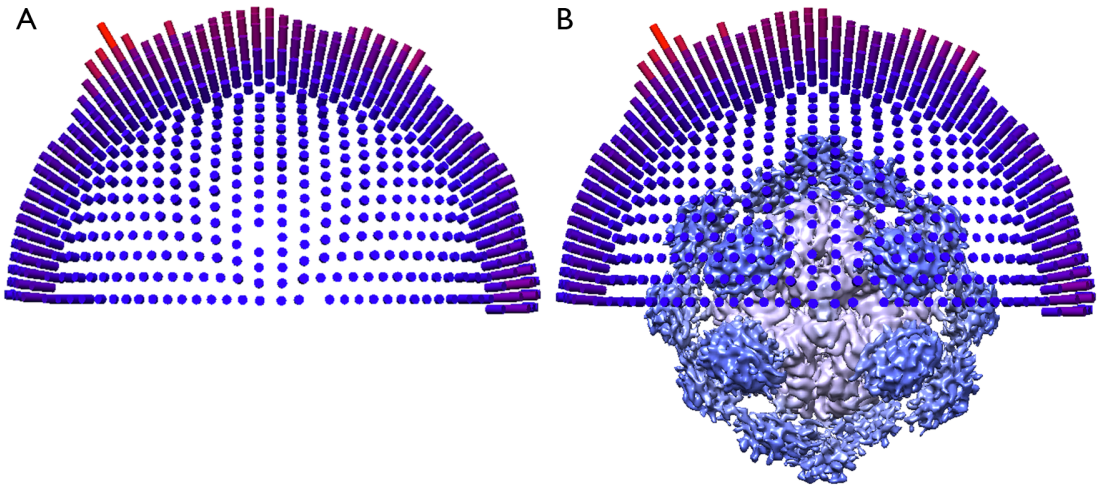

Figure 32 Euler Angles

Euler angle distribution for ¼ of the sphere *Vv*RS map. Each bar represents the sum of particles in the indicated orientation. The height of a bar corresponds to the particle number in one class. **A:** angles are visualized with only a negligible gap in the middle. **B**: the angles to the position of the 3D map are shown respectively.

To confirm that the map was not a result of over-fitting by forcing the wrong symmetry, a reconstruction without applying any symmetry (C1 symmetry) was conducted. The resulting low-resolution map is presented at all three 2D symmetry axis in Figure 33 and exhibits a similar overall composition as the final *Vv*RS 3D map

(Figure 31) showing all basic features of the stressosome. Density and conformation of the N-terminal domains must not be considered due to the simplicity of this refinement procedure. The re-projections of the map show no 5-fold symmetry, a supplemental indication of D2 symmetry (data not shown).

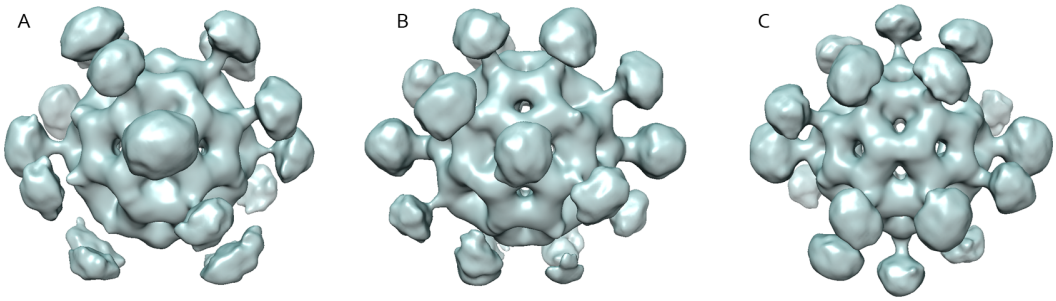

Figure 33 Reconstruction conducted by applying C1 symmetry

A-**C**: The map is represented in positions viewing down each of the three D2 axes. The overall shape is comparable to the final *Vv*RS 3D map. N-terminal domains are located at the right positions.

4.2.2.4 *Homology model of the VvRS stressosome*

For further detailed structural analysis a homology of the *Vv*RS stressosome was constructed. To generate a homology model of the STAS core (performed in collaboration with Janet Vonck and Pilar Cossio Tejada) the map of the *Bacillus subtilis* core (EMD: 1552) was taken as an orientation reference for the single domains. Homology models of the STAS domains of *Vv*R and *Vv*S were generated using the X-ray structure of the RsbS paralog *Mt*S (PDB: 3ZXN) as reference applying the program Swiss-Model (Guex and Peitsch, 1997; Kiefer et al., 2009; Arnold et al., 2006; Biasini et al., 2014). The linker helix for the *Vv*R model was constructed based on the anti-sigma-factor antagonist (STAS) domain protein Moth_1475, the RsbR homolog *Mt*R (PDB: 3ZTA) and the model for the N-*Vv*R protein was determined based on the Heme-based aerotactic transducer hemAT (PDB: 1OR6). In total the homology model comprises 60 proteins with 10 *Vv*S dimers in blue and 20 *Vv*R dimers with N-*Vv*R dimers in brown (Figure 34B)

Figure 34 shows the stressosome homology model that fitted well into the reconstructed map (Figure 31). A slice through the middle of the stressosome map is displayed in Figure 34A which shows 4 N-*Vv*R dimers and the hollow STAS domain core. A *Vv*R dimer is displayed in detail in C revealing the α-helices and β-strands of the STAS domains matching well with the densities of the map (Figure 34E). The β-strand assembly is surrounded by 4 α-helices (for comparison Figure 2B). The β-strand assembly of the *Vv*R and *Vv*S monomers face each other within a homo-dimer and form contact sides (Figure 34C). The contact sides are described in detail in chapter 5.3.4. Adjacent *Vv*S and C-terminal *Vv*R proteins are in contact as well as the dimers of *Vv*R and *Vv*S in the core.

The linker helices seem connected and their densities show a slight twist around each other in the 3D map (detailed evaluation in 5.3.2). The homology model of the N-*Vv*R monomer consists of 8 α-helices that correspond to the density of the 3D map (Figure 34C, D) but no secondary structures could be observed in the 3D map for the N-terminal domains.

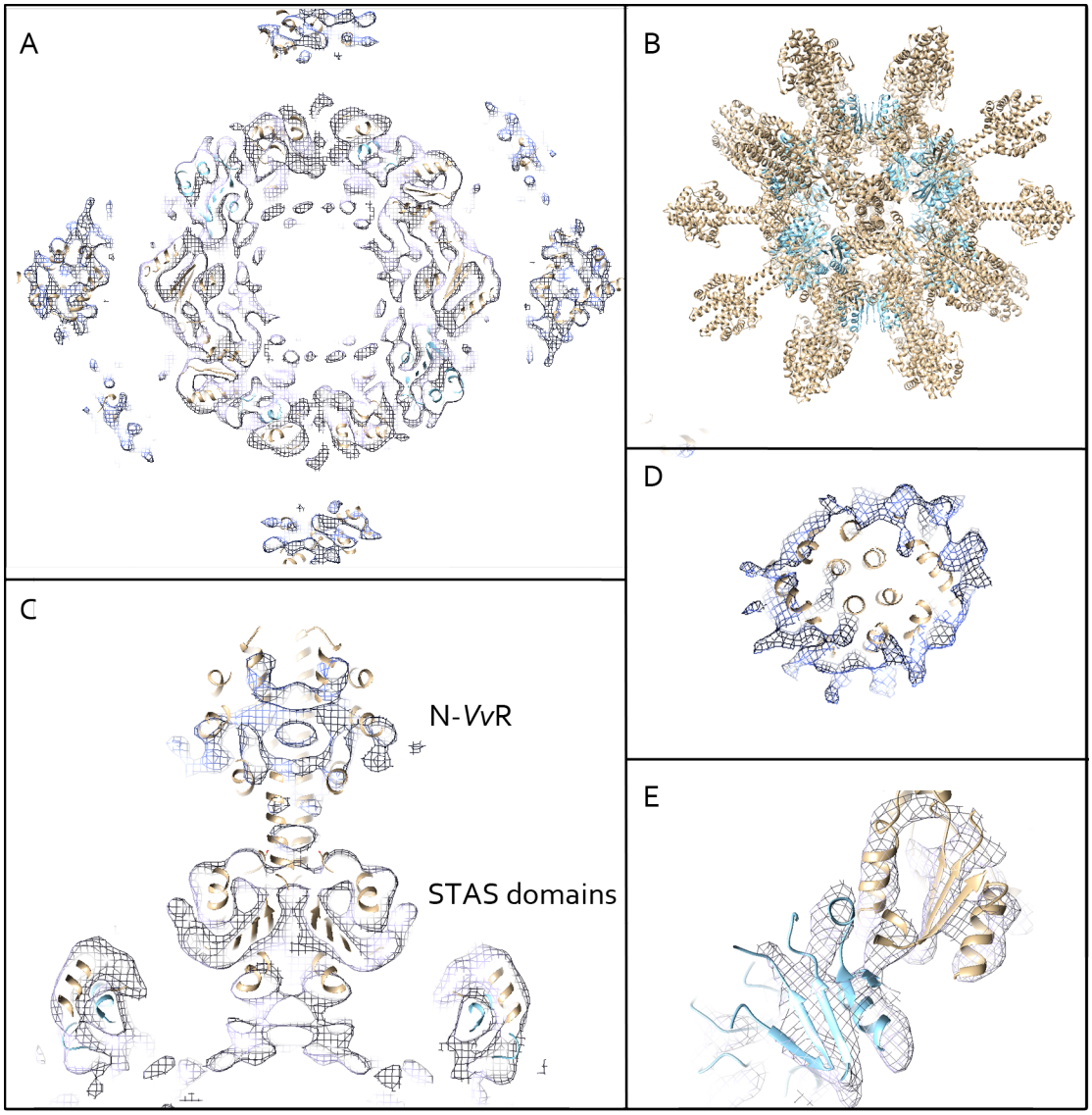

Figure 34 Fitting of the homology model into the 3D map.

A: A slice through the 3D map with the homology model is pictured. Brown *Vv*R and blue *Vv*S. **B:** shows the entire homology model of the *Vv*RS stressosome. **C:** Side view of the *Vv*R dimer. The STAS domains fit well whereas the N-terminal domains of the homology model and the map correspond roughly superimposed. **D:** Top view N-*Vv*R dimer. α-helices of N-*Vv*R fit in the density of the map but secondary structures are not present for the N-terminal domains. **E:** STAS domains in detail. The scaffold domains in the core are close to each other.

Despite the enlargement of the data set to 60,000 particles the resolution did not improve above the 7.6 Å. Therefore we subsequently focused on the investigation of the STAS domain core by performing reconstructions masking the flexible N-terminal domains.

4.2.2.5 *Reconstruction of the VvRS core complex*

The core complex appears rigid in comparison to the N-terminal domains and due to the pseudo-icosahedral symmetry ideal for further structural investigations. In order to improve the resolution for this STAS-domain assembly refinement processes were performed while adjusting specific parameters such as the change to a smaller box size, using a map as reference calculated from the *Vv*R homology model for the core filtered to 20 – 30 Å including more information and a reference mask for excluding the N-*Vv*R domains.

A 3D map was obtained with an overall resolution of 7.6 Å (Figure 35) calculated from 2 independent data sets and secondary structures were observable (Figure 36A).

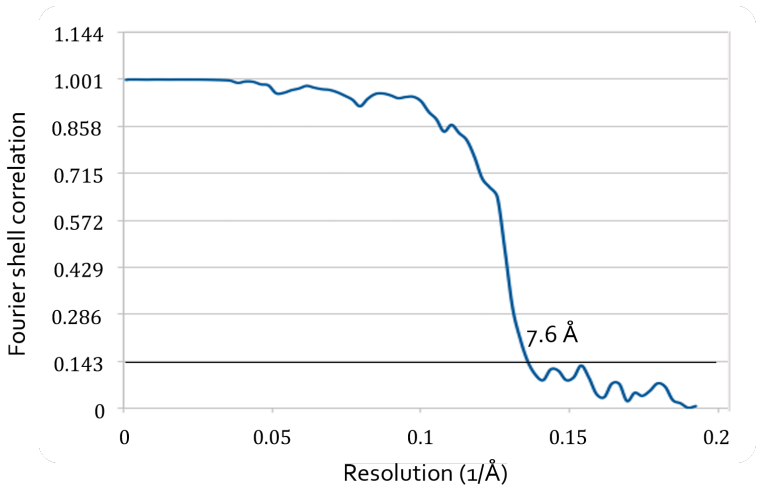

Figure 35 FSC curve of the core reconstruction

The Fourier shell correlation at 0.143 indicated a resolution of 7.6.

The local-resolution estimation with ResMap in Figure 36C-D revealed a slightly better resolution between 6 and 7 Å and the mean resolution was indicated with 7 Å. The homolog model of the STAS domain core fitted perfect into the 3D map (Figure 36B) but surprisingly no further improvements of the core reconstruction could be observed in comparison to the *Vv*RS map (Figure 31).

Based on the low resolution and the assumption that the STAS domains built a rigid scaffold, the next attempt was to increase the resolution further by cleaning the data set.

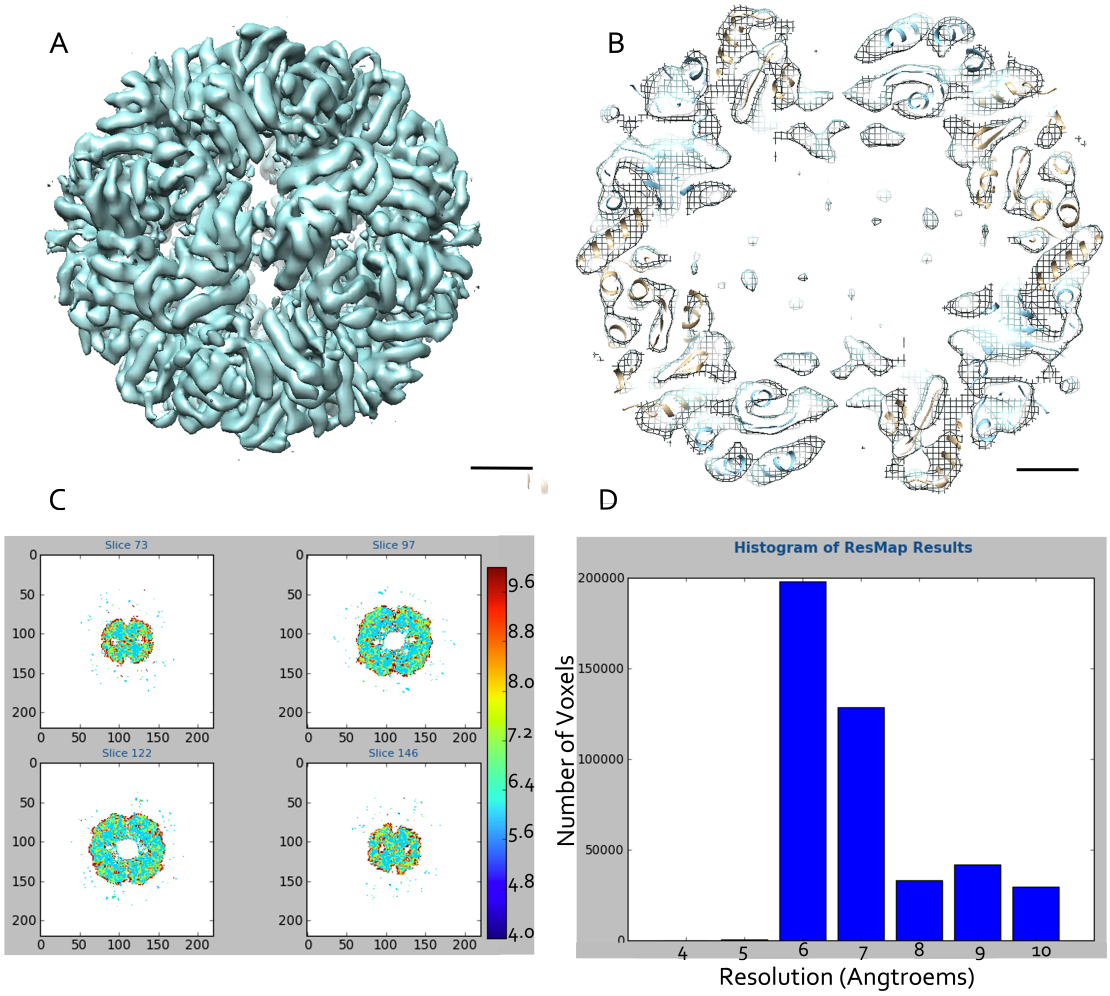

Figure 36 Reconstruction of the *Vv*RS core

A: 3D map. Secondary structures are noticeable. **B:** Section through 3D map. The STAS domains of the homology model fit into the map, *Vv*R in brown and *Vv*S in blue. **C:** The resolution distribution is displayed in insets. Slices show a range of 6 -7 Å within the core. **D**: Bars shown the quantity of each resolution class. The class represented the most is 6 Å.

4.2.2.6 *Classification of the data set*

Generally within one data set particles are integrated which do not average well with the main set due to damage, contact with other particles and contaminations or ice deformations. Classification is recommended as an approach to clean the data set by sorting out incompatible particles. The 2D classification organizes the projections with the same orientation into classes. Classes of projected particles in different orientations are determined by 2D classification and accordingly symmetry and overall arrangement of the particles can be established already (Campbella et al., 2014). Furthermore particles, which are incompatible with the data set, can be determined and excluded.

Another reason for performing a classification is heterogeneity within the data set which can be determined by 3D classification. Out of the starting set the 3D classification process separates the data into smaller associated particle sets and generates corresponding 3D maps respectively. By this means various 3D maps were produced providing additional information about conformational states of the molecule. Both classifications were employed in this work.

I) 2D classification

For the 66.200 particles in Set 2 a 2D classification was performed within the RELION workflow gaining 250 classes.

Out of these classes non-harmonizing classes, e.g. classes with particles that had parts missing or those that appear blurred, were removed (Figure 37 lower line). Set 2 was reduced to 52.000 particles. In most cases undesirable classes contained only a few particles.

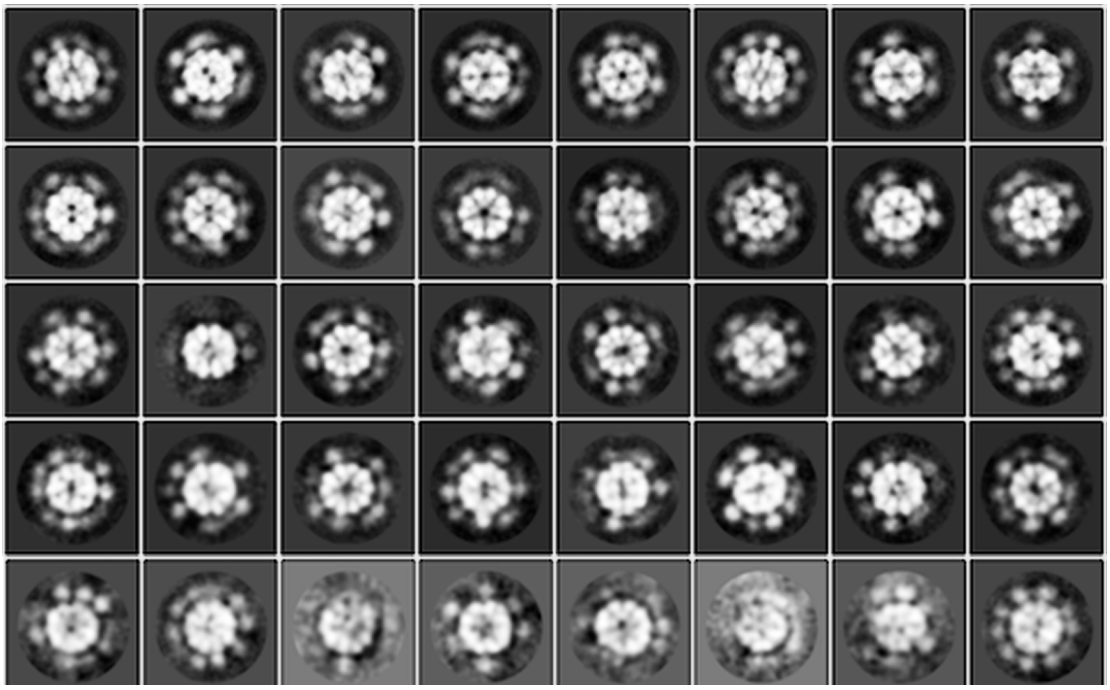

Figure 37 2D classification

A subset of class-averages is shown from the 2D classification with the *Vv*RS stressosome. The classes show 2-, 3- and 5-fold symmetry due to the symmetry mixture present in the stressosome. An irregular arrangement of the N-*Vv*R is observable. The lower line presents some classes of incompatible particles that were excluded from the data set.

Using the cleaned Set 2 reconstructions were implemented to compare the resolution before and after the 2D classification. However, in comparison to the previous map the resolution only improved by approximately 1 Å for the *Vv*RS core (Figure 36, Figure 38). Within this resolution range no differences could be observed between the maps received before and after 2D classification.

Estimation of the local resolution was performed with ResMap without masking the map, which is visible from the occurring noise around the core (Figure 38). Masking tends to overestimate the resolution in a map.

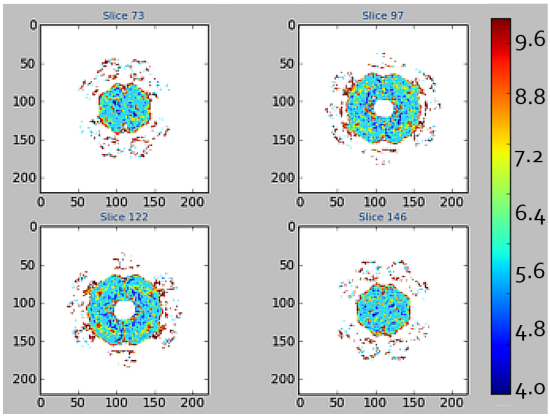

Figure 38 Resolution distribution in the *Vv*RS core after 2D classification

Insets represent slices through the core that are in a range of 5.5 to 6.5 Å.

II) 3D classification

For the evaluation, whether the resolution is dependent on the structural heterogeneity, a 3D classification was conducted using the cleaned (after 2D classification) Set 2. A 3D classification performed with the N- and C-terminal domains of the *Vv*RS complex did not lead to an adequate outcome since the weak densities are hard to recognize precisely and the program was unable to sort the particles into different classes. This effect can be visualized by displaying the change in particle amount in the classes after each iteration step. Under ideal conditions the proportion of switching particles should decrease below 10 % with ongoing refinement but in the case of the *Vv*RS stressosome 60 % particles switched classes in every round.

Furthermore only the core was included in the comprehensive 3D classification processes including the imposition of D2 symmetry, masking out N-*Vv*R by decreasing the image particle size and implementing a reference mask including only the core area. As a reference map the filtered (30 Å) homology model of the core was used.

3 structurally distinguishable maps could be obtained out of 10 (Figure 39A-C) at around 11 Å with a structure comparable to the previously gained maps of the core reconstruction.

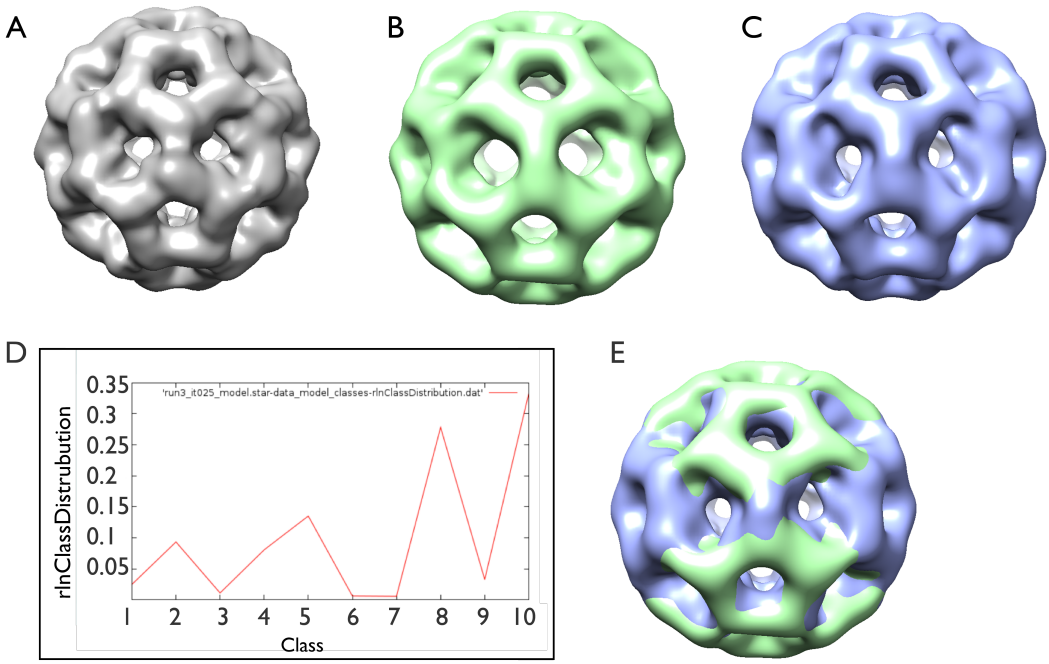

Figure 39 3D classification

A-C: Three 3D maps with the same overall fold. **D:** Diagram displaying the single maps and the corresponding particles, starting with the lowest yield. The first map in grey (class 10) yields the most particles followed by the second, the green map (class 8). The third map in blue (class 5) contains 10 % of the data set. **E:** Map 2 and map 3 superimposed, the elongation is visible.

The map with the highest data yield is map 1 (Figure 39A, grey) that contains 33 % of the particles followed by map 2 with 27 % particles (Figure 39B, green) and map 3 with 14 % of the particles (Figure 39C blue). The remaining particles are spread over maps with insignificant data volume and are therefore not situable for further analysis. The three maps show slight differences in the core shape noticeable by superimposing. For map 3 a stretch along the horizontal axis is visible while map 2 extends vertically pointing a contract-stretch motion of the core (Figure 39E). This result indicates an unexpected flexibilty for the core which was supposed to be rigid,

providing an explanation for the stagnation of the resolution during refinement. The Euler angles of all three classes show an equal orientation distribution of particles, no missing orientations were obtained.

Reconstructions of the 2 main 3D classes (Figure 39, grey and green) were performed using the 3D class as reference maps and the corresponding particle data sets. First with map 1 in Figure 39A in grey and the corresponding data set of around 20.000 particles and secondly with the slightly horizontally expanded map 2 (Figure 39B green) with 7.000. The reconstructions were conducted in the same way as the previous 3D classification by imposing D2 symmetry, using the filtered homology model as a reference map and a reference mask that excluded the N-*Vv*R. In Figure 40 the results of the reconstructions are displayed. For map 1 a resolution of 8.3 Å was obtained showing a round core and first helical substructures while map 2 had a resolution of 11.1 Å still vertically expanded. The Euler angle distribution showed no orientation preference of the particles (data not shown).

In conclusion: A successful classification was conducted indicating a structurally heterogenetic data set in terms of the *Vv*RS STAS domain core. The 2D classification improved the resolution for a small step size. Flexibility of the core could be verified with 3D classification.

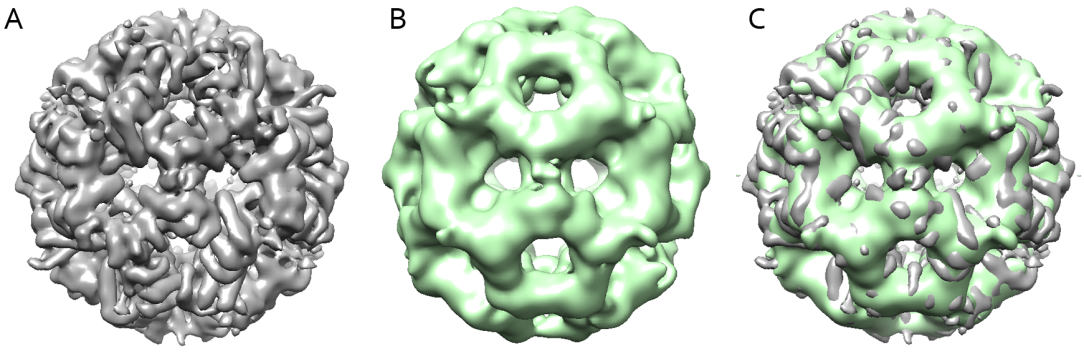

Figure 40 Reconstructions of the 3D classification

A: Map of class 1 (grey, core round). Substructures of the core are detectable. **B:** Map of class 2 (green, core more oval). Color scheme as in Figure 39. **C:** A slight stretch of the green map is observable if compared to the grey one.

4.3 Computerised studies of a dynamic system

In order to support the findings of flexibility and heterogeneity observed by single-particle analysis computerized studies were performed in collaboration with Pilar Cossio Tejada at the MPI for Biophysics in Frankfurt, who has provided the data presented in the next paragraph.

4.3.1 Characterising the stressosome flexibility with BioEM (Bayesian inference of EM)

To further characterize the conformational dynamics of the stressosome core the BioEM algorithm (Cossio and Hummer, 2013) was used. To obtain the most likely flexibility for the core over 710 individual particle projections were used. The flexibility was calculated considering the slowest independent normal modes that describe the most probable direction of the motion of a system (Jin et al., 2014; Tama et al., 2004). The normal mode and BioEM analysis was done on a low filtered map of the core (Cossio and Hummer, 2013). Figure 41 shows the probability of the generated models with respect to the symmetric core (homology model). The probability is shown as a function of the motion along the direction of the two most probable models: first ranking model (green) and second ranking model (purple). Positive numbers indicate that the movements in the model are more probable than the symmetric core (homology model). However, it is important to note that these movements are in the order of 2-4 Å.

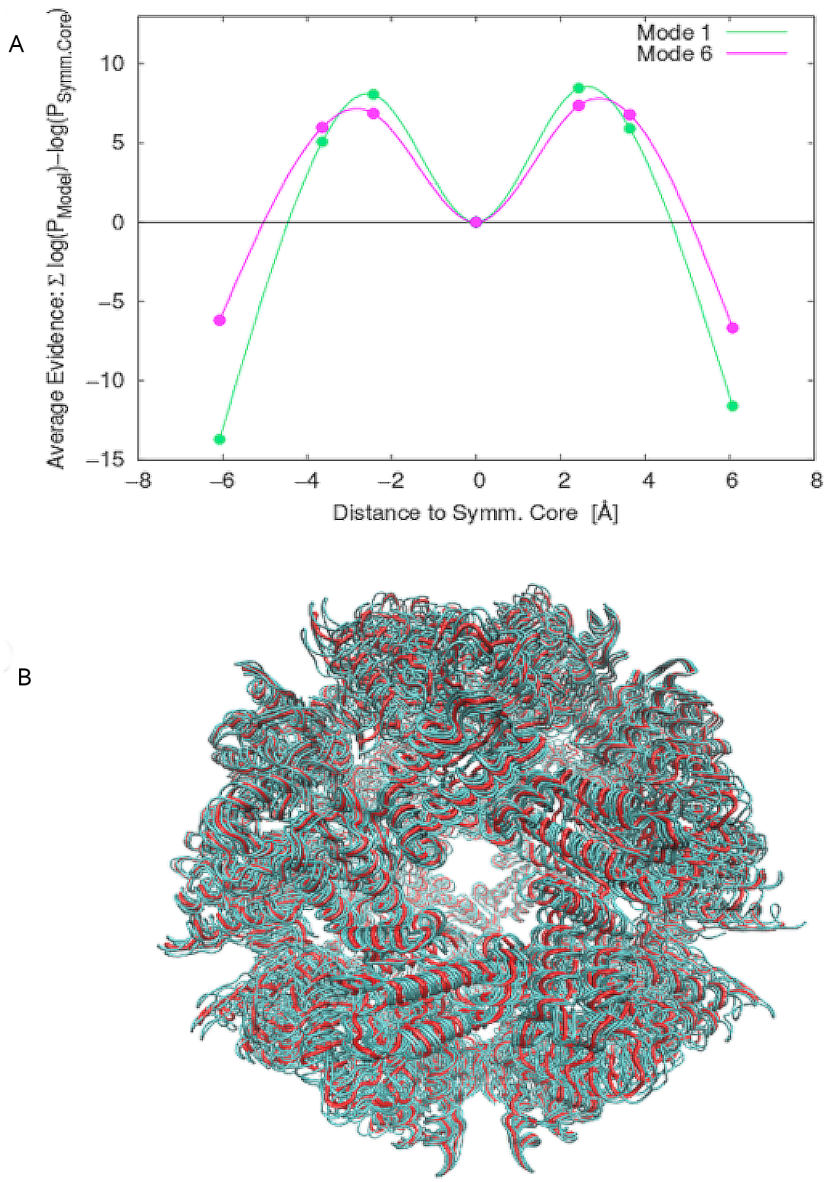

Figure 41 Average probability of core movemnet

A: Average probability, calculated with the BioEM method (Cossio and Hummer, 2013) with respect to the symmetric core. The curves show as a function of the displacement in Å the two most probable normal modes: 1 (green) and 2 (purple). Positive numbers at the y-axis indicate that the model showing movements has a higher probability than the symmetric core. The rigid core is represented as 0 on the x-axis. Both models show that movement between 2 and 4 Å is the most probable since this range is found at the highest positive y value. **B:** Represents the dynamic models in blue as an overlap of the best models for these directions relative to the symmetric core (red). As reference the symmetric core (homology model) is shown. Both models 1 and 2 have a higher posterior probability than the core.

These results indicate that the stressosome core is modestly dynamic with movements of 2-4 Å; this flexibility complicated the improvement of the resolution when using standard structural refinement techniques like single-particle analysis.

For the calculation of the dynamics of the core the particle projections were masked to exclude N-*Vv*R starting from the connection between core and N-terminal domains. To confirm that these results are not an artifact of the linker helix density in the experimental images 100 synthetic images of the homology model with and without the N-terminal domains were created, termed *test* and *control,* respectively. We used the BioEM protocol over the slowest independent normal modes (similarly as it was done with the experimental images described above) to validate if the linker density affected the BioEM characterization of the core. Figure 42 shows some representatives of the synthetic images for the *test* and *control* sets. Those were generated with random orientations. To create synthetic images with random signal-to-noise ratios the normalization and noise standard deviation were selected. The average probability with respect to the symmetric core is shown in Figure 42B as a function of the movement over the first slowest mode. We found that both in the *control* and *test* sets, the symmetric core is the most probable structure, confirming that the likely movements around 2-4 Å that were assessed in the experimental images are not artifacts of the extra N-terminal domains *Vv*R density.

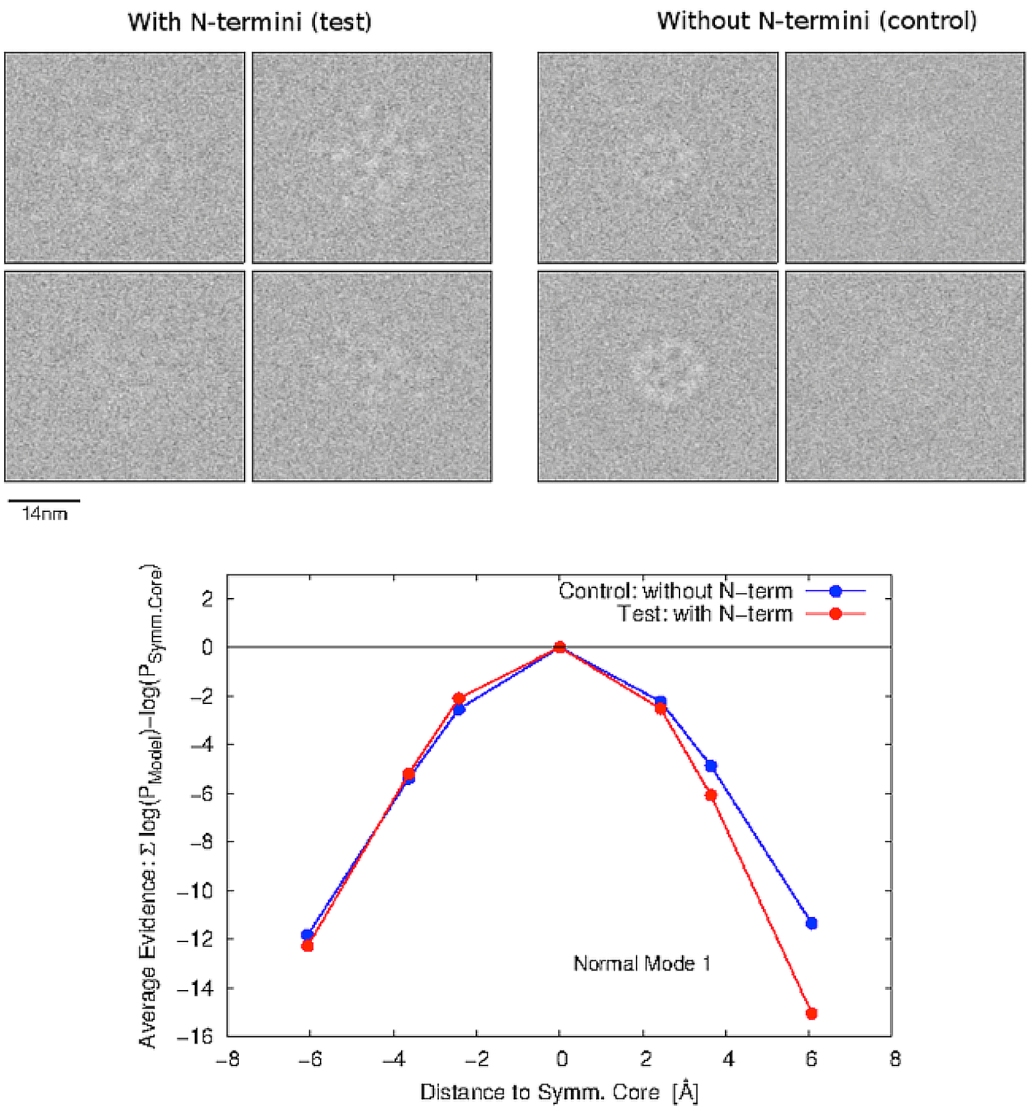

Figure 42

A: Representatives of the images of the synthetic maps with (*test*) and without (*control*) the N-terminal domains. **B:** The average probability with respect to the symmetric core. The average probability is shown as a function of the movement in Å for the test (red) and control (blue) synthetic map sets. The symmetric core is the most probable structure for both sets, indicating that the dynamic effect that we find in the experimental images is not an artifact of the extra N-terminal domain density in the experimental images.

5. DISCUSSION

In this work two different stressosome complexes were investigated. The *Listeria innocua* RS and RST complex was analysed biochemically and by single-particle negative stain EM, the *Vibrio vulnificus* RS complex was investigated by single-particle cryo-EM. This thesis for the first time presents the evidence that Listeria have RST genes encoding for proteins that assemble to a stressosome complex. We could show that the core of the stressosome of *Vibrio vulnificus* is highly flexible.

5.1 The *Listeria innocua* RST-proteins

Expression and purification of all three stressosome proteins was successful (Figure 13, Figure 16) and by negative stain EM the complex formation of *Listeria innocua* R and S proteins could be demonstrated (Figure 18). In blue native polyacrylamide gel electrophoresis (BN-PAGE) the molecular weight of the *Li*RS complex is around 1.2 MDa approximately in the same range as the *Bs*RsbRS stressosome with a calculated mass of 1.5 MDa (Delumeau et al., 2006). The differences in MW can be attributed to the theoretically calculated mass of the *Bs*RsbRS complex, the limited accuracy of BN and the round shape of the particles causing the lower MW. During the co-expression of *Li*R and *Li*S a ratio of approximately 2:1 *Li*R to *LiS* (Figure 13) was determined comparable to the ratio found in the *Bacillus* stressosome (Delumeau et al., 2006; Marles-Wright et al. 2008).

The oligomerization of *Bs*RsbR was already described by Cheng et al. 2003. It is assumed that this self-assembly holds for all RsbR homologs. The ability of *Li*R to self-assemble contributes to the slightly higher ratio of *Li*R to *Li*S visible in Figure 17 and also observed for *Bs*RsbR by Delumeau et al. 2006. The characteristic of *Bs*RsbS of not being able to form higher oligomers *in vitro* (Chen et al. 2003) is assumed for *Li*S likewise.

Moreover we could show that the binding of *Li*T to the *Li*RS complex (Figure 17) is weaker than expected. There are two possible explanations for this reduced interaction. (I) *Li*R forms homo-oligomers, but *Li*T requires *Li*S to bind to the

complex (Figure 17); and II) the stressosome is present in an activated state. Assuming that the *Li*RS complex is activated by a yet unknown condition during the expression and purification process a binding of *Li*T to *Li*S is not possible. Activation can take place via phosphorylation of *Li*S by *Li*T or even without previous phosphorylation as recently published by Gaidenko et al. 2014. They proposed a second activation pathway for the *Bs*RsbRS stressosome without phosphorylation of the RsbS Ser-59 residue and suggested a signal-induces conformational shift as signalling response that leads to activation of RsbT.

EM investigations confirmed the complex formation of *Li*R and *Li*S (Figure 18). No distinguishable features occur in comparison to the *B. subtilis* complexes (Cheng et al., 2003) or to *M. theromacetica* (Quin et al., 2012) at this low resolution. The class sums conducted with the negative stain images show first indications of symmetry as can be seen in Figure 19B and C the 2- and 3 fold.

In vivo detection of *Li*R was successfully performed by applying a specific antibody for N-*Li*R to the crude cell extract and as a result the expression of all stressosome proteins can be assumed. The observed blot signal was weak which is in good agreement with the observation of Marles-Wright and co-workers who could determine only 20 stressosomes per cell via immunofluorescence and independent of stress, the number of stressosome complexes remained the same. For prompt stress detection and mediation the complex is permanently present, ensured via transcription control by the housekeeping σ-factor σ^A and not by stressosome controlled σ^B factor. Interestingly the *Listeria* stressosome appears to be able to respond to nutritional stress as well as to environmental fluctuations (Martinez et al., 2010), contrary to the *Bs*RsbRST stressosome. However as aforementioned, until now the sensing parameters and stress factors of the *Listeria* stressosome as well as for many other bacterial stressosomes are unclear.

The stressosome formation of *Bacillus subtilis* and *Moorella thermoacetica* was confirmed via EM (Chen et al, 2003; Quin et al. 2012) as well as that of the *Vibrio vulnificus* stressosome (Jan Pané-Farré, unpublished data). In this work the first evidence for the *Listeria innocua* stressosome formation is presented. For *Mycobacterium marinum* the RsbRST stressosome proteins could be expressed and by the use of the two-hybrid system protein interaction was determined (Pettersson

et al. 2013). In *M. marinum* the RST proteins regulate the σ^F factor under various environmental stress conditions (oxidative, stationary and cold stress). The σ^F factor is a homolog of the σ^B factor and the sporulation specific σ^F factor in *B. subtilis*. Interestingly the expression level of the *rsb*RST genes of *M. marinum* changes under certain stress influence. Hence the possibility is given that the expression of the RST proteins is regulated likewise by the sigma-factor which is under their control, σ^F, contrary to the *B. subtilis* and *L. innocua rsb*RST-gene expression.

The downstream of the RST module located regulatory assembly is present in various modifications among the bacteria and the components of the RST module vary as well as in terms of detection as in activation pathway. Less is known about the activation mechanism of the downstream proteins and their function in the context of stress response requires further investigations.

5.2 The oxidized *Vv*RS stressosome

Since the first structural data on the *Bacillus* stressosome by Marles-Wright et al. in 2008 to our knowledge no further single-particle analysis of a stressosome was published, even though this complex appears very suitable for single particle cryo-EM. In this work the 3D map of the *Vibrio* stressosome complex at 7.6 Å resolution revealed a yet not anticipated flexibility of the stressosome core (Figure 26).

The established diameter of the *Vibrio* stressosome is 280 Å whereas Marles-Wright and co-workers described the diameter for the *B. subtilis* stressosome being 300 Å, 20 Å more than of *V. vulnificus*. There are two possible considerations: (1) this difference could be constituted by the data collecting approach with different cameras and electron microscopes or (2) the *Vibrio* stressosome might be larger than the *Bacillus* one. However, the additional helices of the N-*Vv*R homology model did not extend the N-terminal domains in length (Figure 44B) and have no influence on the size in total.

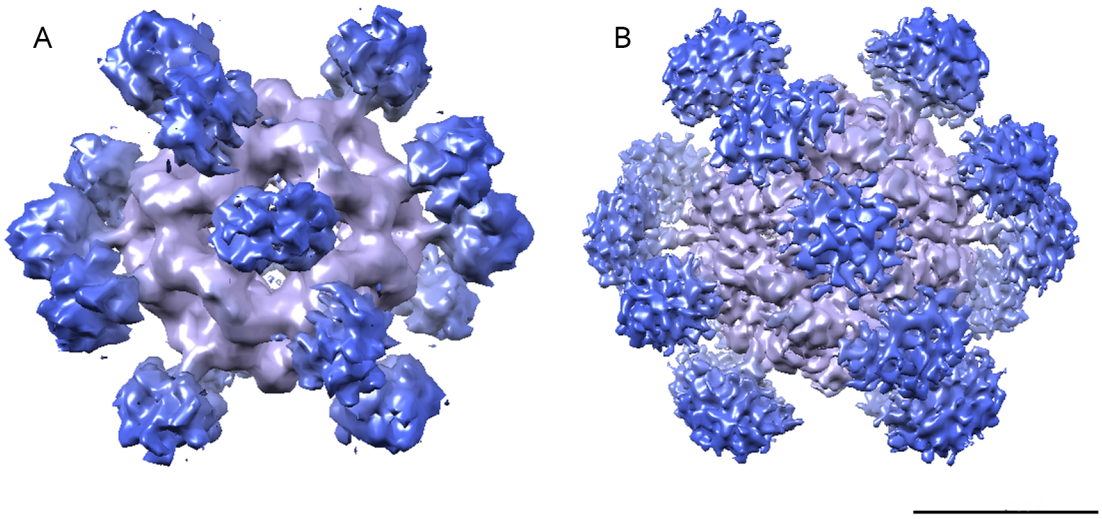

Figure 43 The *B. subtilis* map at 8.0 Å and the *V. vulnificus* map at 7.6 Å

A: *B. subtilis* map (EM Data Bank (EMDB): 1555). **B:** *V. vulnificus* map. Both maps are positioned in the same orientation with a 2-fold as front view. The overall structure is similar but the *V. vulnificus* map displays substructures in the core whereas the *B. subtilis* map appears at lower resolution. The N-terminal domains of *B. subtilis* are more rigid compared to the N-*Vv*R. Scale bar: 100 Å.

Furthermore the 3D map of *B. subtilis* at 8 Å (FSC 0.5 criterion) in contrast to the *Vv*RS complex shows no substructures (Figure 43). Only in the 3D map of the *Bacillus* core (EMDB: 1552) at 6.5 Å substructures are observable. Generally the *Vibrio* stressosome reveals more details than the core of the *Bacillus* stressosome.

Verification of the *Vv*RS 3D map including D2 point-group symmetry was conducted with multiple methods e.g. 2D and 3D classes, Euler angle distribution and reconstructions under various aspects. The class averages of the projections and map re-projections correspond to each other indicating that the classes and the map are identical. In the class sums and eigenimages of *Vv*RS 2-, 3- and 5-folds occur as well as 2-fold symmetry combined with an irregular arrangement of the N-terminal domains due to the pseudo-icosahedral core in combination with the D2 point-group symmetry (Figure 25, Figure 26). The reconstruction without symmetry (C1) yielded a map with the same overall arrangement and the Euler angles presented in Figure 28 show a uniform distribution indicating clearly the absence of an orientation preference of the particles. In case of orientation preference the resolution would be anisotropic as observed by Ludtke et al. in 2001. Based on the 3D maps of *Bs*RsbRS and *Vv*RS it can be concluded that the stressosome complexes in various bacteria have the same overall composition (Figure 43).

The 3D classification was an elegant and efficient way to understand the resolution limit of the *Vv*RS core revealing an intrinsic flexibility that was confirmed by BioEM investigation that showed a higher probability for a dynamic model than a rigid structure. Furthermore the BioEM procedure excluded implemented bias due to the N-terminal domains (Figure 42). The established conformational rearrangement within the core involves all STAS subunits and we were able to display the three main states of the movement. Based on these results we conclude that the activated (oxidized) *Vv*RS complex is highly dynamic, performing contract and stretch motions (Figure 41). Consider that the activation state of the stressosome may lead to an even higher flexibility. The motion of the core is determined to be within a range of around 3 Å (Figure 41) and represented in the 3D classification maps (Figure 40). With a comparable amount of particles (25.000 single projections)

an improvement for the *Vv*RS map from 19 Å for Set 1 to 9 Å for Set 2 was achieved by the use of the new camera and approaches for image quality optimization.

Sorting the particles by 3D classification led to a reconstruction performed with 20000 particles revealing α-helical and β-strand substructures at 8.3 Å (Figure 40A). Commonly the resolution of a 3D map increases with number of particles used but this map was obtained with a much more efficient reconstruction containing a cleaned data set.

5.3 Towards the activation mechanism of the *Vibrio* stressosome

5.3.1 Flexibility and Function of RsbR N-terminal domains

The N-terminal domains have a lower resolution compared to the core region (Figure 31, Figure 34D), a limitation caused by their flexibility, producing smeared-out densities with no secondary structures visible (Figure 31, Figure 43). Such resolution limitations caused by flexibility have been observed for other proteins, e.g. Ludtke et al. in 2011 investigated the Ca^{2+} release channel IP3R1 and the final map indicated a resolution around 10 Å. A later validation of the same data by the gold-standard method by Ludtke and Serysheva in 2013 corrected the resolution to 17 Å. Despite the limited resolution the overall shapes of the N-terminal domains were comparable and allowed to fit the homology model of N-*Vv*R dimers into the densities.

The N-terminal domains of the *Bs*RsbR map appear rather dense in comparison to the N-*Vv*R domains, which appear more flexible, considering the map in Figure 43. Depending on their activation state the increased flexibility of the N-*Vv*R domains could be constituted by binding of the cofactor. Interestingly Dorn et al. showed in 2013 for the N-terminal region of YtvA, the light sensitive RsbR homolog, that this domain exhibits more stability when the cofactor flavin is bound.

*Vv*R has the typical composition of a sensor protein consisting of a detector domain N-*Vv*R that is coupled to corresponding regulatory STAS output domain. The sensor domain of the *Vv*R ortholog HemAT in contrast is linked to a methyl-accepting domain, a domain that mediates chemotaxis as response to changes in the environment (Hou et al., 2000; Zhang and Phillips, 2003). Both sensor domains share a sequence identity of around 20 %. The homology model of the N-*Vv*R protein is based on the structure of HemAT and exhibits the same composition of eight helices (Figure 44) as well as the conserved proximal histidine (His-102) that is likewise located in the F helix as His-123 of HemAT (Figure 44).

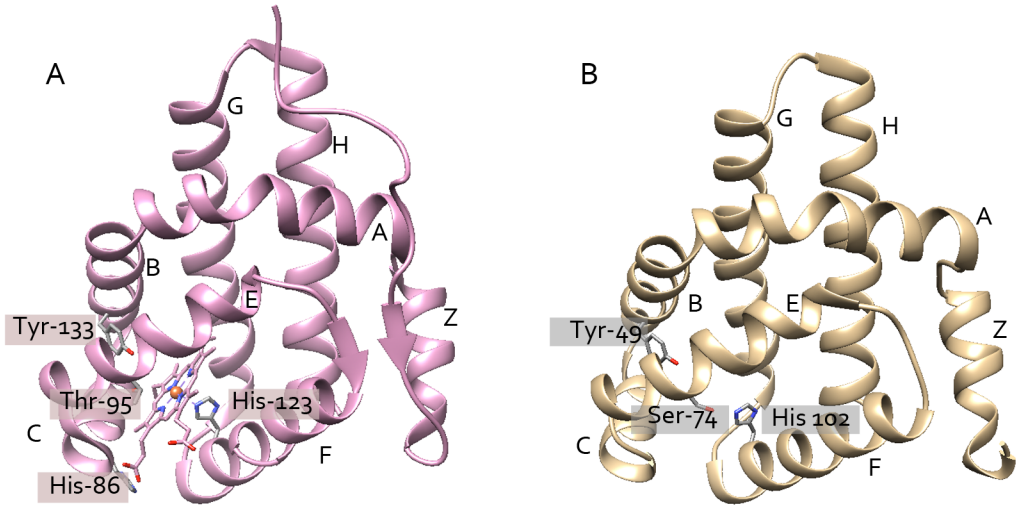

Figure 44 Structure of HemAT and homology model of N-*Vv*R

A: Oxygen sensor HemAT of *Bacillus subtilis* (PDB ID: 1OR6). **B:** Homology model of N-terminal *Vv*R. The homology model of N-*Vv*R shows the same overall fold and helical arrangement as HemAT respectively. The helix labeling for *Vv*R corresponds to the nomenclature of the globin fold as for HemAT (Zhang and Philips, 2003). Both structures have the proximal histidine residue (HemAT-His123, *Vv*R-His102) for iron-heme coordination at the F helix. The heme pocket in HemAT is directly located between the F, C, E and G helices. For *Vv*R it appears much likely that the heme pocket is positioned in the same manner. The involved heme-binding residues are displayed for HemAT and for *Vv*R respectively. Thr-95 is replaced by a serine; a similar residue to His-86 of HemAT could not be detected in *Vv*R.

The *Vv*-His-102 is supposed to be responsible for the iron-heme coordination in N-*Vv*R (Pané-Farré in communication) and might trigger conformational rearrangements within the N-*Vv*R that are further transmitted via the linker helix to the STAS domain. In HemAT the His-123 residue moves upon binding oxygen; this movement in turn leads to conformational changes in the sensor domain (Zhang and Phillips, 2003; Yoshida et al., 2012). Further heme-interacting residues in HemAT are located at a distal position; the Thr-95 at the B helix interacts with the heme bound oxygen along with the His-86 residue (Figure 44). The sequence of *Vv*R exhibits an equivalent Thr residue but lacks an equivalent to His-86 in this region (Figure 45).

For comparison in Figure 47 the sequence of the N-terminal domain of *Bs*RsbR shows no histidine residue equivalent to His-102 indicating no oxygen sensitivity. And additionally the crystal structure of the N-RsbR dimer published by Murray et al. in 2005 (Figure 5) exhibits no heme pocket as found in HemAT; the helices of the N-RsbR are positioned too close to bind a cofactor.

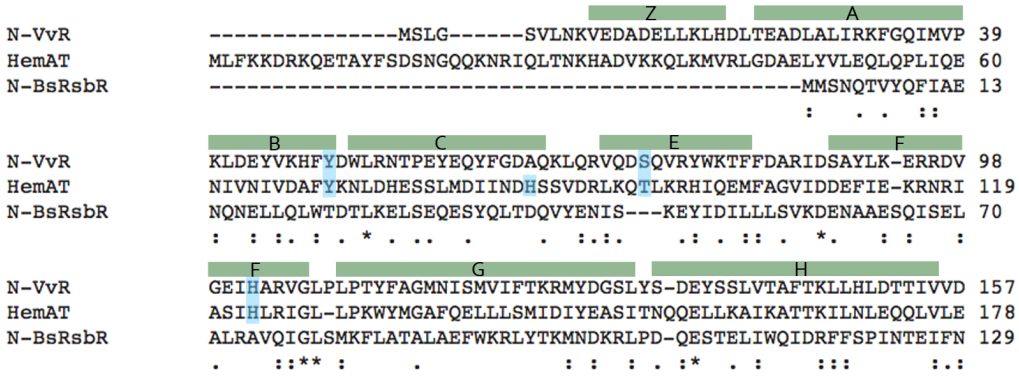

Figure 45 Sequence analysis of N-terminal domains of *Vv*R, *Bs*RsbR and HemAT

Displayed are all 3 sequences in comparison. For *Vv*R and HemAT the helices are marked and labeled in green. Conserved and similar residues are marked in blue. The sequences of *Vv*R and HemAT exhibit the conserved histidine in the F helix but *Bs*RsbR lacks the residue. The Tyrosine (Y) residue in the B helix is conserved but the Threonine (T) is replaced by a Serine (S) residue. The additional histidine in helix C is not present in *Vv*R. The *Bs*RsbR shows neither of these residues.

The sequence identity of *Bs*RsbRA and *Li*R is approximatly 50 % (Figure 46). Both have a similar amino acid length and for both the trigger is completely unknown. The N-terminal domains share an identity of 20 %, which is comparable to the similarity of *Vv*R and HemAT. Due to the similarity we conclude the same overall fold of 6 helices for *Li*R as for *Bs*RsbR (Figure 5A).

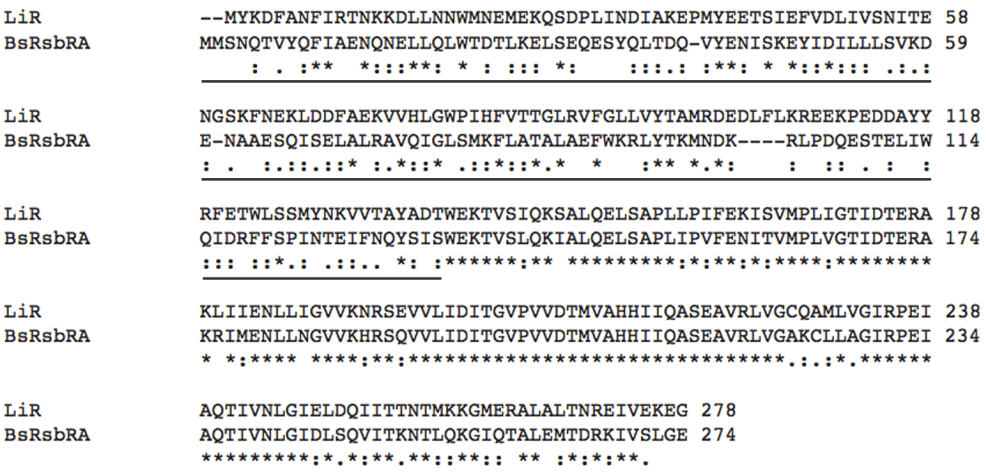

Figure 46 Sequence alignment of *Li*R and *Bs*RsbR

The identity of *Li*R and *Bs*RsbR is around 50 % for the entire protein sequence. The N-terminal domains are underlined in grey and hold a similarity of about 20 %. The amino acid numbers are similar: for *L. innocua* (278) and for *B. subtilis* (274).

The non-heme globin fold domains of the related *Bacillus anthracis* are assumed to be triggered by cellular components like fatty acids and chloride. Hence they could be sensitive to changes in fatty acid synthesis, chloride concentration or pH. These domains exhibit a special chamber and tunnel for the recognition of ligands (Stranzl, 2011). However such structural features are not existent in *B. subtilis* RsbRA and intracellular sensing appears unlikely. Gaidenko and co-workers presented findings that substitutions of the N-terminal domain in *Bs*RsbR do not influence the response level to ethanol and salt stress (Gaidenko et al. 2012) concluding that none of these described factors seem to be the signal for *Bs*RsbR. In spite of these findings it was proposed that sensitivity to an unknown cytoplasmic parameter exists but that the N-terminal domain and the helical linker do not use the usual N-terminal to C-terminal transmission route for signal transmission (Gaidenko et al. 2012). Due to the close relationship of *Bacillus* and *Listeria* a similar sensitivity can be suggested. An unknown specific signal could be responsible for the activation of the *Li*RS stressosome during the performance of our biochemical studies, hence activating the *Li*RS complex and leading to less *Li*T binding in our binding assay (Figure 17).

5.3.2 The linker helices of RsbR like proteins - a transmitter and interaction partner

All RsbR stressosome proteins including *Vv*R comprise a helical interaction domain that is assumed to transmit the signal from N-*Vv*R to the STAS region (Pané-Farré, unpublished data). This was assumed for the linker helix of YtvA (Möglich and Moffat, 2007) as well as for the linker helix of *Bs*RsbRA (Gaidenko et al., 2012). The linker helices of RsbRs from different species reveal a conserved sequence of 13 residues, suggesting a similar role in transmission of signals to the STAS (Gaidenko et al., 2012). The linker of *Bs*RsbRA has conserved residues that constitute to an inner and outer surface within the linker dimer (Figure 6). Substitutions of conserved residues increase the steady-state output from the stressosome and substitutions on the non-conserved outside decrease the output. Therefore, two different contact partners are assumed for both sides. The inner side is in contact with the second helix while the outside is presumed to have contact with other reaction partners.

For the Jα-helix dimer of YtvA studies showed a conformational change by signal input that resulted in a turn of both linkers around each other and by this conformational change the transmission to the STAS domain (Möglich and Moffat, 2007) takes place. A similar turn of two linker helices of *Vv*R could be observed in our map of the oxidized (activated) *Vv*RS stressosome (Figure 31B).

5.3.3 The STAS domains - flexibility as functional feature

The final 3D map allowed of fitting the homology model and in particular the STAS domains matched excellent with the density (Figure 34). The model of the STAS protein *Vv*S shows a minimal variance, possessing five instead of the typical four β-strands for STAS domains (Figure 47), whereas the *Vv*R model presents the general overall constitution of four β-strands.

NMR investigations with the STAS domain comprising rat prestin suggested dynamic features for the STAS domain (Pasqualetto et al., 2010) and MD (Molecular Dynamics) stimulations by Sharma et al. (2014) confirmed this flexibility at or near the α1 and α2 helical region of prestin (nomenclature analog all STAS and as in Figure 2B or Figure 47C). Prestin mediates sound amplification in the mammalian hearing organ and its STAS domain shares a conserved overall fold with RsbR. Furthermore the same group detected a similar flexibility of the STAS domain of human pendrin, an ion transporter showing that helix α1 and α2 of both proteins perform conformational changes. These finding support our result of the flexible stressosome *Vv*RS STAS domains. Structural rearrangements occur within the core either permanently or most probably by activation after signal detection of the N-terminal domains.

In the homology model as well as in the map of the *Vv*RS stressosome the helices α1 and α2 of *Vv*R and *Vv*S are closely positioned to the linker helices and in contact with the α3 helix of an adjacent core protein (Figure 47D). Within one STAS domain both helixes (α1 and α2) are connected via loops that point toward the N-terminal domains. Due to the location of the putative flexible α-helices α1 and α2 a conformational change could be transmitted to the adjacent *Vv*R α3 helix or an adjacent α3 helix of a *Vv*S protein and spread to further STAS domains (Figure 47D). Interestingly the two phosphorylation sites of *Vv*R are located in the N-terminal region of α1 and α2 helix (Figure 47B). This arrangement is equal for the α1 and α2 helices of *Vv*S and *Vv*R dimers.

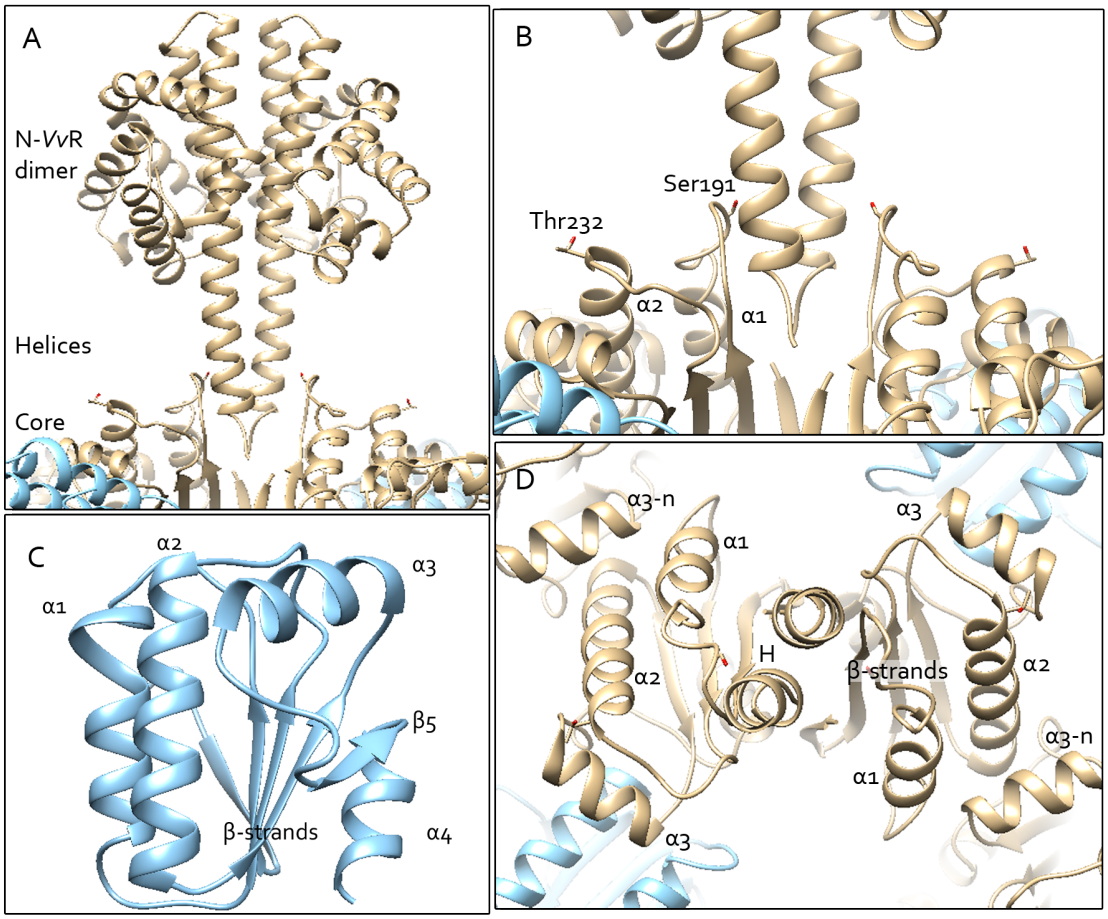

Figure 47 Homology model of *Vv*RS

A: *Vv*R dimer in side view. **B:** Detail from A showing phosphorylation sites of *Vv*R and the linker helices. *Vv*R is pictured in brown and *Vv*S in blue. Ser191 is closely located to the linker helix (H) visible in **B** and Thr232 lies between β3 and α2. In the homology model the residues are presented easily accessible. The homology model is composed out of several single model parts, thus the connection between STAS domain and linker is missing. **C:** Single STAS domain protein *Vv*S with 5 β-strands. **D**: *Vv*R dimer in top view (B rotated by 90°), N-terminal dimers are cut. The positions of helices α1 and α2 are indicated and visible closely located to the α3 helix of the adjacent *Vv*R STAS domain (α3-n). The α3 helices of *Vv*R are closely located to the α1 and α2 helices of *Vv*S.

5.3.4 Potential interaction sites within the STAS core

Sequence analysis of the STAS domains of *Vv*R and *Vv*S revealed an identity of around 20 %. Several conserved residues were observed, for instance in the loop regions between α1 and β3, β3 and α2 and in β4 (Figure 47 sequence, conserved amino acids are marked with a star below). The homology models of *Vv*S and *Vv*R exhibit the typical STAS domain α-helices and β-strands arrangement. *Vv*R has four β-strands (Figure 48A) but *Vv*S shows an additional small β-strand between α3 and α4 containing two hydrophobic residues (Leu and Val) (Figure 47C).

The phosphorylation sites of *Vv*R and *Vv*S are positioned at the core surface (Figure 47B) and are similarly accessible as phosphorylation sites of *Bs*RsbRA and *Bs*RsbS (Marles-Wright et al., 2008). The permanently phosphorylated Thr-171 in RsbRA is equivalent to the *Vv*R Thr-191 and both are located close to the linker helix (Figure 47). Thr-205 of *Bs*RsbR is at a more distant location when compared to the *Vv*R-Thr-232. The phosphorylation pattern of STAS domains upon stress is complex and object of intensive investigations. The double phosphorylation of Thr-171 and Thr-205 in *B. subtilis* occurs only upon strong stress and limits the σ^B activation to a tolerable level (Eymann et al., 2011). Mutation of the phosphorylated residue Thr-171 blocks the stress response of the stressosome (Kim et al., 2004 (b)) meaning that Thr-171 seems to be essential for stress signal transduction. Interestingly substitution of the *Bs*RsbS Ser-59 to alanine reduces but does not cancel the activation output suggesting that Ser-59 might be an evolutionary addition to increase the sensitivity of the stressosome by increasing the release of RsbT (Gaidenko and Price, 2014). Two pathways are proposed for signal transduction, one independent of Ser-59 causing a conformational shift to release RsbT and another depending on Ser-59 phosphorylation by unmasking the phosphorylation site or active stimulation of the kinase. The precise pathways of the different phosphorylation situations within the response procedure are still unknown and await further investigation.

Several amino acid residues, which are ideal located to play a role in the STAS domain interaction have been identified in the homology model and are displayed

in Figure 48. The interaction network of *Vv*R proteins within a homo-dimer is shown in Figure 48A.

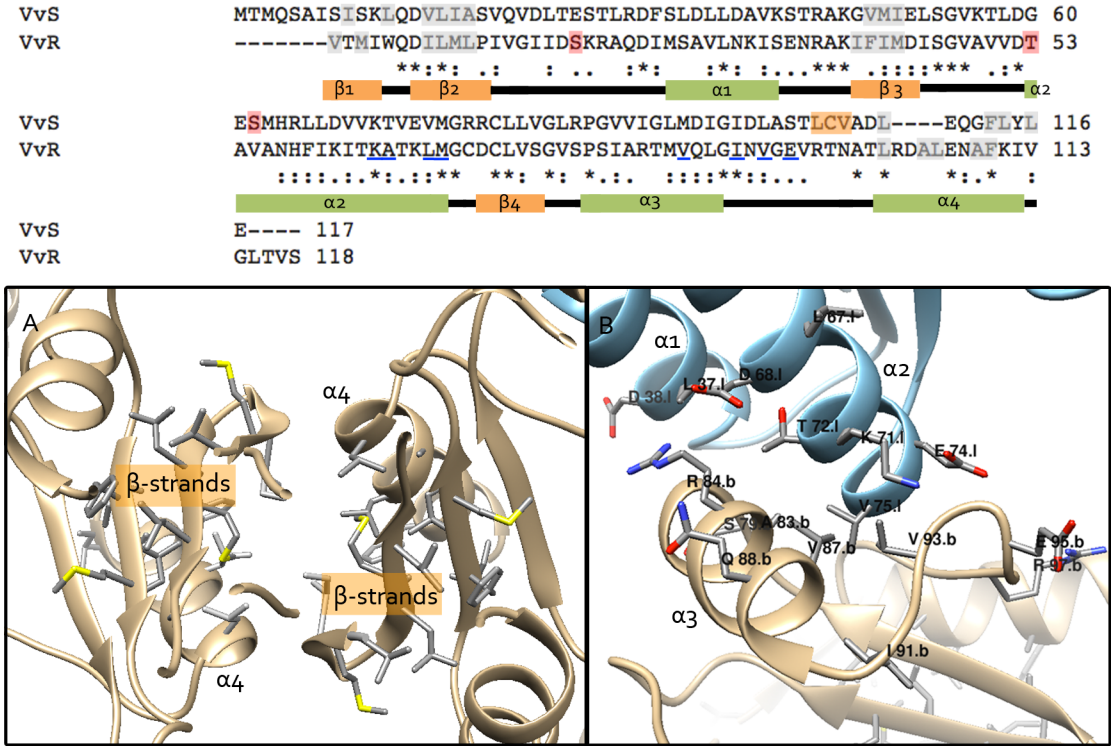

Figure 48 Sequence of the *Vv*R and *Vv*S STAS domains with secondary structure prediction and below amino acid residues of certain possible contact sites are displayed.

Top: Sequence alignment of *Vv*R and *Vv*S STAS domain. β-strands are shown in orange and the α-helices in green highlighted under the sequences. Note that the N-terminal sequence of *Vv*R (1-176) is excluded for the alignment of the STAS domains, therefore amino acid labels must be added to 176 in order to gain the original sequence numbering. **Gre**y marking: hydrophobic residues of the β-strands. **Red** marking: phosphorylation sites at position 62 the serine residue in *Vv*S and at position 191 the serine and 232 the threonine residue of *Vv*R. **Blue** underline: possible interaction partners of adjacent *Vv*R monomers. **A:** Hydrophobic dimer interface of *Vv*R monomers (brown), the contributing residues are displayed as sticks. For simplicity the residue labeling was omitted. **B:** Interaction site of adjacent *Vv*R (brown) and *Vv*S (blue) proteins and probable interacting residues. The label .l and .b after the residue specifier marks the displayed protein, *Vv*R or *Vv*S, in the entire model.

The homology model fitted to the 3D map shows the interface of the *Vv*R and *Vv*S dimer as a mainly hydrophobic β-strand assembly (β1-β3) (Figure 48 sequence, Figure 48A). A similar hydrophobic arrangement was found in the crystal structure of YtvA that crystallized as dimer with the STAS β-strands facing each other and the hydrophobic residues of the interface form intermolecular contact between the two monomers (Möglich and Moffat, 2007). The α4 helix protrudes into the inner sphere of the core contributing to the C-terminal region of the hydrophobic dimer interface (Figure 48A).

The monomers of each dimer (*Vv*R and *Vv*S) are rotated slightly in opposite directions about a virtual intermediate-point in the hydrophobic interface, such that the linker helices are tightly positioned and their C-terminal end is in contact with the α1 helix (Figure 47B).

Interactions between adjacent *Vv*R proteins and adjacent *Vv*R and *Vv*S proteins (for comparison Figure 27) take place at the ventral part of the helices α1 and α2 and the outer side of the α3 helix (Figure 48B) and the nature of the interaction possibilities differ depending on whether *Vv*R and *Vv*R are close to each other or whether *Vv*R is located next to a *Vv*S. The homology model suggests dominantly ionic interactions between *Vv*R and *Vv*S, e.g., positively (R84.b, K71.l) and negatively (D68.l, Q88.b) charged residues that could form salt bridges between *Vv*R and *Vv*S (Figure 48B). Additional hydrophobic residues such as *Vv*R-V87.b, -A83.b and *Vv*S-V75.l are recognizable. The loop between α3 and α4 can make contact to the α2 helix of *Vv*S (Figure 48B). Ionic interaction between *Vv*S and the *Vv*R could appear as well as some hydrophobic interactions between the beginning of the *Vv*R loop and α2 of *Vv*S.

For adjacent *Vv*R monomers of two different dimers the helical arrangement is as mentioned before, α1 and α2 of *Vv*R monomer 1 (*Vv*R1) are close to the α3 helix of the *Vv*R monomer two (*Vv*R2). Potential interaction residues between 2 adjacent *Vv*R proteins are underlined in blue in the sequence of Figure 48. Hydrophobic residues can be determined as well as positive and negative residues for possible ion binding. All these amino acid interactions could play a role in transmitting the conformational rearrangement of the core by an incoming trigger. Within a dimer

the hydrophobic interactions form an inner tight zone whereas the connections between adjacent proteins appear more loose for flexible rearrangement. The inner sphere of the core is bordered with hydrophobic residues.

5.3.5 Interplay of the stressosome proteins

Conformational changes in the STAS domains of *Vv*RS occur upon activation. Depending on the activation state of the individual V*v*R subunits they might take place at different times resulting in a number of sub-states thereby controlling the release of a specific amount of *Vv*T. Phosphorylation dependent affinity changes of RsbT to the anti-sigma factor RsbS might be an additional or even alternative mechanism of activation. RsbT has a much lower affinity to phosphorylated RsbS than to the dephosphorylated form. Such a mechanism was shown for *Mt*S-P and *Mt*T (Quin et al., 2012). It is not clear if the RsbS phosphorylation site is necessary for activation and release of RsbT due to the fact that mutation of Ser-59 did not lead to a complete elimination of the stress response (Gaidenko and Price 2014). It is more likely that depending on the stimulus, different activation pathways in the STAS domain core take place like an affinity switch of RsbT to RsbS or some fine-tuning phosphorylation processes that lead to the specific release of the kinase. The *B. subtilis* RsbT possesses an ATP lid that is directly positioned above the Ser-59 of *Bs*RsbS, but the phosphorylation sites of *Bs*RsbR seem to be not accessible for RsbT. This indicates that a movement must occur if phosphorylation of RsbR Thr-205 takes place by RsbT, supporting in turn the finding of core flexibility in this work.

Based on the work of Gaidenko et al. in 2012 we could assume that the outer side of the linker helix of RsbR is able to contact other proteins or ligands and hence, a possible interaction could take place with the sequestered RsbT. Further such contact could trigger the release of RsbT and Ser-59 of the STAS domain of RsbS would play no role in the activation process. The dynamics of stressosome components definitely plays a role in the activation process.

5.3.6 YtvA: a representative for flexibility in RsbR proteins

At last the interesting and detailed investigation about YtvA must be mentioned, although is lacks the phosphorylation sites and is the only known RsbR paralog containing a LOV domain. Several investigations of YtvA have been performed (Möglich and Moffat 2007; van der Steen et al., 2012, 2013; Jurk et al. 2010, 2011, 2013; Dorn et al., 2013) and based on these results we could determine many parallels between the stressosomes of *B. subtilis* and *V. vulnificus*.

Our homology model shows that the C-terminal parts of the *Vv*R linker helices protrude into the core. This observation is confirmed by the finding of Jurk et al. in 2011 that the Jα helices of YtvA are not accessible. YtvA is part of the *B. subtilis* stressosome assembly *in vivo* and consist of a LOV domain that is sensitive for blue light. Further investigations by solution NMR spectroscopy established mobility of the protein on several domains (Jurk et al., 2011). They demonstrated flexibility for the N- and C-terminal end of the protein, however, the LOV and STAS domains show different mobility levels. Whereas the LOV domain is supposed to be more rigid, the STAS domain is much more flexibile and performs a so-called "breathing event" for the C-terminal helix. The LOV domains exhibit flexibility only at the N-terminal end. For the linker helix (Jα) mobility was observed as well, especially a high flexibility of the C-terminal part but no structural rearrangement.

These findings of high flexibility agree very well with our results of a flexible stressosome and STAS domain core likewise. Equally the flexibility of the N-terminal domains of *Vv*R we found is existent in another *Vv*R homolog.

6. CONCLUSION AND PERSPECTIVES

This is the first experimental evidence that the proteins of the *Listeria* RST module assemble to a stressosome. Further interaction studies of the *Li*R, *Li*S and *Li*T proteins could be carried out to understand which conditions are necessary for interaction and activation of the *Listeria* stressosome. *In vivo* null mutations of the *Li*R paralogs would be important to determine the stimuli of stress conditions. Using a minimal stressosome (comprising one *Li*R paralog) under various stress stimuli could verify the conditions of the GSR induction. Here the implementation of GSR gene transcription could be determined by a σ^B dependent expression of a fusion protein, similarly performed and reported by Gaidenko et al. in 2012 or Martinez et al. in 2010, who conducted β-Galactosidase accumulation or activity tests to measure the stress response. This could be used to clarify whether only environmental stress stimulates the stressosome of *Listeria* or if in addition to this energy stress, e.g., starvation also activates the stressosome (as observed by Martinez et al. 2010).

For the *V. vulnificus* stressosome the trigger for activation is presumed to be oxygen. Structural investigations by single particle analysis were performed in this work to reveal the structure of the oxidized *Vv*RS complex. From our findings we conclude that the structure of stressosome seems to be conserved in Gram-positive and Gram-negative bacteria. During our study we could show the dynamics of the stressosome complex. The data revealed a higher flexibility for the N-terminal domains of *Vv*R than for the *Vv*RS STAS core. The flexibility for the STAS core could be demonstrated in different maps representing conformational intermediates during activation. A further comparison of structural dynamics of reduced and oxidized *Vv*RS stressosome and the entire *Vv*RST complex would shed light into the functional conformational changes during activation.

Studies of the native *Vv*RST stressosome with or without oxygen and substitutions on the co-factor binding N-terminal domain of *Vv*R could verify which residues of the heme pocket are important for oxygen binding. A crystal structure of the N-*Vv*R could expose the detailed structure of the activated and inactivated state and the

bound co-factor (similar to HemAT by Zhang and Philips in 2003 and YtvA by Möglich and Moffat, 2007).

LITERATURE

Akbar S., Gaidenko T. A., Kang C. M., O'Reilly M., Devine K. M., Price C. W. "New family of regulators in the environmental signaling pathway which activates the general stress transcription factor sigma(B) of *Bacillus subtilis*." Journal of Bacteriology 183(4) 1329-38, (2001).

Allegretti M., Mills D. J., McMullan G., Kühlbrandt W., Vonck J. "Atomic model of the F420-reducing [NiFe] hydrogenase by electron cryo-microscopy using a direct electron detector." *eLife* 3:e01963, (2014).

Amunts A., Brown A., Bai X.-C., Llacer J. L., Hussain T., Emsley P., Long F., Murshudov G., Scheres S. H. W., Ramakrishnan V. "Structure of the Yeast Mitochondrial Large Ribosomal Subunit." *Science* 343, 1485-1489, (2014).

Aravind L. & Koonin E. V. "The STAS domain - a link between anion transporters and antisigma-factor antagonists." Current Biology 10(2), R53-55, (2000).

Armache J.-P.,. Jarasch A., Anger A. M., Villa E., Becker T., Bhushan S., Jossinet F., Habeck M., Dindar G., Franckenberg S., Marquez V., Mielke T., Thomm M., Berninghausen O., Beatrix B, Söding J., Westhof E., Wilson D. N., Beckmanna R. "Localization of eukaryote-specific ribosomal proteins in a 5.5-Å cryo-EM map of the 80S eukaryotic ribosome." *Biochemistry*. doi: 10.1073/pnas.1010005107 PMCID: PMC2993421, (2010).

Avila-Pérez M., Hellingwerf K. J., Kort R. "Blue Light Activates the σ^B-Dependent Stress Response of *Bacillus subtilis* via YtvA." *Journal of Bacteriology* 188(17), 6411–6414, (2006).

Bai X.-C., Fernandez I. S., McMullan G., Scheres S. H. W. "Ribosome structures to near-atomic resolution from thirty thousand cryo-EM particles." *eLife* 2:00461, (2013).

Bai X.-C., McMullan G., Scheres S. H. W. "How cryo-EM is revolutionizing structural biology." *Trends in Biochemical Sciences* 40(1), 49-57, (2015).

Brilot A. F., Chen J.Z., Cheng A., Pan J., Harrison S. C., Potter C. S., Carragher B., Henderson R., Grigorieff N. "Beam-induced motion of vitrified specimen on holey carbon film." *Journal of Structural Biology* 177(3), 630–637, (2012).

Buttani V., Losi A., Polverini E., Gaertner W. "Blue news: NTP binding properties of the blue-light sensitive YtvA protein from Bacillus subtilis." *FEBS* 580(12), 3818–3822, (2006).

Campbell M. G., Cheng A., Brilot A. F., Moeller A., Lyumkis D., Veesler D., Pan J., Harrison S. C., Potter C. S., Carragher B., Grigorieff N. "Movies of ice-embedded particles enhance resolution in electron cryo-microscopy." *Structure* 20(11), 1823–1828, (2012).

Campbell M. G., Underbakke E. S., Potter C. S., Carragher B., Marletta M. A. "Single-particle EM reveals the higher-order domain architecture of soluble guanylate cyclase." *PNAS* 111(8), 2960–2965, (2014).

Chen C-C., Lewis R. J., Harris R., Yudkin M. D., Delumeau O. "A supramolecular complex in the environmental stress signalling pathway of *Bacillus subtilis.*" *Molecular Microbiology* 49(6), 1657–1669, (2003).

Chen C-C. Yudkin M. D., Delumeau O. "Phosphorylation and RsbX-Dependent Dephosphorylation of RsbR in the RsbR-RsbS Complex of *Bacillus subtilis.*" *Journal of Bacteriology* 186(20), 6830–6836, (2004).

Cheng Y., "Single-Particle Cryo-EM at Crystallographic Resolution." *Cell* 161(3), 450-457, (2015).

Ciccarelli L., Connell S. R., Enderle M., Mills D. J., Vonck J., Grininger M. "Structure and Conformational Variability of the *Mycobacterium tuberculosis* Fatty Acid Synthase Multienzyme Complex." *Structure* 21(7), 1251-1257, (2013).

Cossio P. & Hummer G. "Bayesian analysis of individual electron microscopy images: Towards structures of dynamic and heterogeneous biomolecular assemblies." *Journal of Structural Biology* 184(3), 427-437, (2013).

de Been M., Francke C., Siezen R. J., Abee T. "Novel σB regulation modules of Gram-positive bacteria involve the use of complex hybrid histidine kinases.", *Microbiology* 157, 3–12, (2011).

Delumeau O., Lewis R. J, Yudkin M. D. "Protein-protein interactions that regulate the energy stress activation of sigma(B) in *Bacillus subtilis*." *Journal of Bacteriology* 184(20), 5583-9, (2002).

Delumeau O., Dutta S., Brigulla M., Kuhnke G., Hardwick S. W., Völker U., Yudkin M. D. and Lewis R. J. "Functional and Structural Characterization of RsbU, a Stress Signaling Protein Phosphatase 2C." *Journal of Biological Chemistry* 279, 40927-40937, (2004).

Delumeau O., Chen C.-C., Murray J. M., Yudkin M. D, Lewis R. J. "High-molecular-weight complexes of RsbR and paralogues in the environmental signaling pathway of Bacillus subtilis." *Journal of Bacteriology* 188(22), 7885-7892, (2006).

Disson O. & Lecuit M. "Targeting of the central nervous system by *Listeria monocytogenes*." *Virulence* 3(2), 213–221, (2012).

Dorn M., Jurk M., Wartenberg A., Hahn A., Schmieder P. "LOV takes a pick: thermodynamic and structural aspects of the flavin-LOV-interaction of the blue-light sensitive photoreceptor YtvA from *Bacillus subtilis*." *PLoS ONE* 8(11), e81268, (2013).

Dubochet J., Lepault J., Freeman R., Berriman J. A., Homo J.-C. "Electron microscopy of frozen water and aqueous solutions." *Journal of Microscopy* 128(3), 219–237, (1982).

Dufour A., Voelker U., Voelker A., Haldenwang W. G. "Relative Levels and Fractionation Properties of *Bacillus subtilis* σ^B and Its Regulators during Balanced Growth and Stress." *Journal of Bacteriology* 178(13), 3701–3709, (1996).

Eymann C., Schulz S., Gronau K., Becher D., Hecker M., Price C. W. "In vivo phosphorylation patterns of key stressosome proteins define a second feedback loop that limits activation of *Bacillus subtilis* sigma-B." *Molecular Microbiology* 80, 798-810, (2011).

FAO/WHO, "Risk assessment of *Vibrio vulnificus* in raw oysters: Interpretative summary and technical report." *Microbiological Risk Assessment*, 8. Rome, Italy: FAO. (2005).

Frank J., Penczek P., Grassucci R., Srivastava S. "Three-Dimensional Reconstruction of the 70S Escherichia coli RibosomeinIce: The Distribution of Ribosomal RNA." *The Journal of Cell Biology* 115, 597-605, (1991).

Freitas T. A. K, Hou S., Alam M. "The diversity of globin-coupled sensors." *FEBS Letters* 552(2-3), 99-104, (2003).

Gabashvili I. S., Agrawal R. K., Spahn C. M. T., Grassucci R. A., Svergun D.I., Frank J., Penczek P. "Solution Structure of the E. coli 70S Ribosome at 11.5 Å Resolution." *Cell* 100, 537–549, (2000).

Gaidenko T. A., Yang X., Lee Y. M., Price C. W. "Threonine phosphorylation of modulator protein RsbR governs its ability to regulate a serine kinase in the environmental stress signaling pathway of *Bacillus subtilis.*" *Journal of Molecular Biology* 288, 29-39, (1999).

Gaidenko T. A., Kim T.-J., Weigel A. L., Brody M. S., Price C. W. "The blue-light receptor YtvA acts in the environmental stress signaling pathway of *Bacillus subtilis*." *Journal of Bacteriology* 188(17), 6387–6395, (2006).

Gaidenko T. A., Bie X., Baldwin E. P., Price C. W. "Substitutions in the presumed sensing domain of the *Bacillus subtilis* stressosome affect its basal output but not response to environmental signals." *Journal of Bacteriology* 193(14), 3588-3597, (2011).

Gaidenko T. A., Bie X., Baldwin E. P., Price C. W. "Two surfaces of a conserved interdomain linker differentially affect output from the RST sensing module of the *Bacillus subtilis* stressosome." *Journal of Bacteriology* 194(15), 3913-3921, (2012).

Gaidenko, T. A., Price C. W. "Genetic evidence for a phosphorylation-independent signal transduction mechanism within the *Bacillus subtilis* stressosome." *PLoS One.* 9:e90741, (2014).

Glaser P., Frangeul L., Buchrieser C., Rusniok C., Amend A., Baquero F., Berche P., Bloecker H., Brandt P., Chakraborty T., Charbit A., Chetouani F., Couvé E., de Daruvar A., Dehoux P., Domann E., Domínguez-Bernal G., Duchaud E., Durant L., Dussurget O., Entian K. D., Fsihi H., García-del Portillo F., Garrido P., Gautier L., Goebel W., Gómez-López N., Hain T., Hauf J., Jackson D., Jones L. M., Kaerst U., Kreft J., Kuhn M., Kunst F., Kurapkat G., Madueno E., Maitournam A., Vicente J. M., Ng E., Nedjari H., Nordsiek G., Novella S., de Pablos B., Pérez-Diaz J. C., Purcell R., Remmel B., Rose M., Schlueter T., Simoes N., Tierrez A., Vázquez-Boland J. A., Voss H., Wehland J., Cossart P. "Comparative Genomics of *Listeria* Species." *Science* 294, 849-852, (2001).

Grigorieff N., Harrison S. C. "Near-atomic resolution reconstructions of icosahedral viruses from electron cryo-microscopy." *Current Opinion in Structural Biology* 21, 265–273, (2011).

Guex N. & Peitsch M. C. "SWISS-MODEL and the Swiss-PdbViewer: An environment for comparative protein modeling." *Electrophoresis* 18, 2714-2723, (1997).

Hecker M., Pané-Farré J., Voelker U. "SigB-Dependent General Stress Response in *Bacillus subtilis* and Related Gram-Positive Bacteria." *Annual Review of Microbiology* 61, 215–36, (2007).

Hecker M. & Völker U. "Non-specific, general and multiple stress resistance of growth-restricted Bacillus subtilis cells by the expression of the sigmaB regulon." *Molecular Microbiology* 29(5), 1129-36, (1998).

Henderson R. "Overview and future of single particle electron cryomicroscopy." *Archives of Biochemistry and Biophysics* 581(C), 19-24 , (2015).

Herrou J. & Crosson S. "Function, structure and mechanism of bacterial photosensory LOV proteins." *Nature Reviews Microbiology* 9(10), 713-23, (2011).

Hou S., Larsen R. W., Boudko D., Riley C. W., Karatan E., Zimmer M., Ordal G. W., Alam M. "Myoglobin-like aerotaxis transducers in Archaea and Bacteria." *Nature* 403(6769), 540-544, (2000).

Jin Q., Sorzano C. O. S., Rosa-Trevín J. M. de la, Bilbao-Castro J. R., Núñez-Ramírez R., Llorca O., Tama F., Jonić S. "Iterative Elastic 3D-to-2D Alignment Method Using Normal Modes for Studying Structural Dynamics of Large Macromolecular Complexes." *Structure* 22 (3), 496-506, (2014).

Jurk M., Dorn M., Kikhney A., Svergun D., Gärtner W., Schmieder P. "The Switch that Does Not Flip: The Blue-Light Receptor YtvA from *Bacillus subtilis* Adopts an Elongated Dimer Conformation Independent of the Activation State as Revealed by a Combined AUC and SAXS Study." *Journal of Molecular Biology* 403(1), 78-87, (2010).

Jurk M., Dorn M., Schmieder P. "Blue Flickers of Hope: Secondary Structure, Dynamics, and Putative Dimerization Interface of the Blue-Light Receptor YtvA from *Bacillus subtilis.*" *Biochemistry* 50(38), 8163-8171, (2011).

Killmann H., Benz R., Braun V. "Properties of the FhuA channel in the *Escherichia coli* outer membrane after deletion of FhuA portions within and outside the predicted gating loop" *Journal of Bacteriology* 178, 6913–6920, (1996).

(a) Kim T.-J., Gaidenko T. A., Price C. W. "A Multicomponent Protein Complex Mediates Environmental Stress Signaling in *Bacillus subtilis*." *Journal of Molecular Biology* 341, 135–150, (2004).

(b) Kim T.-J., Gaidenko T. A., Price C. W. "In Vivo Phosphorylation of Partner Switching Regulators Correlates with Stress Transmission in the Environmental Signaling Pathway of *Bacillus subtilis*" *Journal of Bacteriology* 186(18), 6124–6132, (2004).

Kovacs H., Comfort D., Lord M., Campbell I. D., Yudkin M. D. "Solution structure of SpoIIAA, a phosphorylatable component of the system that regulates transcription factor σ^F of *Bacillus subtilis*." *PNAS* 95, 5067–5071, (1998).

Lau W. C. & Rubinstein J. L. "Single particle electron microscopy." *Methods in Molecular Biology* 955, 401-426, (2013).

Li X., Mooney P., Zheng S., Booth C. R., Braunfeld M. B., Gubbens S., Agard D. A., Cheng Y. "Electron counting and beam-induced motion correction enable near-atomic-resolution single-particle cryo-EM." *Nature Methods* 10(6), 584-590, (2013).

Liao M., Cao E., Julius D., Cheng Y. "Structure of the TRPV1 ion channel determined by electron cryo-microscopy." *Nature* 504, 107-112, (2013).

Losi A. "Flavin-based Blue-light Photosensors: A Photobiophysics Update." *Photochemistry and Photobiology* 83, 1283-1300, (2007).

Ludtke S. J., Baldwin P. R., Chiu W. "EMAN: Semiautomated Software for High-Resolution Single-Particle Reconstructions." *Journal of Structural Biology* 128 , 82–97, (1999).

Ludtke S. J., Joanita Jakana J., Song J.-L.,. Chuang D. T., Chiu W. "A 11.5 AÊ Single Particle Reconstruction of GroEL Using EMAN." *Journal of Molecular Biology* 314, 253-262, (2001).

Ludtke S. J., Baker M. L., Chen D.-H., Song J.-L., Chuang D. T., Chiu W. "De Novo Backbone Trace of GroEL from Single Particle Electron Cryomicroscopy." *Structure* 16, 441–448, (2008).

Ludtke S. J., Tran T. P, Ngo Q. T., Moiseenkova-Bell, V. Y., Chiu W., Serysheva I. I. "Flexible Architecture of IP3R1 by Cryo-EM." *Structure* 19(8), 1192-1199, (2011).

Ludtke S. J., Serysheva I. I. "Single-particle Cryo-EM of calcium release channels: structural validation." *Current Opinion in Structural Biology* 23, 755–762, (2013).

Marles-Wright J., Grant T., Delumeau O., van Duinen G., Firbank S. J., Lewis P. J., Murray J. W., Newman J. A., Quin M. B., Race P. R., Rohou A., Tichelaar W., van Heel M., Lewis R. J. "Molecular Architecture of the "Stressosome," a Signal Integration and Transduction Hub." *Science* 322, 92-96, (2008).

Marles-Wright J. & Lewis R. J. "The stressosome: molecular architecture of a signalling hub." *Biochemical Society Transactions* 38(4), 928-933, (2010).

Martinez L., Reeves A., Haldenwang W. "Stressosomes Formed in *Bacillus subtilis* from the RsbR Protein of *Listeria monocytogenes* Allow σ^B Activation following

Exposure to either Physical or Nutritional Stress." *Journal of Bacteriology* 192(23), 6279–6286, (2010).

McMullan G., Chen S., Henderson R., Faruqi A.R. "Detective quantum efficiency of electron area detectors in electron microscopy." *Ultramicroscopy* 109, 1126–1143, (2009).

Mills D. J., Vitt S., Strauss M., Shima S., Vonck J. "De novo modeling of the F420-reducing [NiFe]-hydrogenase from a methanogenic archaeon by cryo-electron microscopy." *eLife* 2:e00218, (2013).

Mindell J. A. & Grigorieff N. "Accurate determination of local defocus and specimen tilt in electron microscopy." *Journal of Structural Biology* 142, 334–347, (2003).

Murray J. W., Delumeau O., Lewis R. J. "Structure of a nonheme globin in environmental stress signaling." *PNAS* 102(48), 17320–17325, (2005).

Möglich A. & Moffat K. "Structural Basis for Light-dependent Signaling in the Dimeric LOV Domain of the Photosensor YtvA." *Journal of Molecular Biology* 373(23), 112–126, (2007).

Möglich A., Yang X., Ayers R. A., Moffat K. "Structure and function of plant photoreceptors." *Annual Review of Plant Biology* 61, 21-47, (2010).

Nagayama K. "Biological applications of phase-contrast electron microscopy.", In: Kuo J. "Electron Microscopy, Methods and Protocols", 3th edition, *Methods in Molecular Biology* 1117, 385-399, (2014).

Orlova E. V. & Saibil H. R. "Structural Analysis of Macromolecular Assemblies by Electron Microscopy." *Chemical Reviews* 111, 7710–7748, (2011).

Pané-Farré J., Lewis R. J., Stülke J. "The RsbRST stress module in bacteria: A signalling system that may interact with different output modules." *Journal of Molecular Microbiology and Biotechnology* 9, 65–76, (2005).

Pasqualetto E., Aiello R., Gesiot L., Bonetto G., Bellanda M., Battistutta R. "Structure of the Cytosolic Portion of the Motor Protein Prestin and Functional Role of the STAS Domain in SLC26/SulP Anion Transporters." *Journal* of *Molecular Biology* 400, 448–462, (2010).

Pettersson B. M. F., Nitharwal R. G, Das S., Behra K. P. R., Benedik E., Arasu U. T., Islam N. M., Dasgupta S., Bhattacharya A., Kirsebom L. A. "Identification and expression of stressosomal proteins in *Mycobacterium marinum* under various growth and stress conditions." *FEMS Microbiology Letters* 342(2), 98-105, (2013).

Pettersen E. F., Goddard T.D., Huang C.C., Couch G.S., Greenblatt D.M., Meng E.C., Ferrin T.E. "UCSF Chimera--a visualization system for exploratory research and analysis." *Journal of Computational Chemistry* 13, 1605-1612, 2004.

Phippen B. L. & Oliver J. D. "Role of Anaerobiosis in Capsule Production and Biofilm Formation in *Vibrio vulnificus*." *Infection and Immunity*, 83(2), 551-559, (2015).

Price C. W. "General stress response in *Bacillus subtilis* and related Gram positive bacteria.", 301-318 in: Storz G. & Hengge R. (ed.), Bacterial Stress Responses, 2nd edn. *American Society for Microbiology*, Washington D.C., (2010).

Quin M. B., Berrisford J. M., Newman J. A., Baslé A., Lewis R. J., Marles-Wright J. "The Bacterial Stressosome: A Modular System that Has Been Adapted to Control Secondary Messenger Signaling" *Structure* 20, 350–363, (2012).

Rademacher M., Wagenknecht T., Verschoor A., Frank, J. "Three-dimensional structure of the large ribosomal subunit from Escherichia coli." *EMBO Journal* 6, 1107-1114, (1987).

Raengpradub S., Wiedmann M., Boor K. J. "Comparative Analysis of the σ^B-Dependent Stress Responses in *Listeria monocytogenes* and *Listeria innocua* Strains Exposed to Selected Stress Conditions." *Applied and Environmental Microbiology* 74(1), 158–171, (2008).

Reeves A. & Haldenwang, W. G. "Isolation and characterization of dominant mutations in the Bacillus subtilis stressosome components RsbR and RsbS." *Journal of Bacteriology* 189 (5), 1531-41, (2007).

Sambrook J., Fritsch E.F., Maniatis T. "Molecular Cloning: A Laboratory Manual." *Cold Spring Harbor Laboratory Press*, Cold Spring Harbor, New York, (1989).

Scheres S. H. W. "RELION: Implementation of a Bayesian approach to cryo-EM structure determination." *Journal of Structural Biology* 180(3), 519-530, (2012).

Scheres S. H. W. & Chen S. "Prevention of overfitting in cryo-EM structure determination." *Nature Methods* 9(9), 853-854, (2012).

(a) Sharma A. K., Rigby A. C. Alper S. L. "STAS Domain Structure and Function." *Cellular Physiology and Biochemistry* 28, 407-422, (2011).

(b) Sharma A. K., Ye L., Baer C. E., Shanmugasundaram K., Alber T., Alper S. L., Rigby A. C. "Solution Structure of the Guanine Nucleotide-binding STAS Domain of SLC26-related SulP Protein Rv1739c from *Mycobacterium tuberculosis.*" *Journal of Biological Chemistry* 286(10), 8534–8544, (2011).

Sharma A. K., Zelikovic I., Alper S. L. "Molecular Dynamics Simulations of the STAS Domains of Rat Prestin and Human Pendrin Reveal Conformational Motions in Conserved Flexible Regions." *Cellular Physiology and Biochemistry* 33(3), 605-620, (2014).

Shin J.-H., Brody M. S., Price C. W. "Physical and antibiotic stresses require activation of the RsbU phosphatase to induce the general stress response in *Listeria monocytogenes.*" *Microbiology* 156, 2660-2669, (2010).

Stranzl G. R., Santelli E., Bankston L. A., Clair C. L., Bobkov A., Schwarzenbacher R., Godzik A., Perego M., Grynberg M., Liddington R. C. "Structural insights into inhibition of *Bacillus anthracis* sporulation by a novel class of non-heme globin sensor domains." *Journal of Biological Chemistry* 286(10), 8448-8458, (2011).

Tama F., Miyashita O., Brooks C.L. "Normal mode based flexible fitting of high-resolution structure into low-resolution experimental data from cryo-EM." *Journal of Structural Biology* 147(3), 315–326, (2004).

Tang G., Peng L., Baldwin P. R., Mann D. S., Jiang W., Rees I., Ludtke S. J. "EMAN2: An extensible image processing suite for electron microscopy." *Journal of Structural Biology* 157(1), 38–46, (2007).

Tischler A. D. & Camilli A. "Cyclic diguanylate (c-di-GMP) regulates *Vibrio cholerae* biofilm formation." *Molecular Microbiology* 53(3), 857–869, (2004).

van der Steen J. B., Ávila-Pérez M., Knippert D., Vreugdenhil A., Alphen P. van, Hellingwerf K. J. "Differentiation of Function among the RsbR Paralogs in the General Stress Response of *Bacillus subtilis* with Regard to Light Perception." *Journal of Bacteriology* 194(7), 1708–1716, (2012).

van der Steen J. B., Nakasone Y., Hendriksy J., Hellingwerf K. J. "Modeling the functioning of YtvA in the general stress response in *Bacillus subtilis*." *Molecular BioSystems* 9(9), 2331-2343, (2013).

van Heel M. & Keegstra W. "IMAGIC: A fast, flexible and friendly image analysis software system." *Ultramicroscopy* 7, 113-130, (1981).

van Heel, M. "Classification of very large electron microscopical image data sets." *Optik* 82, 114–126, (1989).

Voelker U., Voelker A., Haldenwang W. G. "Reactivation of the *Bacillus subtilis* anti-sigma B antagonist, RsbV, by stress- or starvation-induced phosphatase activities." *Journal of Bacteriology* 178(18), 5456-5463, (1996).

Walter A., Steltenkamp S., Schmitz S., Holik P., Pakanavicius E., Sachser R., Huth M., Rhinow D., Kühlbrandt W. "Towards an optimum design for electrostatic phase plates." *Ultramicroscopy*, 116 62–72, (2012)

Wagenknecht T., Carazo J. M., Radermacher M., Frank J. "Three-dimensional reconstruction of the ribosome from Escherichia coli." *Biophysical Journal* 55, 455-464, (1989).

Wise A. A. & Price C. W. "Four Additional Genes in the *sigB* Operon of *Bacillus subtilis* That Control Activity of the General Stress Factor σ^B in Response to Environmental Signals." *Journal of Bacteriology* 177(1), 123–133, (1995).

Wolf M., Garcea R. L., Grigorieff N., Harrison S. C. "Subunit interactions in bovine papillomavirus." PNAS 107, 6298–6303, (2010).

Yang X., Kang C. M., Brody M. S., Price C. W. "Opposing pairs of serine protein kinases and phosphatases transmit signals of environmental stress to activate a bacterial transcription factor." *Genes and Development* 10, 2265-2275, (1996).

Yoshida Y., Ishikawa H., Aono S., Mizutani Y. "Structural dynamics of proximal heme pocket in HemAT-Bs associated with oxygen dissociation." *Biochimica et Biophysica Acta* 1824(7), 866–872, (2012).

Zhang W. & Phillips G. N. Jr. "Structure of the Oxygen Sensor in *Bacillus subtilis*: Signal Transduction of Chemotaxis by Control of Symmetry." *Structure* 11(9), 1097–1110, (2003).

Zhang X., Jin L., Fang Q., Hui W. H., Zhou Z. H. "3.3 A cryo-EM structure of a nonenveloped virus reveals a priming mechanism for cell entry." *Cell* 141, 472–482, (2010).